

A comparison of dynamic and kinematic observers

regarding roll and pitch of
a vehicle

A.J.F.D. Fritz

Master of Science Thesis



A comparison of dynamic and kinematic observers regarding roll and pitch of a vehicle

by

A.J.F.D. Fritz

to obtain the degree of Master of Science
at the Delft University of Technology,
to be defended publicly on Monday December 10, 2018 at 9:30 AM.

Student number: 4281616
Thesis committee: Dr. ir. R. Happee, TU Delft, chair
Dr. B. Shyrokau, TU Delft, supervisor
Dr ir. A.L. Schwab, TU Delft

An electronic version of this thesis is available at <http://repository.tudelft.nl/>.

Abstract

The automotive industry is continuously improving the safety and comfort of the vehicles. To improve the safety and comfort of the vehicle more focus is put on improving driver assistance systems and also on making the vehicles more autonomous. In order for the safety systems to work properly and also to drive autonomously, it becomes essential that the vehicle has accurate knowledge of all the states of the vehicle. Two of such states are the roll and pitch angle. They are used to correct the images of a stereo camera, in roll control systems and for comfort assessment in autonomous vehicles.

Measuring the roll and pitch angle is in practice problematic. Gyroscopes are mostly used to calculate the roll and pitch angle by integrating the angular rates with respect to time. If low quality gyroscopes are used, this leads to inaccurate calculation of the roll and pitch angle, because the measurements contain noise or bias accumulated during the integration process. To use these low quality gyroscopes, they need to be incorporated in a robust algorithm together with other sensors. Only then the roll and pitch angle can be estimated accurately.

In this thesis a dynamic observer is developed, which has an internal vehicle dynamic model that calculates the tyre forces using an exponential tyre model. The performance of the observer is not only assessed using the true roll and pitch angle, but also compared against the performance of a kinematic observer.

To test the performance of both observers various test manoeuvres were executed in IPG CarMaker, which is a highly advanced vehicle simulation environment. The manoeuvres consisted of rapid steering inputs and hard braking to execute large roll and pitch angles. Sensor noise was added to the inputs of the observers to simulate low quality sensors. In this thesis it has been shown that incorporating dynamics into an observer significantly increases its estimation performance and outperforms the kinematic observer during all manoeuvres when sensor noise was added to the inputs of the observers.

The contribution of this thesis to the scientific field is that an exponential tyre model is used for the calculation of the roll and pitch angle in the internal vehicle dynamic model of the dynamic observer. Another contribution is that this thesis not only compares the performance of the dynamic observer against the real roll and pitch angles, but also against a kinematic observer, to see what the estimation improvement is when including dynamic relations.

Contents

Abstract	iii
List of Figures	vii
List of Tables	ix
List of Abbreviations	xi
List of Symbols	xiii
Acknowledgements	xvii
1 Introduction	1
1.1 Background	1
1.2 Problem	2
1.3 Thesis	4
1.4 Outline	4
2 Estimation Principles	5
2.1 Definition of Roll, Pitch and Yaw Angle	5
2.2 Sensors	5
2.2.1 Gyroscope	6
2.2.2 Global Positioning System	6
2.2.3 Inertial Measurement Unit	7
2.3 State Estimation	7
2.3.1 Linear Kalman Filter	7
2.3.2 Extended Kalman Filter	8
3 Dynamic Observer	11
3.1 Vehicle Modelling	11
3.1.1 State Variables	11
3.1.2 Tyre Modelling	12
3.1.3 State Equations	17
3.2 Estimator	18
3.2.1 Extended Kalman Filter Structure	18
3.2.2 Calculation Jacobian Elements	19
3.2.3 Initialisation and Tuning	20
4 Kinematic Observer	23
4.1 Methodology	23
4.2 Sensor Model	23
4.3 State Vector	24
4.4 Process Model	24
4.5 Measurement Model	25
4.5.1 Measurement Update 1	26
4.5.2 Measurement Update 2	27
4.6 Filter Procedure	28
5 Simulation Setup	29
5.1 Simulation Environments	29
5.1.1 Nonlinear Vehicle Model	29
5.1.2 IPG CarMaker	30

5.2	Test Manoeuvres	31
5.2.1	Sine Sweep	31
5.2.2	Step Response	31
5.2.3	Double Lane Change.	32
5.2.4	Skidpad	32
5.2.5	Fishhook.	32
5.2.6	Braking Straight Line.	32
5.2.7	Hockenheim Racetrack	33
5.3	Variances and Noise Generation	33
5.4	Initialisation of the Observers.	33
5.4.1	Kinematic Observer	33
5.4.2	Dynamic Observer	34
5.5	Passing Criteria	35
5.5.1	Mean Error.	35
5.5.2	Maximum error	35
6	Simulation Results	37
6.1	Roll & Pitch Angle	37
6.1.1	No Noise Added	37
6.1.2	Noise Added	40
6.1.3	Sensor Quality Dependence	43
6.2	Lateral Velocity Dynamic Observer	45
7	Conclusion and Recommendations	49
7.1	Conclusion	49
7.1.1	Roll and Pitch Angle Estimation	49
7.1.2	Lateral Velocity Estimation.	50
7.2	Recommendations	50
	Bibliography	51
A	Derivations	55
A.1	Derivatives Tyre Forces	55
A.2	Derivatives of Jacobian Elements	56
B	Figures Roll and Pitch Angle	61
B.1	No noise Added	61
B.2	Noise Added	64
C	Figures Lateral velocity estimation	69

List of Figures

1.1	Visualisation of a stereo camera, taken from [3]	2
1.2	Estimation performance kinematic observer normal drive WEpod	3
1.3	Estimation performance kinematic observer during emergency braking and hard cornering of the WEpod	3
2.1	Coordinate systems of the vehicle	5
3.1	Effect of tyre saturation	12
3.2	Effect of varying normal loads	12
3.3	Effect of combined slip	13
3.4	Tyre models comparison	13
3.5	Effect of combined slip	14
3.6	Transformation of velocities	14
3.7	Degrees of freedom in-plane	16
3.8	Roll degree of freedom, when looking at the vehicle from the front	17
4.1	Direction of linear and angular velocities as used in [7], taken from [7]	25
4.2	Kalman filter structure	28
5.1	Comparison of the roll and pitch angle	29
5.2	Comparison of the lateral velocity	30
5.3	Steering angle profile of the sine sweep manoeuvre	31
5.4	Steering angle profile of the step response manoeuvre. Steering angle is slowly increased till the lateral acceleration reaches 4 ms^{-2} , then two step steering inputs are applied	31
5.5	Trajectory of a double lane change, where B is the the car width, taken from [46]	32
5.6	Steering input of the fishhook manoeuvre	32
5.7	Layout of Hockenheim racetrack	33
6.1	Calculated roll and pitch angle in the internal vehicle model during the step response manoeuvre	37
6.2	Root Mean Square (RMS) error of each manoeuvre normalised to the best performing observer. Roll angle (a) and pitch angle (b)	38
6.3	Estimation performance during the fishhook manoeuvre	39
6.4	Estimation performance of driving on the Hockenheim racetrack	40
6.5	RMS error of the observers at each manoeuvre normalised to the best performing observer. Roll angle (a) and pitch angle (b)	41
6.6	Estimation performance during the skidpad manoeuvre with noise added	42
6.7	Estimation performance during the emergency braking manoeuvre with noise added	43
6.8	RMS errors of the observers as a function of gyroscope sensor quality of the double lane change manoeuvre	44
6.9	RMS errors of the observers as a function of gyroscope sensor quality of the fishhook manoeuvre	44
6.10	Estimation performance lateral velocity during the double lane manoeuvre	45
6.11	Estimation performance lateral velocity during the step response manoeuvre	46
6.12	Close up lateral velocity estimate of the step response manoeuvre	46
B.1	Estimation performance during the sine sweep manoeuvre	61
B.2	Estimation performance during the step response manoeuvre	62
B.3	Estimation performance during the double lane change manoeuvre	62
B.4	Estimation performance during the skidpad manoeuvre	63
B.5	Estimation performance during normal straight line braking	63
B.6	Estimation performance during emergency straight line braking	64

B.7	Estimation performance during the sine sweep manoeuvre with noise added	64
B.8	Estimation performance during the step response manoeuvre with noise added	65
B.9	Estimation performance during the double lane change manoeuvre with noise added	65
B.10	Estimation performance during the fishhook manoeuvre with noise added	66
B.11	Estimation performance during normal braking with noise added	66
B.12	Estimation performance of driving on the Hockenheim racetrack with noise added	67
C.1	Estimation performance of the lateral velocity during sine sweep manoeuvre	69
C.2	Estimation performance of the lateral velocity during the skidpad manoeuvre	70
C.3	Estimation performance of the lateral velocity during the fishhook manoeuvre	70
C.4	Estimation performance of the lateral velocity during driving on Hockenheim racetrack	70

List of Tables

2.1	Specifications and prices (Jan 2016) of different gyroscopes, taken from [7]	6
5.1	Variances and noise powers used in the simulation	33
5.2	Vehicle parameters of a compact hatchback	34
6.1	RMS errors of the observers for different manoeuvres, when no sensor noise is present	38
6.2	Maximum deviation of the observers for different manoeuvres, when no sensor noise is present	39
6.3	RMS errors of the observers for different manoeuvres, when sensor noise is present	41
6.4	Maximum deviation of the observers for different manoeuvres, when sensor noise is present	42
6.5	RMS error of lateral velocity estimate, when there is no noise and noise is present	45
6.6	Maximum deviation of lateral velocity estimates with respect to true value for the different manoeuvres with no noise and noise present	47

List of Abbreviations

- ABS** Anti-Lock Braking System. 38
- CAN** Controller Area Network. 26
- COG** centre of gravity. 4, 5, 15, 17, 18, 20
- DOF** degree of freedom. 11
- EKF** Extended Kalman Filter. 4, 8, 9, 11–13, 18, 20, 21, 34, 35
- ESC** Electronic Stability Control. 4, 11
- GPS** global positioning system. 1, 6
- IMU** inertial measurement unit. 6, 7, 11, 20, 23, 33
- MEMS** Micro-Electro-Mechanical Systems. 6, 7
- RMS** Root Mean Square. vii, ix, 35, 37–45, 47

List of Symbols

\mathbf{a}	External acceleration vector
\mathbf{A}_k	Linearized state matrix
a_x	Longitudinal acceleration
a_{x_k}	External acceleration x-axis
A_{x_k}	Actual accelerometer measurement x-axis
a_y	Lateral acceleration
a_{y_k}	External acceleration y-axis
A_{y_k}	Actual accelerometer measurement y-axis
a_z	Vertical acceleration
a_{z_k}	External acceleration z-axis
A_{z_k}	Actual accelerometer measurement z-axis
B_f	Front track width
\mathbf{B}_k	Discrete Input matrix
B_r	Rear track width
\mathbf{C}_k	Discrete Output matrix
c_α	Dimensionless constant
\mathbf{C}_θ	Pitch damping coefficient
$C_{\phi,f}$	Roll damping coefficient front
$C_{\phi,r}$	Roll damping coefficient rear
\mathbf{D}_k	Discrete Feed through matrix
$D_{z,f}$	Front vertical suspension damping
$D_{z,r}$	Rear vertical suspension damping
$F_{x,ij}$	Longitudinal tyre force
$F_{y,ij}$	Lateral tyre force
F_z^{long}	Longitudinal component of vertical tyre force
$F_{z,front}^{lat}$	Front lateral component of vertical tyre force
$F_{z,rear}^{lat}$	Rear lateral component of vertical tyre force
$F_{z,ij}$	Vertical tyre force
g	Gravitational constant
\mathbf{g}_k	Gravitational acceleration vector
g_{x_k}	Gravitational acceleration component on x-axis
G_{x_k}	Actual gyroscope measurement about x-axis
g_{y_k}	Gravitational acceleration component on y-axis
G_{y_k}	Actual gyroscope measurement about y-axis
g_{z_k}	Gravitational acceleration component on z-axis
G_{z_k}	Actual gyroscope measurement about z-axis
h_{cg}	Height centre of gravity
\mathbf{H}_k	Linearized feed through matrix
h_r	Distance from centre of gravity to roll axis
h_{roll}	Roll height
h_p	Distance from centre of gravity to pitch axis
h_{pitch}	Pitch height
\mathbf{H}_1	Observation matrix 1
\mathbf{H}_2	Observation matrix 2
\mathbf{I}	Identity matrix
I_{xx}	Body inertia around x-axis
I_{yy}	Body inertia around y-axis
I_{zz}	Body inertia around z-axis

\mathbf{K}_k	Kalman gain matrix
K_y	Linear tyre slip stiffness
$K_{z,f}$	Front vertical suspension stiffness
$K_{z,r}$	Rear vertical suspension stiffness
K_θ	Pitch stiffness
$K_{\phi,f}$	Roll stiffness front
$K_{\phi,r}$	Roll stiffness rear
L	Wheelbase
l_f	Distance from front axle to centre of gravity
l_r	Distance from rear axle to centre of gravity
m	Total mass of vehicle
$\mathbf{M}_{k,1}$	Measurement noise covariances matrix first update
$\mathbf{M}_{k,2}$	Measurement noise covariances matrix second update
m_s	Sprung mass of vehicle
M_z	Yaw moment
\mathbf{n}_A	Zero mean white Gaussian noise accelerometers
\mathbf{n}_G	Zero mean white Gaussian noise gyroscopes
n_v	Measurement noise velocity
\mathbf{P}_k	Kalman error covariance matrix
\mathbf{Q}	Process noise covariance matrix
\mathbf{Q}_k	Process noise covariance matrix at time step k
\mathbf{R}	Measurement noise covariance matrix
\mathbf{R}_k	Measurement noise covariance matrix at time step k
\mathbf{R}_{rot}	Rotation matrix
$\mathbf{R}_{rot,k}$	Rotation matrix at time step k
S_{ij}	Combined slip per wheel
s_x	Longitudinal slip
s_y	Lateral slip
t_s	Sampling time interval
\mathbf{u}	Continuous input vector
\mathbf{u}_k	Discrete input vector
\mathbf{v}_k	Measurement noise vector
v_x	Longitudinal velocity
v_{xk}	Longitudinal velocity per time step
$v_{x,i,j}$	Longitudinal velocity at corners of the vehicle
$v_{x,i,j,tyre}$	Longitudinal velocity at tyres at corners of the vehicle
v_y	Lateral velocity
$v_{y,i,j}$	Lateral velocity at corners of the vehicle
v_{yk}	Lateral velocity per time step
v_z	Vertical velocity
v_{zk}	Vertical velocity per time step
\mathbf{w}_k	Process noise vector
\mathbf{x}	Continuous state vector
$\dot{\mathbf{x}}$	Derivative continuous state vector
\mathbf{x}_k	Discrete state vector
$\hat{\mathbf{x}}_k$	Discrete state estimate vector
xyz	Body fixed coordinate system
XYZ	Global coordinate system
\mathbf{y}_{A_k}	Accelerometer measurements vector
\mathbf{y}_{G_k}	Gyroscope measurements vector
\mathbf{y}_k	Discrete output vector
y_{v_x}	Speed reading from the vehicle
\mathbf{z}	Continuous output vector
\mathbf{z}_k	Discrete output vector
$\mathbf{z}_{k,1}$	Measurement vector first update
$\mathbf{z}_{k,2}$	Measurement vector second update

α_{ij}	Side slip angle
α_k	External acceleration component
$\mathbf{\alpha}_k$	External acceleration component vector
δ_f	Front steering angle
δ_k	Measurement noise
δ_{kl}	Kronecker delta
ϵ	Error of the model
θ	Pitch angle
θ_k	Pitch angle at time step k
$\dot{\theta}$	Pitch rate
$\ddot{\theta}$	Pitch acceleration
κ_{ij}	Longitudinal tyre slip
μ	Tyre/road friction coefficient
σ_A^2	Variance accelerometer noise
σ_G^2	Variance gyroscope noise
σ_v^2	Variance velocity noise
Σ_A	Covariance matrix accelerometer noise
Σ_G	Covariance matrix gyroscope noise
Σ_{GV}	Covariance matrix velocity and gyroscope product terms noise
Σ_{α_k}	Covariance matrix contribution based on estimation $\mathbf{\alpha}_k$
$\mathbf{Y}_{k,1}$	Measurement noises matrix 1
$\mathbf{Y}_{k,2}$	Measurement noises matrix 2
ϕ	Roll angle
ϕ_k	Roll angle at time step k
$\dot{\phi}$	Roll rate
$\ddot{\phi}$	Roll acceleration
Φ_k	State transition matrix
ψ	Yaw angle
$\dot{\psi}$	Yaw rate
$\ddot{\psi}$	Yaw acceleration
ω_{ij}	Wheel velocities
$\boldsymbol{\omega}_k$	True angular rate vector
ω_{x_k}	True angular rate about x-axis
ω_{y_k}	True angular rate about y-axis
ω_{z_k}	True angular rate about z-axis

Acknowledgements

I want to thank firstly my supervisor Barys Shyrokau for all the fruitful discussions and his excellent guidance during the course of my thesis. Without his guidance I would not have finished this thesis in a successful manner.

I also want to thank Riender Happee and the rest of the WEpod comfort group for their constructive comments on my literature colloquium presentation.

A.J.F.D. Fritz
Delft, November 28, 2018



Introduction

1.1. Background

The automotive industry is continuously improving the safety and comfort of the vehicles. To further increase the safety and comfort, the automotive industry is focusing more on improving driver assistance systems and also on making the vehicles autonomous. Driver assistance systems take over certain tasks of the driver, such as for example adaptive cruise control, where the vehicle drives at a predefined velocity and brakes when the car in front slows down. Another example is a city safety system, where the vehicle first warns the driver if it detects a pedestrian or cyclist that is likely to hit the vehicle and then brakes automatically if the pedestrian or cyclist comes too close. The use of such driver assistance systems as described above can lead to an increase of the road safety, because unlike humans, sensors of a vehicle do not get distracted. Driver assistance systems are not only beneficial to the road safety, but also to the driver, because he or she has to focus less on certain driving tasks.

The downside of most driver assistance systems is that most of them can be switched off. If for example the vehicle gives unnecessary warnings the driver could get annoyed and turns the system off, which is not beneficial to the road safety. With autonomous vehicles the driver is not responsible of driving the vehicle anymore and is taken out of the loop. Making the vehicle responsible for the driving task is not only beneficial to the road safety, but also for the driver. Since the driver does not have to pay attention to the road anymore, it opens up possibilities for him/her to do other things while being on the road. Another advantage of making vehicles autonomous is that when vehicles start to communicate with other vehicles and also with the infrastructure the road capacity can be increased. If vehicles communicate with each other they can drive much closer together, because they know when a vehicle brakes. Lastly when a vehicle communicates with the infrastructure such as traffic lights, the traffic flow can be increased, by making the traffic light green just when the vehicle arrives at an intersection.

In order for the autonomous vehicles to drive safely on the road it is essential that the vehicle has accurate knowledge of all the states of the vehicle. These states include the vehicle velocities in longitudinal and lateral directions. The accelerations in longitudinal, lateral and vertical directions and also the vehicle attitude, so the roll, pitch and yaw angles. This information is used to plan the desired course of the vehicle and is also needed in the safety systems of the vehicle.

Some of these states can be measured by sensors, for example, in the case of non-slip conditions, the longitudinal velocity can be calculated using the wheel speed sensors installed at each wheel of the vehicle. Others like lateral velocity cannot be measured by sensors and need to be estimated accurately. To determine the exact position of the vehicle on the road, global positioning system (GPS) is used in conjunction with many other sensors. For example radars are used to measure distances to other vehicles on the road.

To measure distances to other vehicles and detect pedestrians not only radars are used, but also a stereo camera. A stereo camera consists of two cameras mounted at a fixed distance from each other, which is visualised in Figure 1.1. By comparing the images of the two cameras, distances can be estimated using disparity between the two images. The function of the camera is affected by the movements of the vehicle's body [1–3]. If the vehicle goes through a corner, the vehicle's body starts to roll in the opposite direction of the corner. The same applies for the braking of the vehicle, where the vehicle's body dives forward. These movements are called the roll and pitch movement of a vehicle. The distances that are estimated by the stereo camera are affected by these roll and pitch movements. By measuring or estimating the roll and pitch angle, the images of the stereo camera can be corrected so that proper functioning of the camera can be guaranteed.

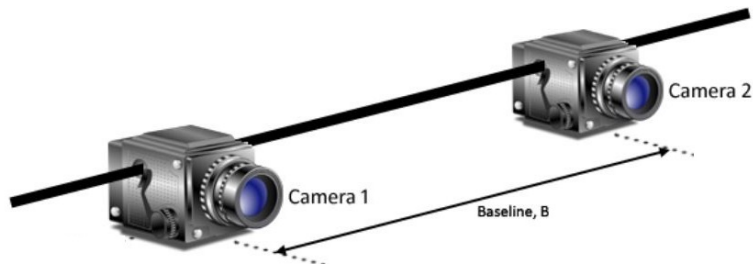


Figure 1.1: Visualisation of a stereo camera, taken from [3]

The roll and pitch angle are not only used for the stereo camera corrections, but they are also used in safety/comfort related systems. Examples are roll stability control systems [4]. The way that such a system works, is that the roll angle that is measured or estimated is continuously compared with a threshold. If the roll angle stays below the threshold the vehicle is stable and unlikely to roll over. If the threshold is exceeded roll-over of the vehicle is likely to happen and action is needed. In [4] an yaw moment, which is a torque about the vehicle's vertical axis, is generated using the brakes of the vehicle to prevent the vehicle to roll-over. To ensure proper working of such a system it is essential that the roll angle measurement or estimate is accurate and does not drift away over time, otherwise the roll stability control system could be activated unnecessarily.

Lastly the roll and pitch angle are used in the assessment of the comfort of the vehicles. Especially in autonomous vehicles motion sickness is a problem [5]. The three main reasons that contribute to motion sickness are the conflict between vestibular and visual inputs, inability to anticipate to the direction of motion and lack of control over the direction of motion [5]. These effects are especially present in autonomous vehicles where the passengers have no control over the vehicle anymore. In literature [6] it has been shown that when the roll and pitch angle vary at certain frequencies the motion sickness is triggered. By measuring the roll and pitch angle, these frequencies can be detected and if the vehicle has adaptive suspension, the suspension settings could be changed so that these frequencies are avoided.

1.2. Problem

The most simple way of determining the roll and pitch angle is by using gyroscopes. Gyroscopes measure angular rates. In this case the roll and pitch angle could be obtained by integrating the angular rates with respect to time. Determining the roll and pitch angle in this way would require accurate gyroscopes, because any noise or bias will be accumulated in the integration process causing the calculated roll and pitch angle to drift away from the real values over time. Gyroscopes that fulfil the requirements of having low noise and bias are expensive [7] and could even cost more than the actual vehicle.

In practice cheap low quality gyroscopes are used in vehicles as standard sensors. In order to accurately determine the roll and pitch angle with such gyroscopes, other sensors are used to correct the drift of the gyroscopes. The measurements of the different sensors are then fused together into an observer to accurately estimate the roll and pitch angle. The observer has to run real time in order to be used e.g. for the image correction of the stereo camera.

Most of the observers in literature that estimate the roll and pitch angle can be divided into two groups: vehicle dynamic model based and sensor kinematics based [8]. The vehicle dynamic model based observers have an internal vehicle model that calculates the states of the vehicle. In general most internal vehicle models are then implemented in some form of a Kalman filter. In the Kalman filter the internal vehicle model is corrected using actual sensor data. In this thesis an observer that is based on an internal vehicle model is called a dynamic observer. The main challenge of a dynamic observer is to have an internal vehicle model that has sufficient dynamics in it to calculate the states accurately, while being sufficient enough for real-time computation.

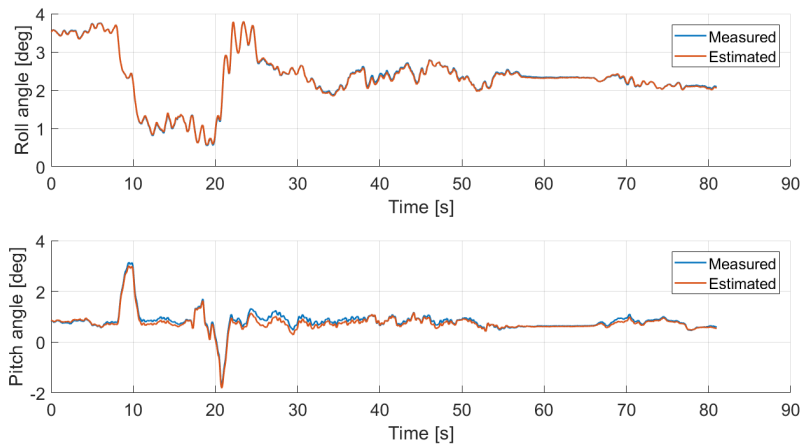


Figure 1.2: Estimation performance kinematic observer normal drive WEpod

The other observer group is purely based on sensor kinematics. These observers don't have an internal vehicle model that calculates the states first, which are then corrected by using actual measurements. Instead they use kinematic relations and general properties of sensors to estimate the roll and pitch angle. One of the properties of an accelerometer for example is that accelerometers not only measure the accelerations of the vehicle, called the external accelerations, but also the gravitational acceleration components. If the external accelerations are removed or when the vehicle standing still, the vector sum of the accelerometers equals the gravitational constant.

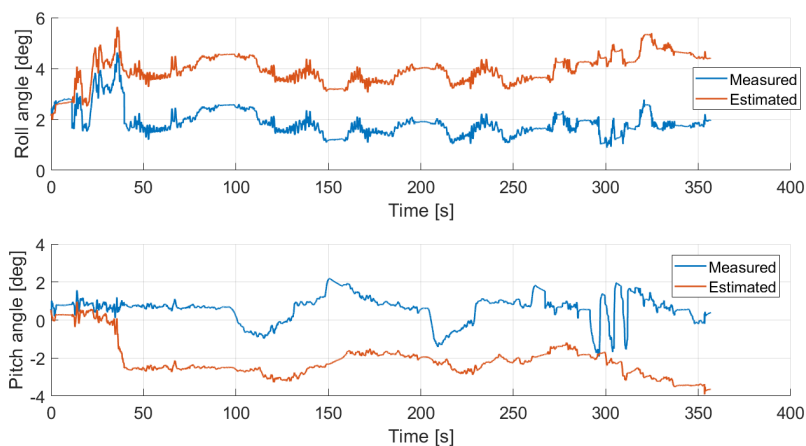


Figure 1.3: Estimation performance kinematic observer during emergency braking and hard cornering of the WEpod

The advantage of using a kinematic observer is that unlike a dynamic observer no knowledge is needed of vehicle mass-geometry properties. This means that the observer can be implemented in every vehicle without any tuning of parameters needed. The downside of a kinematic observer is that in extreme driving situations, such as emergency braking or hard cornering the kinematic relations cannot capture all the motions of the vehicle anymore, because kinematic relations do not take into account tyre behaviour [9]. This leads to an inaccurate estimation of the roll and pitch angles.

The effect of not taking into tyre behaviour can also be seen in Figure 1.2 and 1.3. In Figure 1.2 the estimation performance of a kinematic observer developed by Ahmed and Tahir [7] can be seen of a normal drive of an autonomous vehicle called WEpod. It can be observed that the estimates of the roll and pitch angle follow the measured values well. If the vehicle starts braking very hard and also does some hard cornering the estimates of the roll and pitch angle drift away as can be seen in Figure 1.3, because the tyre behaviour of the vehicle is not taken into account by the observer.

A dynamic observer can take into account tyre behaviour, which should lead to better estimation performance during manoeuvres such as hard cornering and emergency braking. In order to function properly a dynamic observer requires some knowledge of the vehicle parameters, such as the location of the centre of gravity (COG) and the mass distribution of the vehicle, which could be seen as a downside. This downside is compensated by the prospect of accurate estimation results even under extreme driving situations.

1.3. Thesis

In this thesis a dynamic observer is developed which is based on an exponential tyre model. The internal vehicle model is implemented into an Extended Kalman Filter (EKF). The exponential tyre model is chosen because it takes into account 3 dominant effects of the tyre behaviour, which are tyre force saturation, combined slip and varying normal loads. The derivations of the exponential tyre model, which are needed for the EKF, are relatively simple to calculate. This is important because the algorithm should still be able to run real time. The main goal of the dynamic observer is to give accurate estimation results of the roll and pitch angle. Since it is desired to have as much information of the vehicle states as possible, the lateral velocity is also estimated, because it cannot easily be measured by sensors. The lateral velocity is used to calculate the vehicle side slip angle. Having an accurate estimate of the vehicle side slip could lead to the development of new safety systems and improving existing ones like Electronic Stability Control (ESC) [10].

The estimation performance of the dynamic observer is not only compared to the real roll and pitch angles, but also compared to the estimation performance of a kinematic observer that was recently developed. The kinematic observer was developed by Ahmed and Tahir [7]. The observer uses kinematic relations to remove external accelerations of the accelerometer, so that the accelerometer can be used as the correcting sensor for the gyroscope.

The contribution of this thesis to the scientific field is that an exponential tyre model is used for the calculation of the roll and pitch angle in the internal vehicle model of the dynamic observer. Another contribution is that this thesis not only compares the performance of the dynamic observer against the real roll and pitch angles, but also against a kinematic observer, to see what the estimation improvement is when including dynamic relations.

The research question that is answered in this thesis is:

Does incorporating a vehicle dynamic model in an observer increase the performance compared to an observer that is only based on kinematic relations?

1.4. Outline

To answer the research question the report is structured as follows. First in Chapter 2 the concept of state estimation is introduced. In Chapter 3 the dynamic observer is developed and presented and in Chapter 4 the kinematic observer is presented. To test the performance of the observer first in Chapter 5 the simulation environment and the different test manoeuvres are discussed. The results of the simulations can be seen in Chapter 6. Lastly in Chapter 7 the conclusion and recommendations can be found.

2

Estimation Principles

In this chapter the roll, pitch and yaw angle are defined. Then the different sensors that can be used for estimating the roll and pitch angle are explained. Lastly the concept of state estimation is explained by presenting the working principle of a Kalman filter.

2.1. Definition of Roll, Pitch and Yaw Angle

The roll, pitch and yaw angle, ϕ , θ and ψ , respectively, can be defined by introducing the coordinate systems of the vehicle. There are two coordinate systems: one coordinate system which is fixed in space, called the global coordinate system denoted with capital XYZ . The other coordinate system is fixed to the COG of the vehicle and moves in space with the vehicle seen from the global coordinate system. This coordinate system is called the body fixed coordinate system and is denoted with xyz . In Figure 2.1 the coordinate systems of the vehicle are visualised according to the ISO standard.

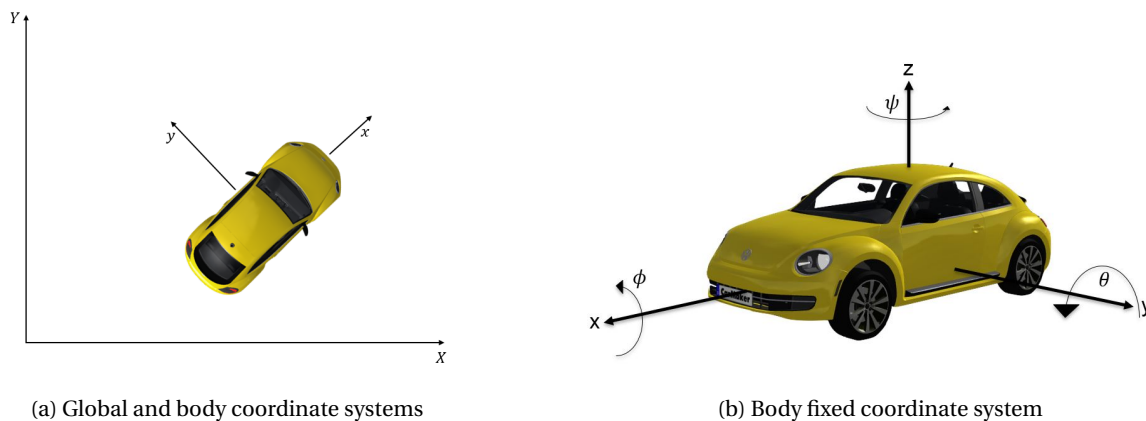


Figure 2.1: Coordinate systems of the vehicle

The body fixed coordinate system can be seen in Figure 2.1b. The x-axis is parallel with the centre line of the vehicle, the y-axis is defined positive to the left of the vehicle and the z-axis is defined positive in the upward direction. The roll angle ϕ is defined as the angle about the x-axis and is positive when the vehicles body rolls from left to right. The pitch angle θ is the angle about the y-axis and is defined positive when the vehicles body dives forward, so during braking. Lastly the yaw angle ψ is defined about the z-axis and is defined positive when the vehicle makes a turn to the left. All angles can be seen in Figure 2.1b.

2.2. Sensors

The gyroscope, which was already mentioned in the introduction, is not the only sensor that can be used to measure the roll and pitch angle. In fact there are many different sensors that can be used to measure the roll

and pitch angle. In Barnada et al. [11] for example, the stereo camera is not only used for object detection, but also to estimate the roll and pitch angle. In the paper it remains however unclear if the proposed algorithm can run real time. In the subsections below the gyroscope and two of the most common sensors used in literature to measure the roll and pitch angle are discussed in detail.

2.2.1. Gyroscope

Using a tri-axial gyroscope the angular velocities along all three axis of the vehicle as defined in Section 2.1 can be measured. The angular velocities are then integrated with respect to time to obtain the vehicle's body angles. Determining the roll and pitch angle this way requires extremely high accuracy gyroscopes [7], because in the integration process any noise or bias will be accumulated. As a result of the accumulated noise or bias in the integration process, the calculated roll and pitch angle can drift away from the real roll and pitch over time.

Automotive gyroscopes use ring-laser or fibre-optic technology, which can reach the necessary level of accuracy, but can cost more than the vehicle itself [7] and due to this high cost it means that these gyroscopes are not an option in production vehicles. Ring-laser and fibre-optic gyroscopes are mostly used as a reference, as for example in [7, 12], they are used to check if the proposed algorithm functions well. With Micro-Electro-Mechanical Systems (MEMS) technology gyroscopes and accelerometers are developed which are available at a very low cost, but the accuracy of these gyroscopes are too low to be used as a direct measurement [13], so these gyroscopes have to be used in conjunction with accelerometers, creating an inertial measurement unit (IMU) and a specific filtering algorithm has to be used that compensate of the drift that these gyroscopes introduce.

In Table 2.1 the specifications and prices can be seen of 8 gyroscopes. It can be observed that the price of the cheapest MEMS gyroscope is a fraction of the most expensive gyroscope, but the noise density and drift error are much larger than the expensive gyroscopes.

Table 2.1: Specifications and prices (Jan 2016) of different gyroscopes, taken from [7]

	Name	Manufacturer	Technology	Noise Density dps/\sqrt{Hz}	Drift Error (deg/h)	Price (USD)
1	TG-6000	KVH	Fibre Optic	0.001	1	30000
2	HG1700AG37	Honeywell	Ring Laser	0.002	1	22000
3	VG700MB	Crossbow	Fibre Optic	0.006	< 20	12000
4	HG1700AG68	Honeywell	Ring Laser	0.008	5	9000
5	Landmark 10	Gladiator Tech	MEMS	0.012	25	2500
6	ADIS16355	Analog Devices	MEMS	0.033	25.2	600
7	MTi-1	Xsens	MEMS	0.01	10	70
8	L3GD20	ST Microelectronics	MEMS	0.03	108	10

2.2.2. Global Positioning System

In [14–16] GPS is used to determine the roll and pitch angles of a vehicle. GPS works with at least 24 satellites in space, which have very precise atomic clocks onboard, which are synchronised with each other and with the ground. The satellites continuously transmit data about their current time and position. GPS receivers or antennas receive the signals of multiple satellites and the receiver then uses the slight time delay between the signals to find its own position. In order for the receiver to find its position at least four signals must be received [17].

As mentioned in [14, 15] the sampling rate of GPS is low, typically not more than 10 Hz, while an IMU sensor samples at frequencies up to 200 Hz. A low sampling rate is not beneficial for accuracy, because it becomes difficult to capture the high dynamics of a vehicle. Another disadvantage of GPS is that it is susceptible to loss of signal, due to satellite blockages such as tunnels or high buildings [18, 19]. This means that sometimes it is not possible to update the vehicle states. It is due to this reason that GPS is not used in this report as a sensor, because continuous updates of the roll and pitch angle are desired.

2.2.3. Inertial Measurement Unit

The IMU sensor is the sensor that is used the most in literature [7, 15, 20–22] to estimate the vehicle's roll and pitch angle. An IMU sensor typically consists of three accelerometers and three gyroscopes mounted in a set of three orthogonal axes [22, 23]. The IMU sensor measures the acceleration and rotation in all three dimensions. The sampling frequency of the IMU sensor is typically about 100 Hz. As already explained in Section 2.2.1 with MEMS technology it became possible to construct IMU sensors at a very low cost, but the measurements contain large amounts of noise even under stable conditions [19], so filtering techniques or combinations with other sensors are used to accurately predict the vehicles angles, which will be done in this report. Apart from their low cost the other advantages of an IMU sensor are its small size and robustness, which makes it easy to mount the sensor in a production vehicle.

2.3. State Estimation

Since the roll and pitch angle have to be estimated, an estimation algorithm has to be used. There are a variety of estimation algorithms available. Examples are sliding mode observers [24], particle filtering [25], moving horizon estimation [26] and Kalman filtering [27]. The Kalman filter is most used in literature [7, 8, 12, 14, 21, 23, 28–34] for estimation of the roll and pitch angle, because its ease of implementation and robustness. The Kalman filter is also used in this report for the dynamic and kinematic observers. The kinematic observer uses a linear Kalman filter and the dynamic observer uses an extended Kalman filter. Both are explained below in detail.

2.3.1. Linear Kalman Filter

The Kalman filter is an algorithm that uses probability to estimate its states. The algorithm works in two steps. In the prediction step the Kalman filter produces estimates of the current state variables, along with their uncertainties using an internal model. This prediction is then used in the next step, which is called the measurement step, where the output of the prediction is compared with actual measurements. The estimates are updated using a weighted average, called the Kalman gain which is calculated based on the uncertainties. The Kalman gain puts more weight on estimates with higher certainty. These two steps are then repeated at every time step.

The advantages of a Kalman filter are that the algorithm can run real time and only uses the present input measurements and the previously calculated state and uncertainty matrix. This means that no additional information about the past is required, making the memory required relatively small compared to other estimators.

Below the working principle of the algorithm is explained in equations using a linear time-varying process model:

$$\begin{aligned}\mathbf{x}_{k+1} &= \mathbf{A}_k \mathbf{x}_k + \mathbf{B}_k \mathbf{u}_k + \mathbf{w}_k \\ \mathbf{y}_k &= \mathbf{C}_k \mathbf{x}_k + \mathbf{D}_k \mathbf{u}_k + \mathbf{v}_k\end{aligned}\quad (2.1)$$

where $\mathbf{x}_k \in \mathbb{R}^n$ is the state, $\mathbf{u}_k \in \mathbb{R}^m$ is the input, $\mathbf{y}_k \in \mathbb{R}^p$ is the output, $\mathbf{w}_k \in \mathbb{R}^n$ is the process noise and $\mathbf{v}_k \in \mathbb{R}^p$ is the measurement noise. Given a measurement sequence and an input sequence up to time step k

$$\mathbf{Y}_k = \{\mathbf{y}_i, \mathbf{u}_i : 0 \leq i \leq k\}$$

with Kalman filtering the best possible estimate $\hat{\mathbf{x}}_{k+1}$ of \mathbf{x}_{k+1} can be obtained. It is assumed that the noise has zero mean and is uncorrelated (white) noise [27]. The covariances

$$E\left\{\begin{bmatrix} \mathbf{w}_k \\ \mathbf{v}_k \end{bmatrix} \begin{bmatrix} \mathbf{w}_l^T & \mathbf{v}_l^T \end{bmatrix}\right\} = \begin{bmatrix} \mathbf{Q}_k & \mathbf{S}_k \\ \mathbf{S}_k^T & \mathbf{R}_k \end{bmatrix} \delta_{kl} = \sum_k \delta_{kl}$$

are assumed to be known. δ_{kl} is the Kronecker delta ($\delta_{kl} = 1$ if $k = l$, and else $\delta_{kl} = 0$). It is also assumed that there is some knowledge about the initial state \mathbf{x}_0 and covariance matrix \mathbf{P}_0 . It is assumed that

$$E\{\mathbf{x}_0\} = \bar{\mathbf{x}}_0 \quad \text{and} \quad E\{(\mathbf{x}_0 - \bar{\mathbf{x}}_0)(\mathbf{x}_0 - \bar{\mathbf{x}}_0)^T\} = \mathbf{P}_0$$

are known.

The general Kalman Filter algorithm can be given as [27, 35]:

Prediction step:

$$\hat{\mathbf{x}}_{k|k-1} = \mathbf{A}_k \hat{\mathbf{x}}_{k-1|k-1} + \mathbf{B}_k \mathbf{u}_k \quad (2.2)$$

$$\mathbf{P}_{k|k-1} = \mathbf{A}_k \mathbf{P}_{k-1|k-1} \mathbf{A}_k^T + \mathbf{Q}_k \quad (2.3)$$

Correction step:

$$\mathbf{K}_k = \mathbf{P}_{k|k-1} \mathbf{C}_k^T (\mathbf{C}_k \mathbf{P}_{k|k-1} \mathbf{C}_k^T + \mathbf{R}_k)^{-1} \quad (2.4)$$

$$\hat{\mathbf{x}}_{k|k} = \hat{\mathbf{x}}_{k|k-1} + \mathbf{K}_k (\mathbf{y}_k - \mathbf{C}_k \hat{\mathbf{x}}_{k|k-1} - \mathbf{D}_k \mathbf{u}_k) \quad (2.5)$$

$$\mathbf{P}_{k|k} = (\mathbf{I} - \mathbf{K}_k \mathbf{C}_k) \mathbf{P}_{k|k-1} \quad (2.6)$$

where the initialisation is done using $k := 0$,

$$\hat{\mathbf{x}}_{0|-1} := \bar{\mathbf{x}}_0 \quad \text{and} \quad \mathbf{P}_{0|-1} := \mathbf{P}_0$$

In equation (2.2) and (2.3) $\hat{\mathbf{x}}_{k-1|k-1}$ and $\mathbf{P}_{k-1|k-1}$ are the state estimate and error covariance matrix of the previous time step. $\hat{\mathbf{x}}_{k|k-1}$ and $\mathbf{P}_{k|k-1}$ are the state prediction estimate and error covariance matrix prediction based on the previous time step. In equation (2.5) and (2.6) $\hat{\mathbf{x}}_{k|k}$ and $\mathbf{P}_{k|k}$ are the corrected state estimate and error covariance matrix, based on the predicted state estimate and error covariance matrix.

Equations (2.2) and (2.3) are called the *a priori* estimates, because $\hat{\mathbf{x}}_{k|k-1}$ and $\mathbf{P}_{k|k-1}$ are calculated based on the linear time varying model and no measurements are taken into account in this step. In the correction step, equations (2.5) and (2.6) are called the *a posteriori* estimates. The Kalman gain \mathbf{K}_k in equation (2.4) is calculated such that it minimises the *a posteriori* error covariance. The Kalman gain is used in equation (2.5) and (2.6) to correct any errors that were introduced in the prediction step and a optimal state estimate is calculated.

2.3.2. Extended Kalman Filter

Many physical systems cannot be written in linear state space form as in equation (2.1). To also make it possible to estimate states of such nonlinear systems, the EKF was developed for nonlinear systems that can not be written in linear state space form. Consider the nonlinear system:

$$\mathbf{x}_{k+1} = f_k(\mathbf{x}_k, \mathbf{u}_k) + \mathbf{w}_k \quad (2.7)$$

$$\mathbf{y}_k = h_k(\mathbf{x}_k, \mathbf{u}_k) + \mathbf{v}_k \quad (2.8)$$

with the constraints

$$\mathbf{x}_k \in \mathbb{X}_k, \quad \mathbf{w}_k \in \mathbb{W}_k, \quad \mathbf{v}_k \in \mathbb{V}_k \quad (2.9)$$

In equation (2.7) and (2.8) the next time step of the state and the output of the system are nonlinear functions of the states and input. In the EKF algorithm equations (2.7) and (2.8) are linearized around the current estimate, so that the nonlinear system can be written in state space. The EKF algorithm looks similar to the linear case and can be given as [34]:

The prediction step as

$$\hat{\mathbf{x}}_{k|k-1} = f(\hat{\mathbf{x}}_{k-1|k-1}, \mathbf{u}_k) \quad (2.10)$$

$$\mathbf{P}_{k|k-1} = \mathbf{A}_k \mathbf{P}_{k-1|k-1} \mathbf{A}_k^T + \mathbf{Q}_k \quad (2.11)$$

The measurement update as

$$\mathbf{K}_k = \mathbf{P}_{k|k-1} \mathbf{H}_k^T (\mathbf{H}_k \mathbf{P}_{k|k-1} \mathbf{H}_k^T + \mathbf{R}_k)^{-1} \quad (2.12)$$

$$\hat{\mathbf{x}}_{k|k} = \hat{\mathbf{x}}_{k|k-1} + \mathbf{K}_k (\mathbf{y}_k - h(\hat{\mathbf{x}}_{k|k-1}, \mathbf{u}_k)) \quad (2.13)$$

$$\mathbf{P}_{k|k} = (\mathbf{I} - \mathbf{K}_k \mathbf{H}_k) \mathbf{P}_{k|k-1} \quad (2.14)$$

where \mathbf{A}_k and \mathbf{H}_k are the Jacobians of the system and sensor model respectively at each time step and where the initialisation was done using $k := 0$,

$$\hat{\mathbf{x}}_{0|-1} := \bar{\mathbf{x}}_0 \quad \text{and} \quad \mathbf{P}_{0|-1} := \mathbf{P}_0$$

The Jacobian matrices consists of all the first order partial derivatives of the state vector. The Jacobian matrix of the system model \mathbf{A} and sensor model \mathbf{H} are defined as

$$A_{ij} = \frac{\partial f_i(x, u)}{\partial x_j} \quad H_{lj} = \frac{\partial h_l(x, u)}{\partial x_j} \quad (2.15)$$

Where i and l are the lengths of the state and output vectors respectively and j is also the length of the state vector.

\mathbf{Q}_k and \mathbf{R}_k are the process and measurement noise covariance matrices respectively. Meaning that \mathbf{Q}_k is the matrix associated with the noise in the system states and \mathbf{R}_k is the covariance matrix of the measurement noise, which is either given by the manufacturer or can found from measurements. Finding the right measurement noise covariance matrix is not that easy and is generally constructed by trial and error, because the unmodeled dynamics and parameter uncertainties are generally not exactly known. The performance of the EKF is highly affected by \mathbf{Q}_k and \mathbf{R}_k , so it is of great importance to choose \mathbf{Q}_k and \mathbf{R}_k correctly [36].

The working principle of the EKF algorithm is the same as for the linear Kalman filter. Due to the calculation of the Jacobian matrices in each iteration, the computational load of the EKF can be high. If the EKF is intended for online parameter estimation, simplifications to the system equations should be considered to reduce the computational load.

3

Dynamic Observer

In this chapter the dynamic observer is developed. A nonlinear vehicle model is implemented in an EKF. The vehicle model consists of 9 degree of freedom (DOF). The DOF consists of the longitudinal and lateral planar motions of the vehicle, body roll, pitch and yaw motion and the rotational dynamics of the four wheels of the vehicle. First the internal vehicle model is presented and this is then implemented into an EKF.

3.1. Vehicle Modelling

The main goal of the dynamic observer is to give correct estimates of the roll and pitch angle. This is done by using an internal nonlinear vehicle model that gives accurate predictions of the roll and pitch angle. The observer is used in conjunction with a low cost IMU sensor. This makes it possible to also estimate the lateral velocity of the vehicle, by using the lateral accelerometer of the IMU sensor. The estimate of the lateral velocity can be used for calculation of the side slip angle, which is beneficial for safety systems such as ESC [10]. The performance of the observer is largely dependent on the accuracy of the internal vehicle model. If the dynamics of the internal vehicle model matches up with the true nonlinear behaviour of the vehicle, the model output error will be small, which leads to faster converge to the correct estimate and so the tracking of the states will be improved.

3.1.1. State Variables

To make sure that the dynamics of the internal vehicle model match up with the actual vehicle behaviour, it is of great importance to choose the correct state variables. To ensure proper functioning of the observer it is essential to have states that can be compared to actual sensor data. Below are the state variables that are chosen for the dynamic observer:

- v_y : lateral velocity in the centre of gravity
- $\dot{\psi}$: yaw rate around vehicles z-axis
- ϕ : roll angle around vehicles x-axis
- $\dot{\phi}$: roll rate around vehicles x-axis
- θ : pitch angle around vehicles y-axis
- $\dot{\theta}$: pitch rate around vehicles y-axis

The vehicle has several sensor outputs which are available. These outputs can be used as an input to the internal vehicle model. In this thesis the available inputs to the internal vehicle model are the front steering wheel angle δ_f and the rotational velocity of the four wheels of the vehicle ω_i . The outputs of the internal vehicle model, which are compared with the actual sensors of the vehicle are:

- a_y : lateral acceleration in the centre of gravity
- $\dot{\psi}$: yaw rate around vehicles z-axis
- $\dot{\phi}$: roll rate around vehicles x-axis
- $\dot{\theta}$: pitch rate around vehicles y-axis

In vector form the inputs \mathbf{u} , states \mathbf{x} and output \mathbf{z} can be summarised as:

$$\mathbf{u} = [\delta_f \quad \omega_{FL} \quad \omega_{FR} \quad \omega_{RL} \quad \omega_{RR}]^T$$

$$\mathbf{x} = [v_y \quad \psi \quad \phi \quad \dot{\phi} \quad \theta \quad \dot{\theta}]^T$$

$$\mathbf{z} = [a_y \quad \dot{\psi} \quad \dot{\phi} \quad \dot{\theta}]^T$$

Now that the input, state and output vector are defined, they can be used to write the internal vehicle model in a form so that it can later be used by the EKF. The system has to be written in the nonlinear state space form as

$$\dot{\mathbf{x}} = \mathbf{f}(\mathbf{x}(t), \mathbf{u}(t)) \quad (3.1)$$

$$\mathbf{z} = \mathbf{h}(\mathbf{x}(t), \mathbf{u}(t)) \quad (3.2)$$

3.1.2. Tyre Modelling

Now that the general form and states of the vehicle model are defined, a model of the tyre forces is developed, because the accuracy of the internal vehicle model of the estimator is for a large part dependent on correct modelling of the highly non-linear tyre forces. The tyre forces depend on the longitudinal and lateral slip, wheel suspension kinematics, vertical loads on the tyre, temperature, road texture, etc. In this thesis report only the three most dominant effects of the tyre force behaviour are taken into account. These are tyre force saturation, combined slip and vertical load dependency. Each is explained below.

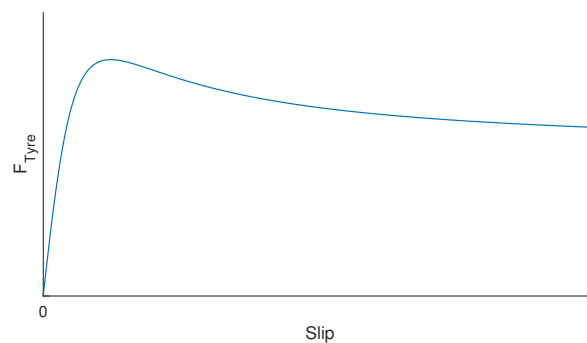


Figure 3.1: Effect of tyre saturation

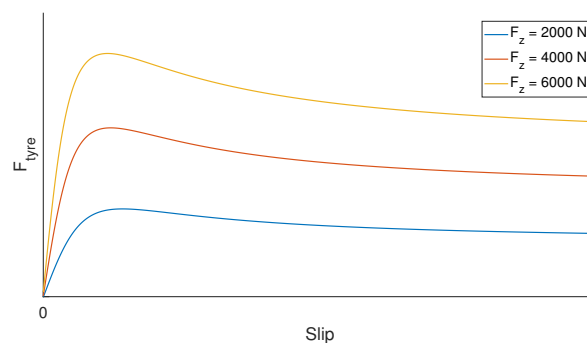


Figure 3.2: Effect of varying normal loads

The tyre saturation can be explained by the phenomenon that for large tyre slip, the tyre forces saturate at the maximum achievable peak friction value. In Figure 3.1 this peak can be observed. When the tyre slip further increases, the maximum tyre force that can be generated saturates or even decreases. In Figure 3.2 the effect of different normal loads on a tyre can be seen. Increasing the normal load leads to an increase

in generated tyre force. Lastly in Figure 3.3 the effect of combined slip can be seen. Having combined slip leads to a lower generated tyre force. The maximum amount of achievable lateral tyre slip is dependent on the amount of slip in the longitudinal direction and vice versa. For example, when braking during cornering, the lateral tyre force will collapse as the brake force increases.

Since the estimator has to be able to run online, the computational load of the tyre force calculation should be minimised. In an EKF the derivatives of the tyre model have to be calculated as well. Increasing the complexity of a tyre model significantly increases the complexity of calculating these derivatives [37, 38], this may mean that the estimator is not able to run online. The tyre model should be as simple as possible while still be able to cope with the non linearity's. An exponential tyre model is chosen as the preferred tyre model due to its simplicity. This model can still cope with the effects of tyre force saturation, combined slip and normal load variation and the derivatives required for the EKF can be easily calculated.

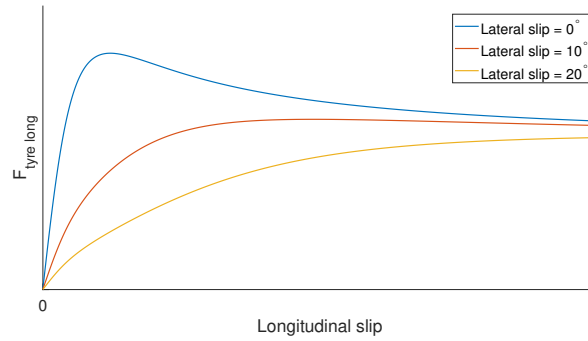


Figure 3.3: Effect of combined slip

In Figure 3.4 a comparison of the exponential tyre model with the Magic formula [39] can be seen. It can be observed that the overall shape of the exponential tyre model matches up with the Magic formula. Only the friction peak can not be modelled and at larger slip values there is a slight offset in the calculated tyre force. The exponential tyre model is tuned offline such that the friction peak and slip stiffness will closely match with the measured vehicle behaviour.

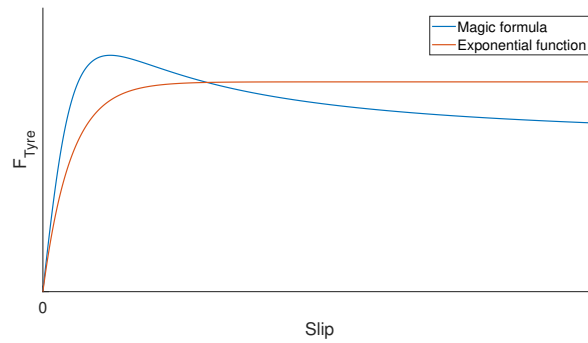


Figure 3.4: Tyre models comparison

For the exponential tyre model it is assumed that the longitudinal and lateral tyre forces are linearly dependent with the vertical tyre load F_z . To take combined slip into account in the tyre model a simplified relation is used. Since the lateral slip is dependent on the longitudinal slip and vice versa, the combined slip can be seen as the resultant between the two, as illustrated in Figure 3.5. This relation can be written as [38]

$$S = \sqrt{s_x^2 + s_y^2} \quad (3.3)$$

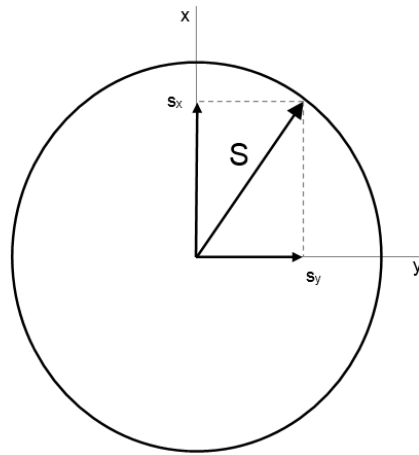


Figure 3.5: Effect of combined slip

In order to calculate the tyre slip at each corner of the vehicle, the velocities at the centre of gravity have to be transformed to each corner of the vehicle. Each wheel of the vehicle has separate longitudinal slip calculation which uses the transformed wheel velocity and rotational wheel velocity. This is done so that individual wheel braking (or traction) can be accounted for.

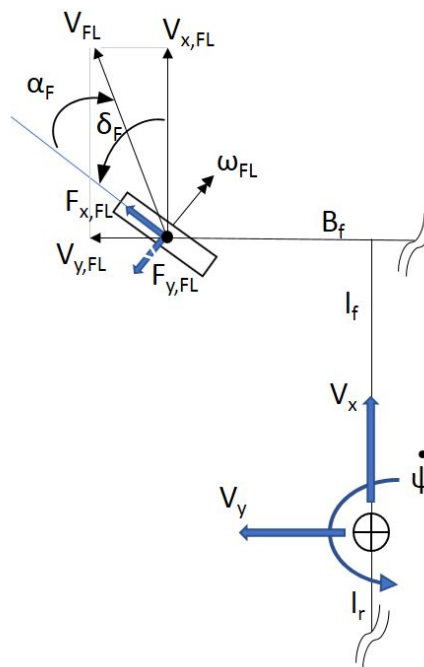


Figure 3.6: Transformation of velocities

To visualise the transformation of the velocities, the right front wheel is visualised, which can be seen in Figure 3.6. The same type of definition also applies to the other three wheels, but those are not visualised. The longitudinal and lateral velocities at each corner of the vehicle can be calculated using the following equations

$$v_{x,FL} = v_x - \frac{B_f}{2} \dot{\psi} \quad (3.4)$$

$$v_{x,FR} = v_x + \frac{B_f}{2} \dot{\psi} \quad (3.5)$$

$$v_{x,RL} = v_x - \frac{B_r}{2} \dot{\psi} \quad (3.6)$$

$$v_{x,RR} = v_x + \frac{B_r}{2} \dot{\psi} \quad (3.7)$$

$$v_{y,FL} = v_{y,FR} = v_y + l_f \dot{\psi} \quad (3.8)$$

$$v_{y,RL} = v_{y,RR} = v_y + l_r \dot{\psi} \quad (3.9)$$

Where l_f and l_r are the distances from the front and rear axles to the COG. In order to derive the longitudinal and lateral tyre forces, these velocities then have to be transformed to the local coordinate axis of the wheel. This is done by correcting the velocities with the steering angle.

$$v_{x,FL,tyre} = v_{x,FL} \cos(\delta_f) + v_{y,FL} \sin(\delta_f) \quad (3.10)$$

$$v_{x,FR,tyre} = v_{x,FR} \cos(\delta_f) + v_{y,FR} \sin(\delta_f) \quad (3.11)$$

$$v_{x,RL,tyre} = v_{x,RL} \cos(\delta_r) + v_{y,RL} \sin(\delta_r) \quad (3.12)$$

$$v_{x,RR,tyre} = v_{x,RR} \cos(\delta_r) + v_{y,RR} \sin(\delta_r) \quad (3.13)$$

Since the vehicle is only front steered, the rear steering angle is equal to zero which results in:

$$v_{x,RL,tyre} = v_{x,RL} \quad (3.14)$$

$$v_{x,RR,tyre} = v_{x,RR} \quad (3.15)$$

It is not necessary to correct the lateral velocities, since the tyre side slip angle is calculated directly using the steering angle. The tyre side slip equations are

$$\alpha_{FL} = \alpha_{FR} = \text{atan}\left(-\frac{v_{y,FL}}{v_x}\right) + \delta_f \quad (3.16)$$

$$\alpha_{RL} = \alpha_{RR} = \text{atan}\left(-\frac{v_{y,RL}}{v_x}\right) \quad (3.17)$$

To avoid divisions by zero, a condition is set to the side slip angle. It is only calculated when the longitudinal velocity is greater than 0.5 ms^{-1} . When the longitudinal velocity is smaller, the side slip angle is set to zero.

The longitudinal tyre slip can be calculated using the rotational velocities of the wheels and the longitudinal velocities in the local coordinates of the wheels. To guarantee numerical stability, a distinction in the definition of tyre slip is made between positive tyre slip as a result of acceleration and negative tyre slip due to braking. To avoid divisions by zero, the same condition is used as for the side slip angle. The positive longitudinal tyre slip of the tyres is defined as

$$\kappa_{ij} = 1 - \frac{v_{x,ij,tyre}}{R_w \omega_{ij}} \quad (3.18)$$

For negative longitudinal tyre slip as

$$\kappa_{ij} = \frac{R_w \omega_{ij}}{v_{x,ij,tyre}} - 1 \quad (3.19)$$

Where ij stand for each corner of the vehicle, defined as $ij = \{FL, FR, RL, RR\}$. R_w is the tyre radius and ω_{ij} the rotational velocity of each tyre. Now the longitudinal and side slip are defined, the combined slip vector from equation (3.3) can now be rewritten and is defined for each wheel as

$$S_{FL} = \sqrt{\alpha_{FL}^2 + \kappa_{FL}^2} \quad (3.20)$$

$$S_{FR} = \sqrt{\alpha_{FR}^2 + \kappa_{FR}^2} \quad (3.21)$$

$$S_{RL} = \sqrt{\alpha_{RL}^2 + \kappa_{RL}^2} \quad (3.22)$$

$$S_{RR} = \sqrt{\alpha_{RR}^2 + \kappa_{RR}^2} \quad (3.23)$$

The only equations that have to be defined are the equations of the vertical tyre load at each wheel. These forces change due to longitudinal and lateral load transfer. The longitudinal component of the vertical tyre force can be given as

$$F_z^{long} = m \frac{h_s}{2L} a_x \quad (3.24)$$

The lateral component is different for the front and rear of the vehicle and can be given as

$$F_{z,front}^{lat} = m \frac{l_r}{L} \frac{h_f}{B} a_y \quad (3.25)$$

$$F_{z,rear}^{lat} = m \frac{l_f}{L} \frac{h_r}{B} a_y \quad (3.26)$$

Combining equations (3.24), (3.25) and (3.26) with the static weight distribution of the vehicles gives [40]

$$F_{z,FL} = mg \frac{l_r}{2L} - F_z^{long} - F_z^{lat} \quad (3.27)$$

$$F_{z,FR} = mg \frac{l_r}{2L} - F_z^{long} + F_z^{lat} \quad (3.28)$$

$$F_{z,RL} = mg \frac{l_f}{2L} + F_z^{long} - F_z^{lat} \quad (3.29)$$

$$F_{z,RR} = mg \frac{l_f}{2L} + F_z^{long} + F_z^{lat} \quad (3.30)$$

Now that the combined slip vector and the vertical tyre forces are defined for each wheel, the exponential tyre model for each wheel is defined for the lateral force as [41]

$$F_{y,ij} = \mu F_{z,ij} \frac{\alpha_{ij}}{S_{ij}} \left(1 - e^{-K_{y,i} S_{ij}} \right) \quad (3.31)$$

The variable μ represents the tyre/road-friction coefficient. For dry asphalt μ is approximately equal to 1. The tuning of the slip characteristics is done using the linear tyre slip stiffness K_y .

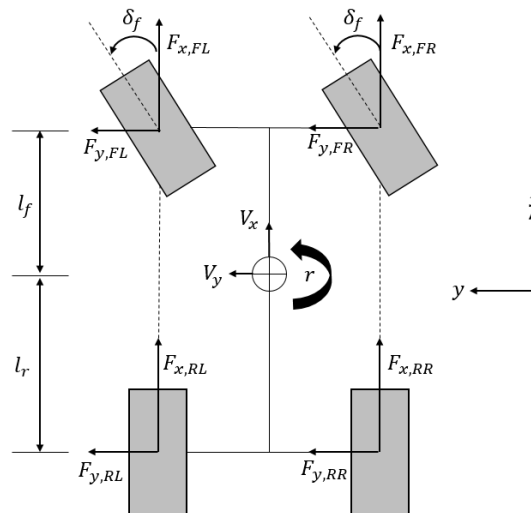


Figure 3.7: Degrees of freedom in-plane

3.1.3. State Equations

Now that the lateral tyre forces are calculated they can be used to calculate the states of the estimator. Below the equations related to the lateral velocity and yaw rate are derived. Looking at Figure 3.7 and starting with Newton's second law of motion and a moment balance around the z-axis gives:

$$ma_y = \sum F_y \quad (3.32)$$

$$I_{zz}\ddot{\psi} = \sum M_z \quad (3.33)$$

where $\sum F_y$ is the sum of the lateral tyre forces acting on the centre of gravity of the vehicle. $\sum M_z$ is the total yaw moment around the vertical z-axis. m and I_{zz} are the vehicle mass and inertia around the vertical axis respectively.

The lateral acceleration a_y is the sum of the derivative of the lateral velocity v_y and the centripetal acceleration [42], so $a_y = \dot{v}_y + \psi v_x$. Using the tyre forces from the previous section and rewriting equations (3.32) and (3.33) gives:

$$m(\dot{v}_y + v_x\dot{\psi}) = \sum F_y(v_x, v_y, \dot{\psi}, \delta_f, \omega_{ij}, F_{z,ij}, \mu) \quad (3.34)$$

$$I_{zz}\ddot{\psi} = \sum M_z(v_x, v_y, \dot{\psi}, \delta_f, \omega_{ij}, F_{z,ij}, \mu) \quad (3.35)$$

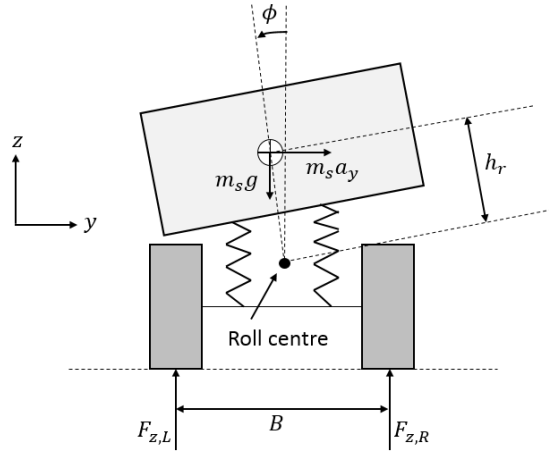


Figure 3.8: Roll degree of freedom, when looking at the vehicle from the front

The equations of the roll and pitch rates are derived below, which are used in the estimator for calculation of the roll and pitch angle. As with the yaw rate, a moment balance is also done, but now around the x-axis and y-axis to obtain the equations of the roll and pitch rates. Starting with the moment balance around the x-axis and looking at Figure 3.8 gives [8, 33, 40]

$$I_{xx}\ddot{\phi} = m_s g h_r \sin(\phi) + m_s a_y h_r \cos(\phi) - (K_{\phi f} + K_{\phi r})\phi - (C_{\phi f} + C_{\phi r})\dot{\phi} \quad (3.36)$$

where h_r is the distance from the vehicle's COG to the roll axis. $K_{\phi f}$ and $K_{\phi r}$ are the front and rear roll stiffnesses respectively. $C_{\phi f}$ and $C_{\phi r}$ are the front and rear roll damping coefficients respectively. a_y is calculated using the relation (3.32). Since a_y is calculated using lateral forces, equation (3.36) can be written as

$$I_{xx}\ddot{\phi} = m_s g h_r \sin(\phi) + m_s \frac{\sum F_{y,ij}}{m} h_r \cos(\phi) - (K_{\phi f} + K_{\phi r})\phi - (C_{\phi f} + C_{\phi r})\dot{\phi} \quad (3.37)$$

The derivative of the roll angle ϕ with respect to time equals $\dot{\phi}$. Recalling that the state vector was defined as

$$\mathbf{x} = [v_y \quad \dot{\psi} \quad \phi \quad \dot{\phi} \quad \theta \quad \dot{\theta}]^T$$

The derivative of the third element of the state vector, which is the roll angle, becomes now equal to the fourth element of the state vector.

The pitch rate can be derived in the same manner as the roll rate. Starting with a moment balance around the y-axis gives [33]

$$I_{yy}\ddot{\theta} = m_s g h_p \sin(\theta) - m_s a_x h_p \cos(\theta) - K_\theta \theta - C_\theta \dot{\theta} \quad (3.38)$$

where h_p is the distance from the vehicle's COG to the pitch axis. K_θ and C_θ are the pitch stiffness and pitch damping coefficient respectively.

The derivative of the pitch angle can be obtained in the same manner as that of the roll angle. Looking at the definition of the state vector, the derivative of the fifth element, which is the pitch angle, becomes equal to the sixth element of the state vector.

Now that all state equations are defined they can be rewritten in a nonlinear state space form. Recalling that the state and input vector were defined as

$$\mathbf{x} = [v_y \quad \dot{\psi} \quad \phi \quad \dot{\phi} \quad \theta \quad \dot{\theta}]^T$$

$$\mathbf{u} = [\delta_f \quad \omega_{FL} \quad \omega_{FR} \quad \omega_{RL} \quad \omega_{RR}]^T$$

then renaming the state and input variables as x_1, x_2, \dots, x_6 and u_1, u_2, \dots, u_5 , the nonlinear state space form can be written as

$$\dot{\mathbf{x}} = \begin{bmatrix} \frac{1}{\eta u} (F_{y,FL} + F_{y,FR} + F_{y,RL} + F_{y,RR}) - v_x x_2 \\ \frac{1}{I_{zz}} (l_f (F_{y,FL} + F_{y,FR}) - l_r (F_{y,RL} + F_{y,RR})) \\ x_4 \\ \frac{1}{I_{xx}} (m_s g h_r \sin(x_3) + m_s \frac{\sum F_{y,ij}}{m} h_r \cos(x_3) - (K_{\phi_f} + K_{\phi_r}) x_3 - (C_{\phi_f} + C_{\phi_r}) x_4) \\ x_6 \\ \frac{1}{I_{yy}} (m_s g h_p \sin(x_5) - m_s a_x h_p \cos(x_5) - K_\theta x_5 - C_\theta x_6) \end{bmatrix} \quad (3.39)$$

3.2. Estimator

Now that the internal vehicle dynamic model is defined, it can be implemented in an EKF. First the general structure of the estimator is presented. Then the structure of the required Jacobians and the assumptions made to calculate them are given. Lastly the initialisation and tuning of the observer is presented.

3.2.1. Extended Kalman Filter Structure

The internal vehicle model in the previous section was given in continuous form. In order to use it in an EKF it has to be discretized. The continuous vehicle model is converted into discrete time using the relations:

$$\mathbf{x}_k = \mathbf{x}_{k-1} + \dot{\mathbf{x}} t_s \quad (3.40)$$

$$\mathbf{z}_k = \mathbf{z} \quad (3.41)$$

where t_s is the sampling time interval and k is the time step. $\dot{\mathbf{x}}$ and \mathbf{z} are the state and output equations of the internal vehicle model as defined in equations (3.1) and (3.2).

Now that the internal vehicle model is discretized it can be used in the EKF. In Chapter 2 the general structure of the EKF was already presented, but is repeated below

The prediction step is given as

$$\hat{\mathbf{x}}_{k|k-1} = f(\hat{\mathbf{x}}_{k-1|k-1}, \mathbf{u}_k) \quad (3.42)$$

$$\mathbf{P}_{k|k-1} = \mathbf{A}_k \mathbf{P}_{k-1|k-1} \mathbf{A}_k^T + \mathbf{Q} \quad (3.43)$$

and the measurement update:

$$\mathbf{K}_k = \mathbf{P}_{k|k-1} \mathbf{H}_k^T (\mathbf{H}_k \mathbf{P}_{k|k-1} \mathbf{H}_k^T + \mathbf{R})^{-1} \quad (3.44)$$

$$\hat{\mathbf{x}}_{k|k} = \hat{\mathbf{x}}_{k|k-1} + \mathbf{K}_k (\mathbf{y}_k - h(\hat{\mathbf{x}}_{k|k-1}, \mathbf{u}_k)) \quad (3.45)$$

$$\mathbf{P}_{k|k} = (\mathbf{I} - \mathbf{K}_k \mathbf{H}_k) \mathbf{P}_{k|k-1} \quad (3.46)$$

In the prediction step the nonlinear internal vehicle model is used to make a prediction of the state estimate and error covariance matrix. For the prediction of the error covariance matrix a Jacobian matrix of the system model is calculated, which is a linearization of the nonlinear model. In the measurement update the outputs of the nonlinear model are compared to the actual sensor measurements, which is then used to correct the state estimate. In the correction of the error covariance matrix a Jacobian matrix of the sensor model is calculated. It should be noted that in the above equations the process noise and measurement noise covariance matrices are not dependent on time step k . This means they are modelled as constants.

The Jacobian matrix of the system model \mathbf{A} is defined as

$$A_{ij} = \frac{\partial f_i(x, u)}{\partial x_j} \quad \text{with } i = \{1, 2, 3, 4, 5, 6\} \quad \text{and } j = \{1, 2, 3, 4, 5, 6\} \quad (3.47)$$

and the Jacobian of the sensor model \mathbf{H} as

$$H_{ij} = \frac{\partial h_i(x, u)}{\partial x_j} \quad \text{with } i = \{1, 2, 3, 4\} \quad \text{and } j = \{1, 2, 3, 4, 5, 6\} \quad (3.48)$$

It should be noted that the Jacobian elements are numbered according to the definition of the state and output vectors as in Section 3.1.1.

3.2.2. Calculation Jacobian Elements

A large part of the computational load is accounted by the calculation of the partial derivatives in the Jacobians. Any simplification that can be done, which does not affect the final result helps to reduce this computational load. Since a large part of the computational load lies in the calculation of the Jacobians with respect to the tyre forces, a few simplifications are done in these calculations.

The first simplification in the calculation of the Jacobians is not to take the combined slip into account. Above that an additional simplification is made. The arctan in equations (3.16) and (3.17) is neglected, which leads to the following definition of the side slip angles

$$\alpha_{FL} = \alpha_{FR} = -\frac{v_{y,FL}}{v_x} + \delta_F \quad (3.49)$$

$$\alpha_{RL} = \alpha_{RR} = -\frac{v_{y,RL}}{v_x} \quad (3.50)$$

The lateral tyre forces for positive and negative side slip α are now defined for the left front wheel as, for positive α

$$F_{y,FL} = \mu F_{z,FL} \left(1 - \exp^{-K_{y,F} \left(\frac{-v_{y+1_f} \dot{\psi}}{v_x} + \delta \right)} \right) \quad (3.51)$$

and for negative α

$$F_{y,FL} = -\mu F_{z,FL} \left(1 - \exp^{K_{y,F} \left(\frac{-v_{y+1_f} \dot{\psi}}{v_x} + \delta \right)} \right) \quad (3.52)$$

In the same manner the lateral tyre force equations are defined for the other three wheels. Now that the tyre force equations used for the partial derivatives are defined for positive and negative slip values, the derivatives can be calculated. Further details of the calculation of the derivatives can be seen in Appendix A.

Simplifications were also made in the calculation of the derivatives with respect to the roll and pitch rates. Since the roll and pitch angle is typically only a few degrees, for the calculation of the derivatives the small angle approximation is used on equations (3.37) and (3.38). For the small angle approximation it is assumed that

$$\begin{aligned}\cos(x) &\approx 1 \\ \sin(x) &\approx x\end{aligned}$$

Using these approximations results in the following equation for the roll rate

$$\ddot{\phi} = \frac{1}{I_{xx}} \left(m_s g \phi + m_s \frac{\sum F_{y,ij}}{m} h_r - (K_{\phi f} + K_{\phi r}) \phi - (C_{\phi f} + C_{\phi r}) \dot{\phi} \right) \quad (3.53)$$

And for the pitch rate

$$\ddot{\theta} = \frac{1}{I_{yy}} \left(m_s g \theta - m_s a_x h_p - K_{\theta} \theta - C_{\theta} \dot{\theta} \right) \quad (3.54)$$

Further details of the calculation of the derivatives of the roll and pitch rates can again be seen in Appendix A.

3.2.3. Initialisation and Tuning

In order to guarantee proper working of the dynamic observer it is essential to initialise the observer correctly and tune it properly. This needs to be done for every new type of vehicle the dynamic observer is used in. Starting with the initialisation. For the internal vehicle model of the observer several parameters of the vehicle are needed to be defined to accurately calculate the dynamics. Below these parameters are summarised.

m	Total mass of the vehicle, kg
m_s	Sprung mass of the vehicle, kg
I_{xx}	Body inertia around x-axis, kg m ²
I_{yy}	Body inertia around y-axis, kg m ²
I_{zz}	Body inertia around z-axis, kg m ²
L	Wheelbase, m
l_f	Distance from front axle to COG, m
h_{cg}	Height of vehicles COG above the road, m
b_f	Front track width, m
b_r	Rear track width, m
h_{roll}	Height of roll axis above the road, m
h_{pitch}	Height of pitch axis above the road, m
$K_{z,f}$	Front vertical suspension stiffness, N m ⁻¹
$K_{z,r}$	Rear vertical suspension stiffness, N m ⁻¹
$D_{z,f}$	Front vertical suspension damping, N s m ⁻¹
$D_{z,r}$	Rear vertical suspension damping, N s m ⁻¹

Once these parameters are correctly defined, the tyre forces needs be tuned. This is done by tuning the parameters $K_{y,f}$ and $K_{y,r}$. The sum of the tyre forces divided by the total mass of the vehicle gives the lateral acceleration of the vehicle. This sum is compared to the actual lateral acceleration of the vehicle. By tuning $K_{y,f}$ and $K_{y,r}$ the lateral acceleration calculated by the model will closely match the actual lateral acceleration and this also implies proper calculation of the tyre forces.

After tuning of the tyre forces the roll and pitch stiffnesses and damping are tuned, so that the calculated roll and pitch rate are close to the actual roll and pitch rate. Now that all parameters are tuned, the internal vehicle model should calculate roll and pitch angles that lie close to the actual roll and pitch angle.

The EKF is now used to give correct estimates of the roll and pitch angles, when sensor measurements are taken into account. For proper functioning of the EKF it is of great importance to select the proper process and measurement noise covariance matrices. The variances that are used in the measurement noise covariance matrix come from the sensors that are used to in the EKF. In this thesis the measurement noise covariance matrix consists of the variances of the IMU sensor. In most cases these variances are given by the manufacturer.

The process noise covariance matrix is not so trivial to select. As was already explained in Chapter 2, the unmodeled dynamics and parameter uncertainties are not exactly known. Choosing elements in the process noise covariance matrix that are too low with respect to the elements of the measurement noise covariance matrix, means that in the EKF more weight is put on the internal vehicle model. This could lead to under estimation of the states. Choosing elements of the process noise covariance matrix that are too high with respect to the elements of the measurement noise covariance matrix, means that in the EKF more weight is put on the measurements. This could lead to a larger drift error. The process noise covariance matrix is tuned until the Kalman filter gives satisfactory results.

4

Kinematic Observer

In this chapter a kinematic observer is presented which estimates the roll and pitch angle through sensor kinematics. This observer was developed by Ahmed & Tahir [7] and was designed to give accurate estimation results even when using low quality sensors. The observer consists of a Kalman filter, which uses velocity, accelerometer and gyroscope measurements to accurately estimate the roll and pitch angle.

4.1. Methodology

As was shown in Table 2.1 low cost gyroscopes suffer from drift. This drift needs to be corrected by another sensor in order to obtain accurate estimates of the roll and pitch angle. In [7] an accelerometer is used as the correcting sensor. The measurements of the accelerometer are corrected by removing the external accelerations of the vehicle. The external accelerations along the lateral and vertical axis are removable due to specific kinematic relations of a moving vehicle. The external acceleration in the longitudinal direction cannot be removed, but by obtaining correct gravitational accelerations along the lateral and vertical axes, the longitudinal gravitational acceleration component can be determined, because the norm of the gravitational accelerations in three directions is always equal to 9.81 ms^{-2} .

Since an accelerometer is a noisy sensor due to road vibrations, determining the longitudinal acceleration using the relation $A_{x_k} = \sqrt{9.81^2 - A_{y_k}^2 - A_{z_k}^2}$, where A denotes the accelerometer measurement, would create even more noise in the measurement of the longitudinal component. This issue is solved in [7] using a Kalman filter to implement the complete fusion process by considering the state vector as a three dimensional vector, representing the orientation of the vehicle with respect to the global coordinate system. The filter uses a two step process. First only the lateral and vertical components of the state vector are updated from the accelerometer measurements. The measurements are compensated for centripetal, lateral and vertical accelerations. In the second step a measurement for the longitudinal gravity component is formed by using the updated lateral and vertical components of the state vector.

4.2. Sensor Model

Three sensors are used in this observer. From an IMU sensor the accelerometer and gyroscope measurements are obtained. The vehicle's velocity should also be known. The measurements from the sensors at time step k can be expressed in the vehicle coordinate system as:

$$\mathbf{y}_{G_k} = \boldsymbol{\omega}_k + \mathbf{n}_G \quad (4.1)$$

$$\mathbf{y}_{A_k} = \mathbf{g}_k + \mathbf{a}_k + \mathbf{n}_A \quad (4.2)$$

$$y_{v_x} = v_x + n_v \quad (4.3)$$

where \mathbf{y}_{G_k} is a vector $[G_{x_k} \ G_{y_k} \ G_{z_k}]^T$ containing the actual gyroscope measurements about the x, y and z-axis of the vehicle coordinate frame. The actual measurements are the sum of the true angular rates $\boldsymbol{\omega}_k = [\omega_{x_k} \ \omega_{y_k} \ \omega_{z_k}]^T$ about each axis and the zero mean white Gaussian noise in each axis contained in

the vector \mathbf{n}_G . In equation (4.2) \mathbf{y}_{A_k} is a vector $[A_{x_k} \ A_{y_k} \ A_{z_k}]^T$ which contains the actual accelerometer measurements. The actual accelerometer measurements are the sum of the gravitation acceleration $\mathbf{g}_k = [g_{x_k} \ g_{y_k} \ g_{z_k}]^T$, the external accelerations $\mathbf{a}_k = [a_{x_k} \ a_{y_k} \ a_{z_k}]^T$ and the white Gaussian noise \mathbf{n}_A . In equation (4.3) y_{v_x} is the speed reading of the vehicle, v_x the actual vehicle speed and n_v is the measurement noise.

4.3. State Vector

During normal driving situations the roll and pitch angle is only a few degrees. Even in extreme situations the roll and pitch angle never becomes 90° and singularity does not occur. Using Euler angles [43] and the same definition as in Section 2.1 the state vector can be formulated. The relation between the global and the body fixed coordinate system can be given as

$$XYZ = \mathbf{R}_{rot}xyz \quad (4.4)$$

where \mathbf{R}_{rot} is the rotation matrix to rotate any vector in the body fixed coordinate system (xyz) into the global coordinate system (XYZ). The rotation matrix is given by [43]

$$\mathbf{R}_{rot} = \begin{bmatrix} \cos(\psi)\cos(\theta) & \cos(\psi)\sin(\theta)\sin(\phi) - \sin(\psi)\cos(\phi) & \cos(\psi)\sin(\theta)\cos(\phi) + \sin(\psi)\sin(\phi) \\ \sin(\psi)\cos(\theta) & \sin(\psi)\sin(\theta)\sin(\phi) + \cos(\psi)\cos(\phi) & \sin(\psi)\sin(\theta)\cos(\phi) - \cos(\psi)\sin(\phi) \\ -\sin(\theta) & \cos(\theta)\sin(\phi) & \cos(\theta)\cos(\phi) \end{bmatrix} \quad (4.5)$$

Since the last row doesn't contain any terms with the yaw angle ψ , the last row is used to calculate the roll and pitch angles, ϕ and θ respectively.

$$\phi = \text{atan}\left(\frac{R_{32}}{R_{33}}\right)$$

$$\theta = \text{atan}\left(\frac{-R_{31}}{R_{32}/\sin(\phi)}\right)$$

where R_{ij} denotes the $(i, j)^{th}$ element of \mathbf{R}_{rot} . The state vector at time step k is then defined as

$$\mathbf{x}_k = [R_{31} \ R_{32} \ R_{33}]^T \quad (4.6)$$

In [7] it is noted that the gravitational acceleration vector \mathbf{g}_k in equation (4.2) at any time step k as measured in the vehicle coordinate system is equal to

$$\mathbf{g}_k = g\mathbf{x}_k \quad (4.7)$$

where g is the gravitational acceleration constant equal to 9.81 m s^{-2}

4.4. Process Model

The process model is developed using the general equations for the process model [27], which is given by

$$\mathbf{x}_k = \mathbf{\Phi}_{k-1}\mathbf{x}_{k-1} + \mathbf{w}_{k-1} \quad (4.8)$$

where $\mathbf{\Phi}_{k-1}$ is the state transition matrix and \mathbf{w}_{k-1} is the process noise with covariance matrix \mathbf{Q}_{k-1} . The state vector \mathbf{x}_k is determined from \mathbf{x}_{k-1} using the fact that the rotation matrix $\mathbf{R}_{rot,k}$ at time step k can be computed from $\mathbf{R}_{rot,k-1}$ using the integral of the vector differential equation, which is taken from [44]:

$$\mathbf{R}_{rot,k} = \mathbf{R}_{rot,k-1}(\mathbf{I}_3 + \Delta t\tilde{\boldsymbol{\omega}}_{k-1}) \quad (4.9)$$

where t_s is the sampling time interval, $\boldsymbol{\omega}_{k-1}$ contains the ideal angular rates of rotation of the body and \sim is a cross product operator on a 3×1 vector. Taking for example the cross product operator on \mathbf{p} gives

$$\tilde{\mathbf{p}} = \begin{bmatrix} 0 & p_3 & p_2 \\ p_3 & 0 & -p_1 \\ -p_2 & p_1 & 0 \end{bmatrix} \quad (4.10)$$

Since only the last row of $\mathbf{R}_{rot,k}$ is used, instead of using equation (4.9), the following equation is used

$$\mathbf{x}_k = (\mathbf{I}_3 + t_s \tilde{\boldsymbol{\omega}}_{k-1}) \mathbf{x}_{k-1} \quad (4.11)$$

Because the ideal angular rates $\boldsymbol{\omega}_{k-1}$ are not known in practice and are measured by the gyroscope, substitution of equation (4.1) into (4.11) after some rewriting gives

$$\mathbf{x}_k = (\mathbf{I}_3 + t_s \tilde{\mathbf{y}}_{G_{k-1}}) \mathbf{x}_{k-1} + t_s \tilde{\mathbf{x}}_{k-1} \mathbf{n}_G \quad (4.12)$$

Comparison of (4.12) with (4.8) gives the state transition matrix and a model for the process noise

$$\Phi_{k-1} = \mathbf{I}_3 + t_s \tilde{\mathbf{y}}_{G_{k-1}} \quad (4.13)$$

$$\mathbf{w}_{k-1} = t_s \tilde{\mathbf{x}}_{k-1} \mathbf{n}_G \quad (4.14)$$

In [7] it was stated that the state dependence of the process noise \mathbf{w}_{k-1} does not violate any underlying assumption of the Kalman filter. The process noise covariance \mathbf{Q}_{k-1} is given by

$$\mathbf{Q}_{k-1} = E[\mathbf{w}_{k-1} \mathbf{w}_{k-1}^T] \quad (4.15)$$

Substitution of equation (4.14) into (4.15) and using $\tilde{\mathbf{x}}_{k-1}^T = -\tilde{\mathbf{x}}_{k-1}$ gives

$$\mathbf{Q}_{k-1} = -t_s^2 \tilde{\mathbf{x}}_{k-1} \sum_G \tilde{\mathbf{x}}_{k-1} \quad (4.16)$$

Where \sum_G is the covariance matrix of the gyroscope noise given by $E[\mathbf{n}_G \mathbf{n}_G^T]$ which is set equal to $\sigma_G^2 \mathbf{I}_3$ by assuming that the variance of the gyroscope noise σ_G^2 is the same along all three axes.

4.5. Measurement Model

A measurement model is developed with the purpose to mitigate the error propagated in the state estimate by the process model. The measurement update is done in two steps. The general equations of the measurement models [27] are given by

$$\mathbf{z}_{k,1} = \mathbf{H}_1 \mathbf{x}_k + \mathbf{Y}_{k,1} \quad (4.17)$$

$$\mathbf{z}_{k,2} = \mathbf{H}_2 \mathbf{x}_k + \mathbf{Y}_{k,2} \quad (4.18)$$

where $\mathbf{z}_{k,1}$ and $\mathbf{z}_{k,2}$ are measurement vectors, \mathbf{H}_1 and \mathbf{H}_2 are observation matrices and $\mathbf{Y}_{k,1}$ and $\mathbf{Y}_{k,2}$ are the measurement noise with covariance matrices $\mathbf{M}_{k,1}$ and $\mathbf{M}_{k,2}$ for updates 1 and 2 respectively.

The accelerometer measurements \mathbf{y}_{A_k} for the measurements updates as defined in equation (4.2) are used. \mathbf{y}_{A_k} consists of the sum of the gravitational \mathbf{g}_k and external acceleration \mathbf{a}_k components. Since \mathbf{a}_k is not zero when the vehicle is moving, it needs to be subtracted from \mathbf{y}_{A_k} before using it for the measurement update. The external accelerations are determined by resolving them into their constituent components using the kinematic model of a car. The definition of the axis as defined in [7] is slightly different as the definition taken in Section 2.1. Since the final estimated roll and pitch angle only have a sign difference, in this section the definition as in [7] is taken, which can be seen in Figure 4.1.

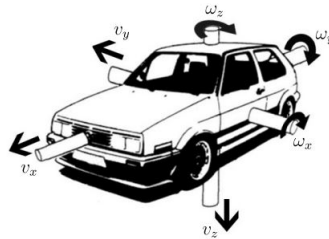


Figure 4.1: Direction of linear and angular velocities as used in [7], taken from [7]

Using the directions of the velocities and angular rates as in Figure 4.1 the external accelerations are given by [7]

$$\mathbf{a}_{x_k} = \dot{v}_{x_k} - \omega_{z_k} v_{y_k} + \omega_{x_k} v_{z_k} \quad (4.19)$$

$$\mathbf{a}_{y_k} = \dot{v}_{y_k} + \omega_{z_k} v_{x_k} - \omega_{y_k} v_{z_k} \quad (4.20)$$

$$\mathbf{a}_{z_k} = \dot{v}_{z_k} - \omega_{x_k} v_{x_k} + \omega_{y_k} v_{z_k} \quad (4.21)$$

In equation (4.19), \dot{v}_{x_k} cannot be estimated using the available sensor data and is too significant to ignore. Although generally v_x is given by the Controller Area Network (CAN) bus, which can be used for the longitudinal velocity v_{x_k} , it cannot be differentiated to obtain \dot{v}_{x_k} . The speed given by the CAN bus is a very low rate approximation of the actual speed. Differentiation will give an incorrect estimate of \dot{v}_{x_k} . In [7], the x-axis accelerometer measurements are discarded, because \mathbf{a}_{x_k} cannot be determined. \mathbf{a}_{y_k} and \mathbf{a}_{z_k} can be determined from equation (4.20) and (4.21) and are subtracted from the y and z-axis accelerometer readings to give the measurement vector $\mathbf{z}_{k,1}$, which updates the state vector \mathbf{x}_k in the first measurement update.

It can be noted that the most significant quantities in equation (4.20) and (4.21) are the longitudinal velocity v_{x_k} and the yaw rate ω_{z_k} . Ideally the velocities v_{y_k} and v_{z_k} are zero, but when the tires are being steered, a small lateral velocity component v_{y_k} is present due to the tire cornering stiffness. The same holds for the vertical velocity v_{z_k} when the car hits a bump on the road. In [7] the derivatives of the lateral and vertical velocity, so \dot{v}_{y_k} and \dot{v}_{z_k} , are modelled using a first order low pass process:

$$\alpha_k = c_\alpha \alpha_{k-1} + \epsilon_k \quad (4.22)$$

where α_k is an external acceleration component at time step k , c_α is a dimensionless constant which determines the cut-off frequency and ϵ_k is the error in this model. Modelling \dot{v}_{y_k} and \dot{v}_{z_k} by α_{y_k} and α_{z_k} according to equation (4.22) gives

$$\alpha_{y_k} = c_{a1} \alpha_{y_{k-1}} + \epsilon_{y_k} \quad (4.23)$$

$$\alpha_{z_k} = c_{a2} \alpha_{z_{k-1}} + \epsilon_{z_k} \quad (4.24)$$

For simplicity $c_{a1} = c_{a2} = c_a$. Substitution in equation (4.20) and (4.21) and ignoring the negligible products $\omega_{y_k} v_{z_k}$ and $\omega_{y_k} v_{y_k}$ gives

$$\alpha_{y_k} = c_a \alpha_{y_{k-1}} + \omega_{z_k} v_{x_k} + \epsilon_{y_k} \quad (4.25)$$

$$\alpha_{z_k} = c_a \alpha_{z_{k-1}} - \omega_{x_k} v_{x_k} + \epsilon_{z_k} \quad (4.26)$$

4.5.1. Measurement Update 1

Substitution of the gyroscope and CAN bus measurements from equation (4.1) and (4.3) into equation (4.25) and (4.26) gives

$$\mathbf{a}_{y_k} = c_a \alpha_{y_{k-1}} + (G_{z_k} - n_{G_z})(y_{v_x} - n_v) + \epsilon_{y_k} \quad (4.27)$$

$$\mathbf{a}_{z_k} = c_a \alpha_{z_{k-1}} - (G_{x_k} - n_{G_x})(y_{v_x} - n_v) + \epsilon_{z_k} \quad (4.28)$$

This can be arranged in matrix form as

$$\mathbf{a}_{k,1} = c_a \boldsymbol{\alpha}_{k-1} + \mathbf{y}_{G_{k,1}} v_t + \mathbf{n}_{G,1} \mathbf{n}_{v,1} + \boldsymbol{\epsilon}_k \quad (4.29)$$

where $\mathbf{a}_{k,1} = [a_{y_k} \ a_{z_k}]^T$, $\boldsymbol{\alpha}_{k-1} = [\alpha_{y_{k-1}} \ \alpha_{z_{k-1}}]^T$, $\mathbf{y}_{G_{k,1}} = [G_{z_k} \ -G_{x_k}]^T$, $\mathbf{n}_{G,1} = [n_{G_z} \ n_{G_x}]^T$, $\mathbf{n}_{v,1} = [n_v \ n_v]^T$ and $\boldsymbol{\epsilon}_k = [\epsilon_{y_k} \ \epsilon_{z_k}]^T$.

The cross-product terms are ignored for simplicity, because their contribution to the measurement noise will be negligible. In the first update the x-axis accelerometer readings are discarded and the update from y- and z-axis readings are applied, so the accelerometer measurement for this update can be arranged in the vector form as

$$\mathbf{y}_{A_{k,1}} = [A_{y_k} \ A_{z_k}]^T \quad (4.30)$$

Combining equations (4.29), (4.30) and (4.2) gives

$$\mathbf{y}_{A_{k,1}} = H_m \mathbf{g} \mathbf{x}_k + c_a \boldsymbol{\alpha}_{k-1} + \mathbf{y}_{G_{k,1}} v_x + \mathbf{n}_{G,1} \mathbf{n}_{v,1} + \boldsymbol{\epsilon}_k + \mathbf{n}_{A,1} \quad (4.31)$$

Equation (4.31) is then compared with the measurement model in equation (4.17) which gives

$$\mathbf{z}_{k,1} = \mathbf{y}_{A_{k,1}} - c_a \boldsymbol{\alpha}_{k-1} - \mathbf{y}_{G_{k,1}} v_x \quad (4.32)$$

$$\mathbf{H}_1 = g H_m = g \begin{bmatrix} 0 & 1 & 0 \\ 0 & 0 & 1 \end{bmatrix} \quad (4.33)$$

$$\mathbf{Y}_{k,1} = \boldsymbol{\epsilon}_k + \mathbf{n}_{G,1} \mathbf{n}_{v,1} + \mathbf{n}_{A,1} \quad (4.34)$$

The measurement noise covariance $\mathbf{M}_{k,1}$ is given as

$$\mathbf{M}_{k,1} = E[\mathbf{Y}_{k,1} \mathbf{Y}_{k,1}^T] \quad (4.35)$$

It is assumed that $\boldsymbol{\epsilon}_k$, $\mathbf{n}_{G,1}$, $\mathbf{n}_{v,1}$ and $\mathbf{n}_{A,1}$ are uncorrelated, so that $\mathbf{M}_{k,1}$ can be written as

$$\mathbf{M}_{k,1} = \sum a_k + \sum_{GV} + \sum_A \quad (4.36)$$

Here \sum_{GV} is the measurement noise from the velocity and gyroscope product terms which is set equal to $\sigma_v^2 \sigma_g^2 \mathbf{I}_2$. \sum_A is the accelerometer noise which is set equal to $\sigma_A^2 \mathbf{I}_2$. It is assumed that the accelerometer variance is the same along both y and z-axis. $\sum a_k$ is the contribution to the measurement noise by the model based estimation of $\boldsymbol{\alpha}_k$ which is given by $E[\boldsymbol{\epsilon}_k \boldsymbol{\epsilon}_k^T]$. $E[\boldsymbol{\epsilon}_k \boldsymbol{\epsilon}_k^T]$ cannot be determined analytically and in [7] an approximation is used: $\sum a_k = 2^{-1} c_a^2 \|\boldsymbol{\alpha}_{k-1}\|^2 \mathbf{I}_2$ which was suggested in [45].

4.5.2. Measurement Update 2

The lateral and vertical axes accelerometer readings are used to obtain the correct estimates of second and third element of the state vector \mathbf{x}_k , so $\mathbf{x}_k(2)$ and $\mathbf{x}_k(3)$, respectively in equation (4.6). It can be noted that the state vector in equation (4.5), due to the definition of a rotation matrix, has the property:

$$\sqrt{\mathbf{x}_k(1)^2 + \mathbf{x}_k(2)^2 + \mathbf{x}_k(3)^2} = 1$$

Assuming that the correct estimates of $\mathbf{x}_k(2)$ and $\mathbf{x}_k(3)$ are obtained, the property above is used to calculate the estimate of $\mathbf{x}_k(1)$:

$$\mathbf{x}_k(1) = \sqrt{1 - \mathbf{x}_k(2)^2 - \mathbf{x}_k(3)^2}$$

The estimate of $\mathbf{x}_k(1)$ is then used as a measurement for correcting the state vector in the next step. The measurement is denoted by y_{x_k}

$$\begin{aligned} y_{x_k} &= \sqrt{1 - \mathbf{x}_k(2)^2 - \mathbf{x}_k(3)^2} + \delta_k \\ &= \mathbf{x}_k(1) + \delta_k \end{aligned} \quad (4.37)$$

where δ_k is the noise in this measurement. Comparison equation (4.37) with (4.18) gives

$$\mathbf{z}_{k,2} = y_{x_k} \quad (4.38)$$

$$\mathbf{H}_2 = [1 \quad 0 \quad 0] \quad (4.39)$$

$$\mathbf{Y}_{k,2} = \delta_k \quad (4.40)$$

The measurement noise covariance $\mathbf{M}_{k,2}$ is given by $E[\delta_k \delta_k^T]$ and can be seen as a tuning parameter.

4.6. Filter Procedure

The proposed Kalman filter algorithm proposed in [7] is summarised in Figure 4.2. The $-$ superscript denotes the *a priori* estimate, the $+$ superscript denotes the *a posteriori* estimate after the first measurement update and $++$ denotes the *a posteriori* estimate after the second measurement update. P_k is the error covariance matrix and $K_{k,1}$ and $K_{k,2}$ are the Kalman gains for the first and second measurements updates respectively at time step k .

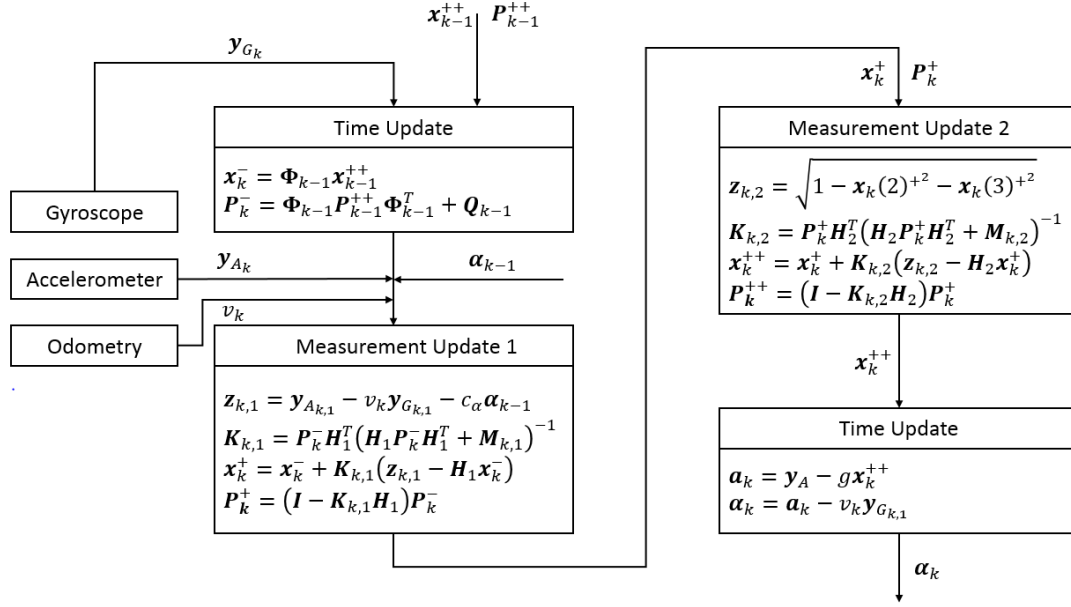


Figure 4.2: Kalman filter structure

The roll and pitch angles are calculated from the *a posteriori* state estimate:

$$\phi_k = \text{atan}\left(\frac{x_k^{++}(1)}{x_k^{++}(2)}\right) \quad (4.41)$$

$$\theta_k = \text{atan}\left(\frac{-x_k^{++}(1)}{x_k^{++}(2)/\sin(\phi_k)}\right) \quad (4.42)$$

5

Simulation Setup

In this chapter the simulation setup is presented. First the the simulation environments are discussed. Then the different test manoeuvres are presented which are used to test the performance of the observers. Lastly the criteria that the observers have to satisfy are discussed.

5.1. Simulation Environments

Below two different types of simulation environments are discussed. In the first environment a nonlinear vehicle model in Simulink is used. In the second simulation environment IPG CarMaker is used.

5.1.1. Nonlinear Vehicle Model

In the first simulation environment a nonlinear vehicle model is used to test the observers. The vehicle model is a SimMechanics model in Simulink. The vehicle model not only takes the planar dynamics into account, but also the roll, pitch and yaw dynamics. The downside of this model is that it only takes limited vertical dynamics into account. Due to this reason this model is not used for extensive test procedures, but only used for preliminary evaluation, during the development of the observers. In the model the tyres are modelled by making use of the Magic formula [39]. With the Magic formula the tyre forces can be accurately calculated.

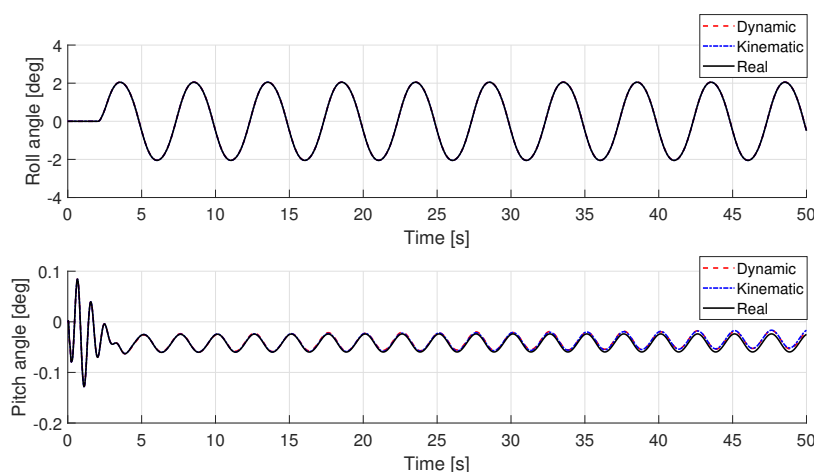


Figure 5.1: Comparison of the roll and pitch angle

The nonlinear model is used to test the performance of the observers when a sinusoidal steering input is applied to the vehicle model. This is a so called sine wave. The goal of this test is to see if the observers will suffer from drift after a certain time interval. The frequency of the steering will be set to 0.2 Hz. The steering wheel angle will be varying between -30° and 30° . The manoeuvre is executed at a speed of 80 km h^{-1} .

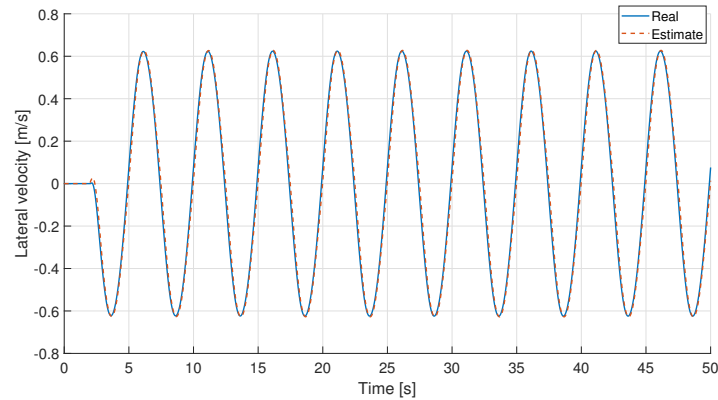


Figure 5.2: Comparison of the lateral velocity

In Figure 5.1 and 5.2 the performance of the observers can be seen for the sinusoidal steering input. It can be observed that the estimates of the roll, pitch and lateral velocity match up well with the true values out of the nonlinear model. When the true roll angle is equal to 2° , the roll estimates of the dynamic and kinematic observer are also equal to 2° . There is only a very small difference between the true pitch angle and the estimate of the pitch angle of the kinematic observer at the end of the manoeuvre. To test the performance of the observers in more extreme situations, many different tests are done with IPG CarMaker described in the next section.

5.1.2. IPG CarMaker

To test the performance of the observers in extreme situations, tests are done in IPG CarMaker. This software is a highly advanced simulation environment. IPG CarMaker consists of a highly nonlinear vehicle model, which makes the model behave very similar to a real vehicle. The benefits of this vehicle model above the nonlinear model in the previous section apart from the vertical dynamics, is that IPG CarMaker takes into account the compliance of the suspension components and also the kinematics of the suspension are defined in greater detail.

The vehicle model that is used in IPG CarMaker resembles a compact hatchback. This vehicle model was provided by a car manufacturer and the model was validated using a real vehicle. The vehicle model showed similar behaviour as a real vehicle. The model contained detailed information about the mass distribution and geometry of the vehicle. Also the nonlinear spring and damper characteristics as well as the tyre property files were specified.

The accelerations that IPG CarMaker outputs do not contain the gravitational accelerations, only the accelerations caused by the vehicle are given. Since the kinematic observer needs the gravitational acceleration to work properly, it is added to the input of the observers. The gravitational acceleration always points straight down and can be decomposed in the longitudinal, lateral and vertical axis of the vehicle using the true roll and pitch angle from IPG CarMaker. Using Figure 2.1b in Chapter 2 where the body fixed axis of the vehicle is defined, the gravitational acceleration can be decomposed as

$$g_{x_k} = g \sin(\theta_k) \quad (5.1)$$

$$g_{y_k} = -g \sin(\phi_k) \cos(\theta_k) \quad (5.2)$$

$$g_{z_k} = -g \cos(\phi_k) \cos(\theta_k) \quad (5.3)$$

Where k is the time step and g the gravitational constant equal to 9.81 ms^{-2}

5.2. Test Manoeuvres

The following test manoeuvres are done using IPG CarMaker: a sine sweep, step response, double lane change manoeuvre, skidpad, fishhook, braking manoeuvres and driving on a racetrack. Each will be discussed in detail below.

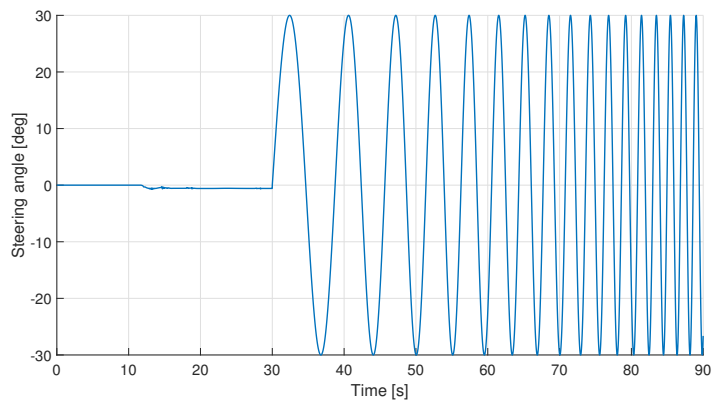


Figure 5.3: Steering angle profile of the sine sweep manoeuvre

5.2.1. Sine Sweep

A sine sweep manoeuvre is very similar to sine wave manoeuvre, only the frequency of the steering angle is not held constant, but instead increases over time. The starting frequency is chosen to be equal to 0.1 Hz and the final frequency is equal to 1 Hz. The vehicle starts from standstill and then accelerates to 80 km h^{-1} . Then the vehicle starts doing the manoeuvre for 60 seconds. The steering input is similar to the sine wave and still varies between -30° and 30° . The visualisation of the steering input in this manoeuvre can be seen in Figure 5.3.

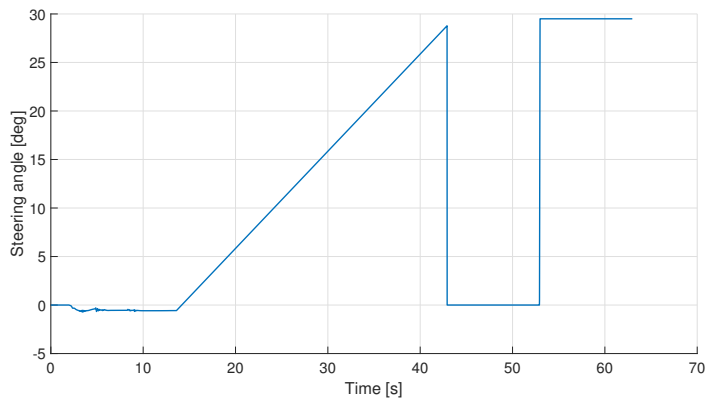


Figure 5.4: Steering angle profile of the step response manoeuvre. Steering angle is slowly increased till the lateral acceleration reaches 4 ms^{-2} , then two step steering inputs are applied

5.2.2. Step Response

The next manoeuvre is a step response steering input. The goal of a step response manoeuvre is to see how well the observers can track the true roll and pitch angle when there is a sudden change of direction. The vehicle starts the manoeuvre again from standstill and accelerates to 80 km h^{-1} . Then the steering angle is slowly increased till the lateral acceleration reaches 4 ms^{-2} . This is done to find right the steering angle needed in the step response. After a few seconds of straight line driving, the step steering input is applied which can be seen in Figure 5.4. The steering rate is limited to 500 deg/s . The steering rate is limited to this value, because in real driving conditions a driver is not able to turn at a faster rate.

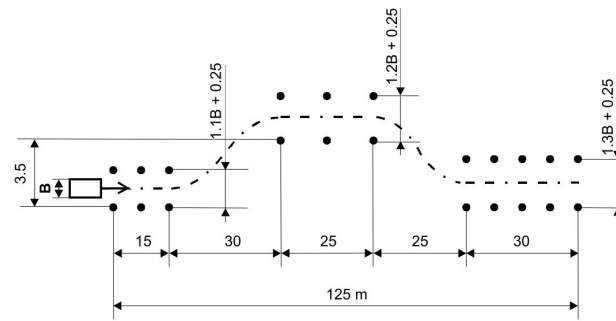


Figure 5.5: Trajectory of a double lane change, where B is the the car width, taken from [46]

5.2.3. Double Lane Change

In Figure 5.5 the trajectory of a double lane change manoeuvre can be seen, where the dotted line is the desired path of the car. The goal of this test is to see the performance of the estimators during extreme conditions, where large roll is expected. The initial velocity at the entrance of the manoeuvre is set to 90 km h^{-1} . After finishing the manoeuvre the vehicle returns to steady state in which the estimated roll and pitch angle should go back to zero.

5.2.4. Skidpad

A skidpad is a circular area with a fixed radius and flat pavement. The radius of the circle is 42 meters. The vehicle drives from standstill in circles until the point that lateral deviation of the vehicle deviates more than half a meter of the desired course, then the vehicle slows back down to standstill. The velocity at which the vehicle cannot follow the desired course is 70 km h^{-1} . The goal of this test is not to find the maximum lateral acceleration of the vehicle, but to see how well the observers can cope with roll and pitch behaviour for a long duration. The objective of this test manoeuvre is to have a minimum drift error.

5.2.5. Fishhook

To test the performance of the observers during a critical vehicle manoeuvre, where the vehicle can roll over, a fishhook test is performed. In this test the vehicle will be likely to roll over and the goal of this test is to see how well the observers perform when extreme roll is present. The steering input of the manoeuvre can be seen in Figure 5.6.

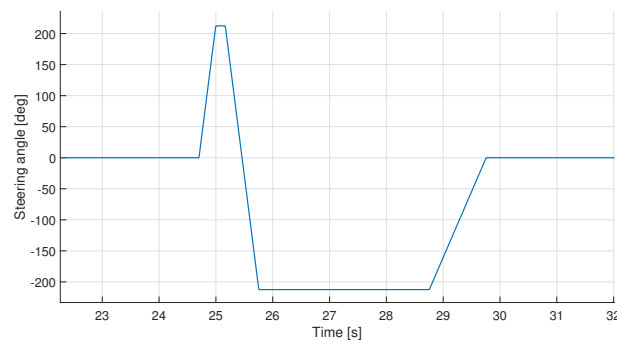


Figure 5.6: Steering input of the fishhook manoeuvre

5.2.6. Braking Straight Line

To test the correctness of the pitch angle estimate of the observers some braking tests are done. This is done driving in a straight line at constant speed of 75 km h^{-1} and then the braking is initiated. Two braking test are being done. First normal braking is simulated by applying half of the braking force. The vehicle then gradually slows down to a standstill. In the second test the vehicle is tested at its limit and maximum braking force is applied. This is done to check the performance of the observers during an extreme driving situation.

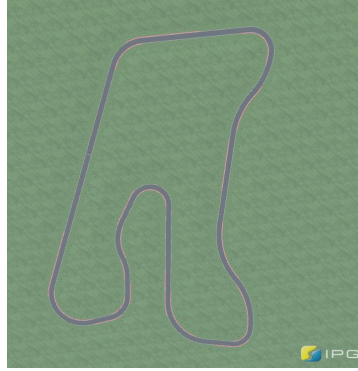


Figure 5.7: Layout of Hockenheim racetrack

5.2.7. Hockenheim Racetrack

To test the performance of the observers over a long time duration, the vehicle is driven on a racetrack. The Hockenheim race track can be seen in Figure 5.7. In IPG CarMaker a predefined driver can be selected, which follows the track in the most efficient way. The driver was limited to drive between a set of accelerations. The longitudinal acceleration could not exceed 3.0 ms^{-2} , the longitudinal deceleration could not exceed -4.0 ms^{-2} and the lateral acceleration could not exceed 4.0 ms^{-2} . Driving on this track contains braking and acceleration as well as braking during cornering, so all kinds of vehicle motions are present to test the performance of the observers.

5.3. Variances and Noise Generation

The variances of the IMU sensor and velocity sensor were chosen such that they represent low quality sensors as in Table 2.1. In Table 5.1 the values of the variances that are used for the IMU sensor and velocity sensor can be seen. To simulate noisy sensor data from low quality IMU sensors, noise was added to the angular rates, accelerometers and velocity sensor, which are the inputs of the observers. In Simulink the band-limited white noise block was used to simulate this noise. The input of the block was noise power. In Table 5.1 the values of the noise powers that are used in simulation can be seen.

Table 5.1: Variances and noise powers used in the simulation

Sensor component	Variance	Noise power
Gyroscope	$1.60 \times 10^{-3} \text{ rad s}^{-1}$	$1.57 \times 10^{-4} \text{ rad s}^{-1}$
Accelerometer	$1.96 \times 10^{-2} \text{ m s}^{-2}$	$1.50 \times 10^{-3} \text{ m s}^{-2}$
Velocity	$1.00 \times 10^{-4} \text{ m s}^{-1}$	$1.00 \times 10^{-5} \text{ m s}^{-2}$

5.4. Initialisation of the Observers

In this section the initialisation of the observers is presented. For both observers the variances of the IMU sensor and velocity sensor are the same and can be seen in Table 5.1.

5.4.1. Kinematic Observer

The Kinematic observer has two tuning parameters which need to be set. The first one is c_a , which determines the cut-off frequency of the first order low pass process in equation (4.22). It can vary between 0 and 1. The second tuning parameter is the measurement noise covariance $M_{t,2}$ in the second measurement update. After trial and error, c_a is set equal to 1 and $M_{t,2}$ is set equal to 0.9.

The Kalman filter inside the kinematic observer requires also the initialisation of the state vector and the covariance matrix. The state vector was initialised by using the initial orientation of the vehicle. The covariance matrix was initialised by setting the whole matrix equal to machine precision, which is equal to 10^{-16} .

5.4.2. Dynamic Observer

The initialisation of the dynamic observer is a bit more complicated. First the parameters of the internal vehicle model have to be known, which were discussed in Section 3.2.3. Then the tuning parameters of the internal vehicle model have to be set. Lastly the initialisation of the EKF needs to be performed. The vehicle parameters of the compact hatchback, which are used to test the performance of the observers, can be seen in Table 5.2.

Table 5.2: Vehicle parameters of a compact hatchback

Parameter	Value	Unit
m	1500	kg
m_s	1300	kg
I_{xx}	500	kgm ²
I_{yy}	2000	kgm ²
I_{zz}	2000	kgm ²
L	2.5	m
l_f	1.0	m
h_{cg}	0.6	m
h_f	0.8	m
h_{roll}	0.1	m
h_{pitch}	0.4	m
$K_{z,f}$	25000	Nm ⁻¹
$K_{z,r}$	30000	Nm ⁻¹
$D_{z,f}$	1300	Nsm ⁻¹
$D_{z,r}$	1500	Nsm ⁻¹

Now that the vehicle parameters are set, the linear tyre slip stiffnesses $K_{y,F}$ and $K_{y,R}$ are tuned. They are both set equal to 20. The front roll stiffness is tuned to a value of 80000 Nrad⁻¹ and in the rear to 40000 Nrad⁻¹. The pitch stiffness is tuned to a value of 30000 Nrad⁻¹. The front roll damping is tuned to 11000 Nsm⁻¹ and in the rear to 1500 Nsm⁻¹. The pitch damping coefficient is tuned to 10000 Nsm⁻¹.

The EKF inside the dynamic observer needs also to be initialised and tuned. The tuning parameters are the process noise covariance matrix \mathbf{Q} and the measurement noise covariance matrix \mathbf{R} . \mathbf{R} is set by using the variances of Table 5.1, which gives the following matrix:

$$\mathbf{R} = \begin{bmatrix} \sigma_A^2 & 0 & 0 & 0 \\ 0 & \sigma_G^2 & 0 & 0 \\ 0 & 0 & \sigma_G^2 & 0 \\ 0 & 0 & 0 & \sigma_G^2 \end{bmatrix}$$

The process noise covariance matrix \mathbf{Q} is different for when no noise is added and when noise is added to the inputs of the observers. When no noise is added to the inputs of the observer the values on the diagonal of the \mathbf{Q} matrix are chosen to be equal to 10^{-3} . Changing the values on the diagonal does not have a significant effect on the estimation performance of the roll and pitch angle. The dynamics of the roll and pitch angle in the internal vehicle model do not match up completely with the actual roll and pitch dynamics, to compensate this some noise is added to the off diagonal values that relate the roll and pitch angle to the roll and pitch rates. This off diagonal noise is set equal to 10^{-3} .

When noise is added to the inputs of the observer this off diagonal noise has a negative influence on the estimation performance and so is removed when noise is added to the inputs. It turned out that the values on the diagonal equal to 10^{-3} of the \mathbf{Q} matrix when no noise was added to the inputs were also a good approximation when noise was added to the inputs. Increasing the noise on the diagonal resulted in a larger drift error of the roll and pitch angle, while decreasing the noise on the diagonal lead to under estimation of the roll and pitch angle.

When no noise is added to the inputs the Q matrix is equal to

$$Q = \begin{bmatrix} 10^{-3} & 0 & 0 & 0 & 0 & 0 \\ 0 & 10^{-3} & 0 & 0 & 0 & 0 \\ 0 & 0 & 0 & 10^{-3} & 0 & 0 \\ 0 & 0 & 0 & 10^{-3} & 0 & 0 \\ 0 & 0 & 0 & 0 & 0 & 10^{-3} \\ 0 & 0 & 0 & 0 & 0 & 10^{-3} \end{bmatrix}$$

When noise is added to the inputs the Q matrix is equal to

$$Q = \begin{bmatrix} 10^{-3} & 0 & 0 & 0 & 0 & 0 \\ 0 & 10^{-3} & 0 & 0 & 0 & 0 \\ 0 & 0 & 0 & 0 & 0 & 0 \\ 0 & 0 & 0 & 10^{-3} & 0 & 0 \\ 0 & 0 & 0 & 0 & 0 & 0 \\ 0 & 0 & 0 & 0 & 0 & 10^{-3} \end{bmatrix}$$

The state vector of the EKF was initialised by setting the whole vector equal to machine precision, which is the same value as used in the initialisation of the kinematic observer. When no noise was added to the inputs of the observer the covariance matrix was initialised as an identity matrix and with noise added to the inputs, it was initialised as a diagonal matrix with the first 2 inputs of the diagonal equal to 1 and the other inputs equal to 10^{-4} . The roll and pitch angle always had a small offset, due to the weight of the driver. To compensate for this offset, it was added to the final state estimate in the EKF.

5.5. Passing Criteria

In this section the criteria that the observers have to meet are discussed.

5.5.1. Mean Error

A good indicator of estimation performance, which is also used in literature [7, 45], is the so called Root Mean Square (RMS) error. It represents the square root of the mean square error. It can be defined as

$$\text{RMS} = \sqrt{E((\hat{x} - x)^2)} \quad (5.4)$$

where \hat{x} is the estimate and x is the estimated or true value. The RMS error can never be negative and ideally it is equal to 0, which means perfect estimation, but this is never achieved in practice.

For the roll and pitch angle the the desired performance threshold of the RMS error of the roll and pitch angle is set to the same value as in [7], which is equal to 1°. This applies for both the kinematic and dynamic observer.

5.5.2. Maximum error

Although the RMS error is sensitive to outliers it could happen that in certain situations large estimation errors are present for a short duration. This roll and pitch error peaks could have a negative influence on sensors that make use of the estimated roll and pitch angle. To detect that these error peaks are not too large, a limit is set. In this thesis the maximum error limit of the roll and pitch angle is set to 2°.

6

Simulation Results

In this chapter the results of the different manoeuvres are presented. First the roll and pitch estimation results are presented. There is a distinction made between no noise added to the inputs of the observers and noise added to the inputs. Lastly the estimation results of the lateral velocity of the dynamic observer are presented.

6.1. Roll & Pitch Angle

In this section the roll and pitch angle estimation results are presented. To see the performance of the observers during different quality of the sensors, a distinction is made. First the results are presented when perfect sensor data is assumed and no noise is added to the inputs of the observers. Then the results are presented when sensor noise is added, which resembles a worst case scenario with low quality sensors.

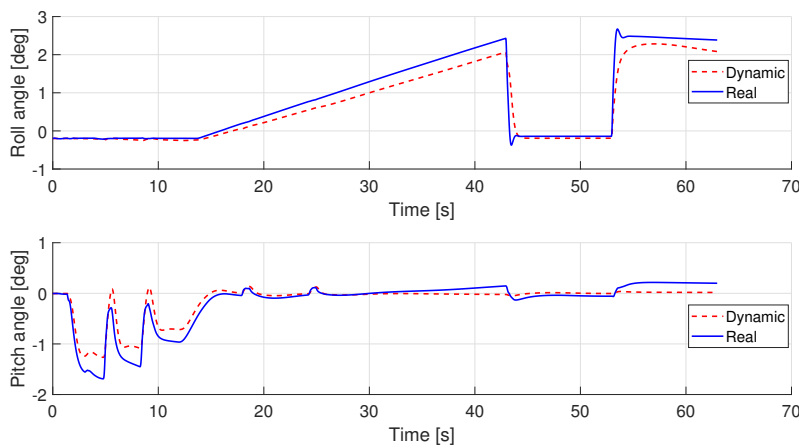


Figure 6.1: Calculated roll and pitch angle in the internal vehicle model during the step response manoeuvre

6.1.1. No Noise Added

In Figure 6.1 the calculated roll and pitch angle of the internal vehicle model in the dynamic observer can be seen during the step response manoeuvre. It can be observed that the calculated values of the roll and pitch angle already match up quite well with the actual roll and pitch angle, which means that the internal model functions properly.

In Table 6.1 the RMS errors of the roll and pitch angle of both observers can be seen. Looking at the table it can be observed that for almost all manoeuvres the RMS error stays below the threshold of 1°. Only when the vehicle is driven on the Hockenheim racetrack the threshold for the RMS error of the roll angle of the kinematic observer is exceeded and during this manoeuvre, the RMS error of the pitch angle is also the highest

Table 6.1: RMS errors of the observers for different manoeuvres, when no sensor noise is present

Manoeuvre	RMS error roll [°]		RMS error pitch [°]	
	Dynamic	Kinematic	Dynamic	Kinematic
Sine sweep	0.0454	0.1153	0.0039	0.2819
Step response	0.3340	0.3983	0.0035	0.1560
Double lane change	0.0151	0.1066	0.0051	0.0958
Skidpad	0.8053	0.5944	0.0133	0.0969
Fishhook	0.1256	0.4479	0.0600	0.5064
Normal braking straight line	0.0116	0.0201	0.0047	0.1121
Emergency braking straight line	0.0396	0.7001	0.0071	0.1180
Hockenheim racetrack	0.5866	7.0941	0.0170	0.5894

of all the manoeuvres. This can be explained by the fact that when the vehicle is driven on the Hockenheim racetrack, there are constantly large accelerations that persist for long periods of time. As already mentioned in the introduction kinematic relations cannot capture all the motions of the vehicle during large accelerations, because kinematic relations do not take into account tyre behaviour. This causes the estimate of the roll angle to drift away over time from the true estimate, which results in a large RMS error.

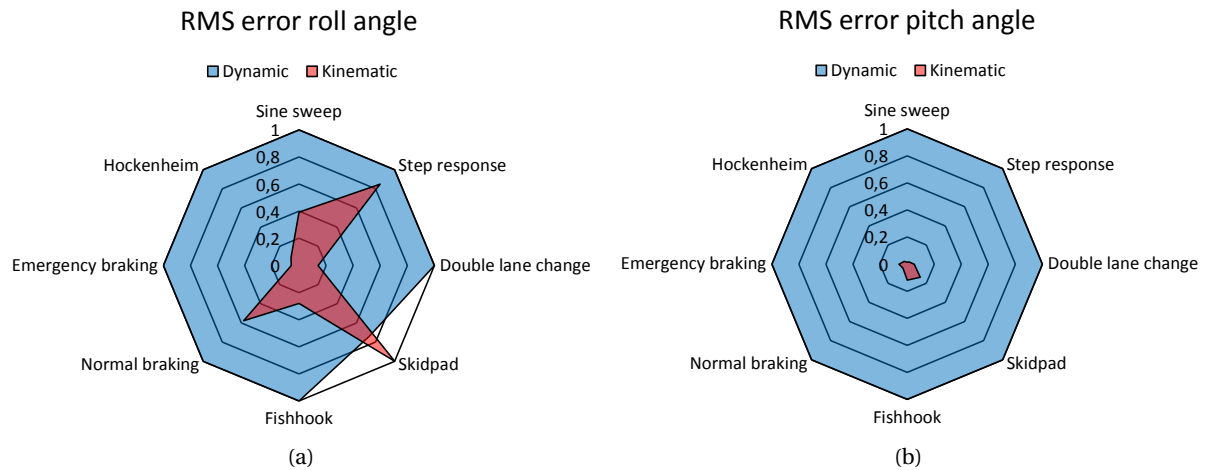


Figure 6.2: RMS error of each manoeuvre normalised to the best performing observer. Roll angle (a) and pitch angle (b)

What also can be seen from Table 6.1 is that the RMS error for the roll angle is the lowest for both observers when braking in a straight line. This is as expected because the braking is done in straight line, so no roll angle is present. The RMS errors at this manoeuvre are almost the same, because at this point the kinematic relations still can capture the motion of the vehicle. When looking at the results from the emergency braking manoeuvre, the results is a bit different. Then the RMS error of the roll angle increases for the kinematic observer. The vehicle in IPG CarMaker is not equipped with Anti-Lock Braking System (ABS) and one wheel of the vehicle locks during the manoeuvre. The kinematic observer has trouble to capture this, while the dynamic observer takes this into account.

In Figure 6.2 RMS errors of the roll and pitch angle from Table 6.1 are visualised. At every manoeuvre the RMS error is normalised to the best performing observer. This means that the best performing observer will be set equal to 1 and the other observer will be scaled accordingly. In this figure the large differences

in performance of the dynamic and kinematic observer become visible. Especially the RMS errors of the dynamic observer regarding the pitch angle are much lower than the RMS errors of the kinematic observer.

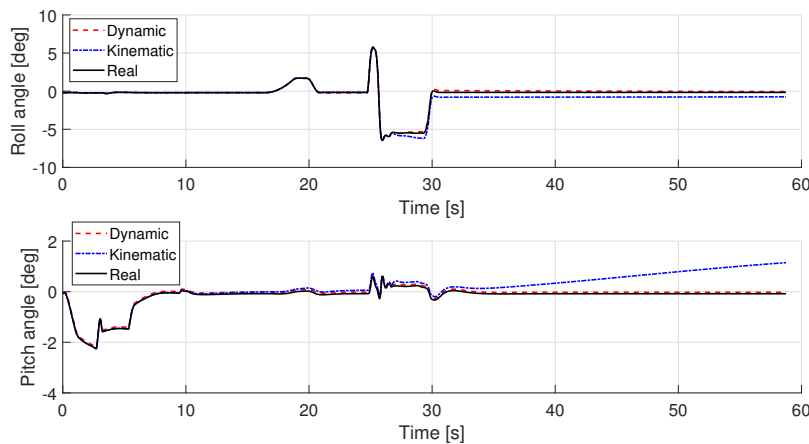


Figure 6.3: Estimation performance during the fishhook manoeuvre

The RMS error of the roll angle of the dynamic observer is the largest for the skidpad manoeuvre. It is even larger than the RMS error of the kinematic observer, which can also clearly be seen in Figure 6.2. In this manoeuvre the vehicle was driven from standstill and then constantly accelerating until the point that the lateral deviation reached a certain value. The performance of the dynamic observer can be explained by a mismatch of the dynamics at larger slip values, which is extra dominant for long periods of time. Due to the mismatch between the exponential tyre forces and the actual tyre forces at high slip values, which could be seen in Figure 3.4 of Chapter 3, the lateral acceleration that is calculated in the vehicle model is too high, but this is then over compensated by the terms that contains the roll stiffness and roll coefficients in equation (3.37), which leads to a calculated roll angle in the internal vehicle model that is too low compared to the actual roll angle.

Table 6.2: Maximum deviation of the observers for different manoeuvres, when no sensor noise is present

Manoeuvre	Maximum deviation roll [°]		Maximum deviation pitch [°]	
	Dynamic	Kinematic	Dynamic	Kinematic
Sine sweep	0.1285	0.2933	0.0344	0.8689
Step response	0.6934	1.2396	0.0348	0.2918
Double lane change	0.0668	0.4662	0.0347	0.3231
Skidpad	2.0161	1.6265	0.0404	0.4121
Fishhook	0.2540	0.7388	0.0823	1.2288
Normal braking straight line	0.0538	0.0468	0.0329	0.2474
Emergency braking straight line	0.1147	2.1168	0.0492	0.4708
Hockenheim racetrack	1.6914	13.7525	0.0398	1.1234

In Figure 6.3 the estimation performance of the fishhook manoeuvre can be seen. It can be observed that there is a slight mismatch of the estimated roll angle of the kinematic observer that starts halfway of the manoeuvre. From that point on the pitch angle slowly drifts away from the true angle. The drift of the pitch angle can be explained by the fact that the roll and pitch angle in the state vector of the kinematic observer are coupled. An incorrect estimate of the roll angle leads to an incorrect estimate of the pitch angle.

In Table 6.2 the maximum estimation deviation of the observers with respect to the real roll and pitch angle can be seen. The roll angle of the kinematic observer shows the largest deviation. This is as expected since the RMS error was also the largest. Looking at Figure 6.4 this also can be observed. Although the shape of the estimated roll and pitch angle looks similar to that of the true values, the estimates drift away from the true values, because the kinematic relations cannot capture all the motions, due to the large and prolonged accelerations.

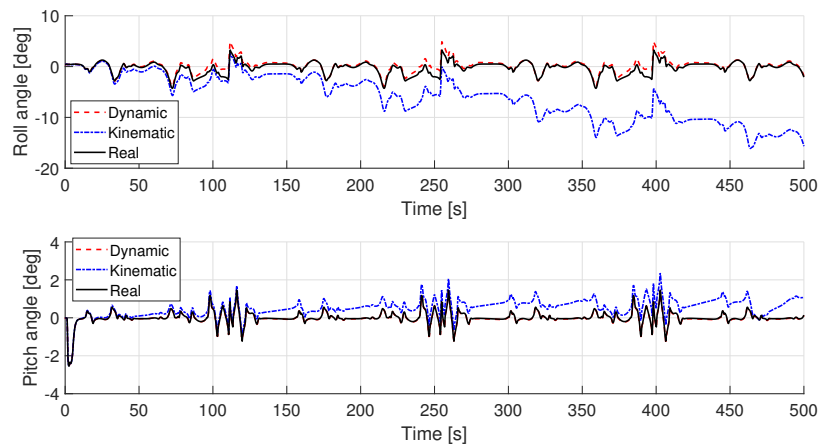


Figure 6.4: Estimation performance of driving on the Hockenheim racetrack

Looking at Table 6.2 also shows that the maximum deviations of the pitch angle of the dynamic observer are about ten times smaller than the maximum deviations of the kinematic observer. This is valid for all manoeuvres. The large deviations of the pitch angle of the kinematic observer during the fishhook manoeuvre and the drive on the Hockenheim racetrack can be explained again by the coupling of the states.

The limitations of the kinematic observer are also clearly visible in the braking manoeuvres. For normal braking the maximum deviation of the roll and pitch angle is comparable to the dynamic observer. When the emergency braking manoeuvre is performed, the maximum deviations of the dynamic observer only increase slightly, while the deviations of the kinematic observer increase significantly.

The reader is referred to Appendix B to see the figures of the estimation performance of the roll and pitch angle of the rest of the manoeuvres.

6.1.2. Noise Added

In this section the estimation results are shown when noisy sensor data is added to the inputs of both the kinematic and dynamic observers. In Section 5.3 the noise powers were specified.

In Table 6.3 the RMS errors of the roll and pitch angle of both observers can be seen. Looking at the RMS errors shows that now there is a significant performance difference between the observers. The RMS errors of the roll and pitch angle of the kinematic observer exceed the threshold of 1° for every manoeuvre. The RMS error of the roll angle of the dynamic observer stays in all manoeuvres except the Hockenheim racetrack below the threshold and for the Hockenheim racetrack the threshold is only exceeded by 0.35° . The RMS errors show that including dynamics into an observer clearly increases the estimation performance when noise is added to the input of the observers.

From Table 6.3 it can also be observed that the RMS errors of the pitch estimation for the dynamic observer exceed the threshold of 1° only slightly, but that the performance is worse than the roll angle estimation. This can be explained that for the roll angle estimation the lateral tyre forces are used to calculate the lateral acceleration, instead of using the lateral accelerometer measurements. The pitch angle estimation is based on the longitudinal accelerometer measurements. The comparison of the estimation results shows that using the tyre forces leads to better estimation performance.

Table 6.3: RMS errors of the observers for different manoeuvres, when sensor noise is present

Manoeuvre	RMS error roll [°]		RMS error pitch [°]	
	Dynamic	Kinematic	Dynamic	Kinematic
Sine sweep	0.7782	3.8767	1.2725	3.5937
Step response	0.8606	6.5113	1.1617	4.0567
Double lane change	0.4277	3.5010	1.4080	4.1551
Skidpad	1.6608	13.1638	1.2686	2.9869
Fishhook	0.8592	2.8232	1.1246	4.6954
Normal braking straight line	0.2582	4.0345	1.3427	4.4898
Emergency braking straight line	0.3578	3.9432	1.2720	4.1148
Hockenheim racetrack	1.3549	32.8858	1.1764	10.8381

Calculation of the longitudinal tyre forces can be performed in the same way as the lateral tyre forces using the exponential tyre model. To ensure that the longitudinal tyre forces are calculated correctly, their sum needs to be compared to the longitudinal acceleration, which basically means that one is estimating the longitudinal velocity. The longitudinal velocity can already accurately calculated using the wheel speed sensors. This basically means that the estimation algorithm will be made much more complex, due to all the derivatives needed for the Jacobian elements, with the prospect of only a slight increase in estimation performance of the pitch angle. Due to this reason the longitudinal accelerometer measurements are used in this thesis instead of longitudinal tyre forces.

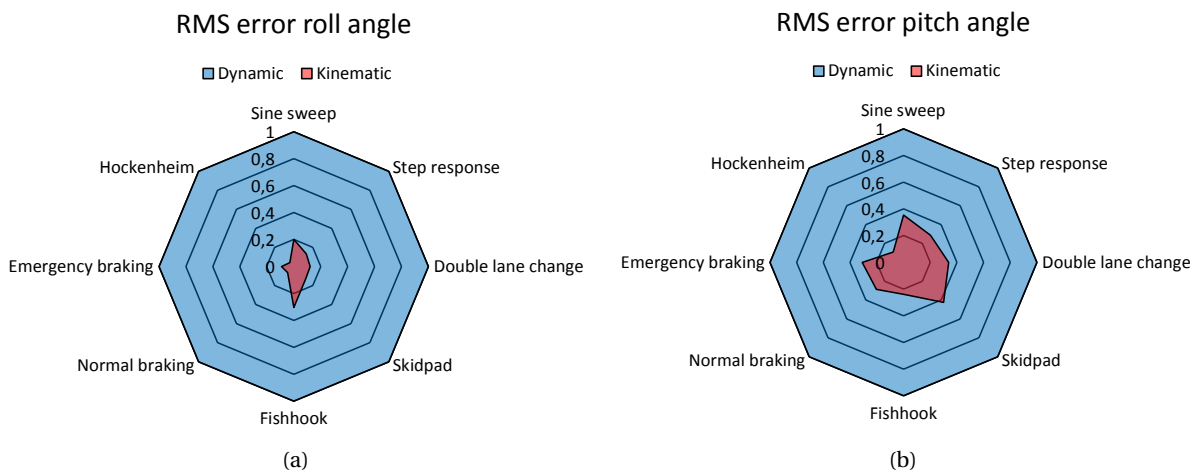


Figure 6.5: RMS error of the observers at each manoeuvre normalised to the best performing observer. Roll angle (a) and pitch angle (b)

In Figure 6.5 the RMS errors of the roll and pitch angle from Table 6.3 are visualised. Again at every manoeuvre the RMS error is normalised to the best performing observer. It can be observed that at every manoeuvre the dynamic observer performs better than the kinematic observer. Comparing Figure 6.5 to Figure 6.2 where no sensor noise was present, it becomes clear that when sensor noise is added to the observer, the relative performance of the dynamic observer increases regarding the roll angle in comparison to the kinematic observer. The relative performance of the kinematic observer regarding the pitch angle estimation increases in comparison to the dynamic observer.

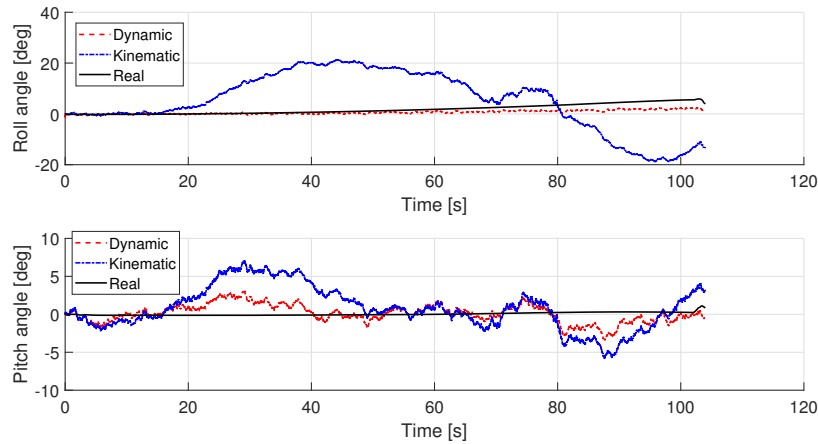


Figure 6.6: Estimation performance during the skidpad manoeuvre with noise added

Remembering the estimation performance of roll angle for the skidpad manoeuvre in the previous section, where the kinematic observer performed better than the dynamic observer. If one looks at Table 6.3 and Figure 6.6 the opposite is the case when sensor noise is added to the inputs. It can be seen that the kinematic observer performs quite badly now sensor noise is added. A possible explanation for this is that the kinematic observer cannot remove the external accelerations properly due to the noisy signals. This means that the drift introduced by the gyroscopes cannot be corrected correctly. Due to the long duration of the accelerations the drift error grows to a very large value over time.

Table 6.4: Maximum deviation of the observers for different manoeuvres, when sensor noise is present

Manoeuvre	Maximum deviation roll [°]		Maximum deviation pitch [°]	
	Dynamic	Kinematic	Dynamic	Kinematic
Sine sweep	2.0338	11.2480	3.3578	9.5886
Step response	2.1851	13.7164	3.2679	9.5397
Double lane change	1.9599	10.2049	3.2793	10.0071
Skidpad	4.1082	24.2128	3.7738	7.2200
Fishhook	3.7138	9.6585	3.0597	10.5294
Normal braking straight line	1.2001	10.0706	3.2980	9.6640
Emergency braking straight line	2.4177	10.0706	3.2980	9.6640
Hockenheim racetrack	4.0089	58.2015	3.8360	28.4421

The explanation that the external accelerations cannot be removed properly due to the noisy signals could also be used to the other manoeuvres, but in these manoeuvres the accelerations do not hold on for extensive periods of time, which results in lower RMS errors. What also does not help is that the roll and pitch angle are coupled in the state vector. An incorrect roll angle estimate leads also to an incorrect pitch angle estimate.

In Table 6.4 the maximum deviation of the estimates of the observers compared the real roll and pitch angle can be seen. It can be seen that the threshold of 2° is exceeded for both observers for almost all manoeuvres. Only during the double lane change manoeuvre and the normal braking the maximum deviation of the dynamic observer stays below 2° . The threshold of the maximum deviation of the roll angle of the dynamic observer is for the rest of the manoeuvres only just exceeded. The maximum deviation of the pitch angle of the dynamic observer is for almost all manoeuvres equal to about 3° . This can be explained by again by the noisy sensor input of the longitudinal accelerometer used for the calculation of the pitch angle.

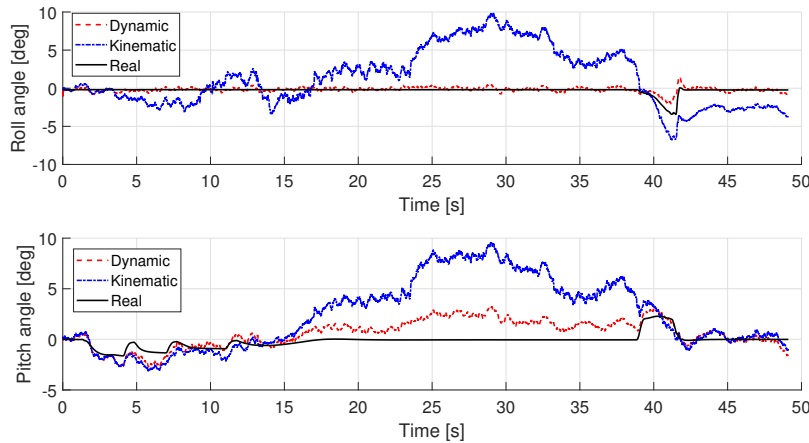


Figure 6.7: Estimation performance during the emergency braking manoeuvre with noise added

One thing that can also be noted from Table 6.4 and what can also be seen in Figure 6.7 is that the maximum deviation of the roll angle for the kinematic observer is almost 10° for the straight line braking manoeuvres. Due to the coupling of the roll and pitch angle in the states, this also leads to a high deviation of the pitch angle. The algorithm has trouble with removing the external accelerations when there are noisy sensor inputs and cannot remove the drift introduced by the gyroscopes.

The reader is referred to Appendix B to see the figures of the rest of the manoeuvres.

6.1.3. Sensor Quality Dependence

To see what the effect the gyroscope sensor quality has on the estimation performance of the observers, the gyroscope noise that was added to the inputs of the observers was varied over an interval. The noise added to the other inputs, which are the accelerometers and velocity sensor, were set to zero. The noise of the gyroscope was varied between 0 and the value specified in Section 5.3.

The off diagonal noise values of the process noise covariance matrix \mathbf{Q} of the dynamic observer turned out to be not linearly dependent to the increased noise of the gyroscope sensor. After trial and error it turned out that the best results were achieved when the process noise covariance matrix \mathbf{Q} for the dynamic observer was held constant over the range of varying gyroscope sensor noise and set equal to the same value as when maximum noise is added to the inputs of the observer.

In Figure 6.8 the RMS errors of the roll and pitch angle can be seen as a function of the noise power of the gyroscope noise for the double lane change manoeuvre. The noise power is given as an input of the band limited white noise block that generates the noise that is added to the gyroscopes. It becomes clear that the RMS errors of the roll and pitch angle of the kinematic observer increase significantly over the range, whereas the RMS error of the pitch angle of the dynamic observer only increases slightly and the RMS error of the roll angle of the dynamic observer stays more or less constant.

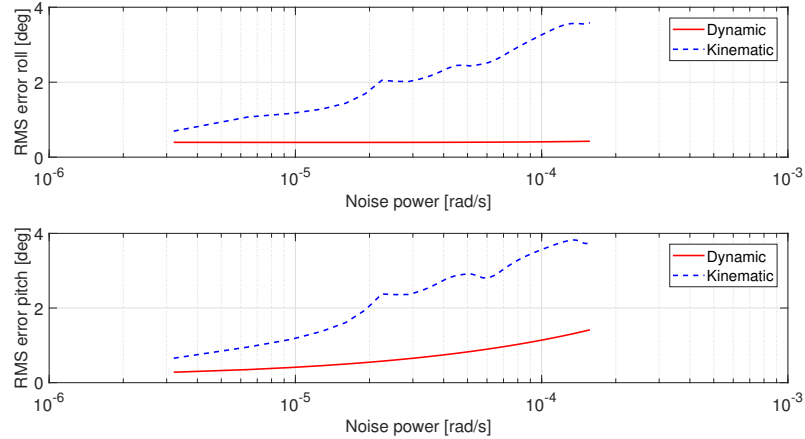


Figure 6.8: RMS errors of the observers as a function of gyroscope sensor quality of the double lane change manoeuvre

The results from Figure 6.8 are as expected. When the noise power increases the kinematic observer has difficulty to remove the external accelerations when the sensor values become noisy and so the RMS error of the roll and pitch angle increases. The coupling of the states in the kinematic observer can also be observed in the figure. When there is a small peak in the RMS error of the roll angle, the peak becomes also visible in the RMS error of the pitch angle.

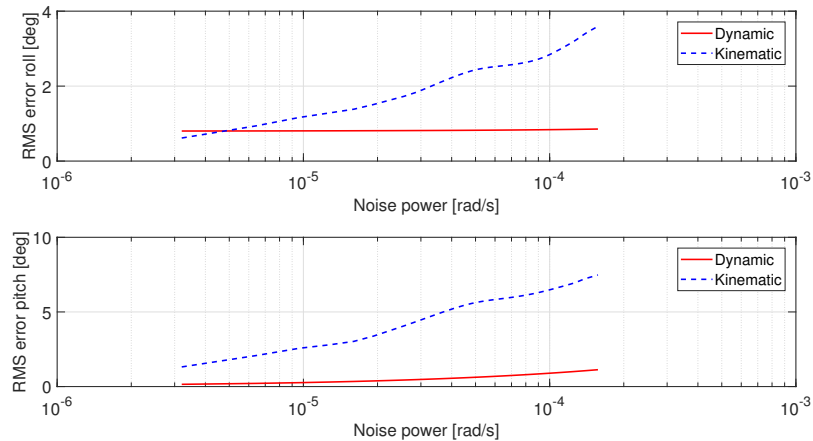


Figure 6.9: RMS errors of the observers as a function of gyroscope sensor quality of the fishhook manoeuvre

In Figure 6.9 the RMS error of the roll and pitch angle can be seen as a function of the noise power of the gyroscope noise for the fishhook manoeuvre. It can again be observed that the RMS errors of the kinematic observer increase when the noise power increases. What also can be seen is that the RMS error of the dynamic observer for the roll angle stays more less constant over the range of noise power and for low noise powers it is higher than the RMS error of the kinematic observer. This can be explained by the fact that the process noise covariance matrix \mathbf{Q} was set constant over the entire range of noise powers. It was set equal to same value as when maximum noise was added to the inputs of the observer for the entire range of noise power. This means that for low noise power, so low sensor noise, the tuning of the \mathbf{Q} matrix is not optimal, which results in a higher RMS error of the roll angle. The RMS error of the pitch angle is less effected by this, which results in a low RMS error for low noise powers.

6.2. Lateral Velocity Dynamic Observer

The dynamic observer does not only estimates the roll and pitch angle, but also the lateral velocity. In this section the estimation results are presented of the lateral velocity. In Table 6.5 the RMS error of the lateral velocity estimates can be seen. In the table the results are shown for each manoeuvre when no sensor noise is added to the inputs and when maximum sensor noise, as specified in Section 5.3, is added to the inputs of the observer. From the table it becomes clear that the RMS error does not increase much when sensor noise is added to the inputs of the observer.

Table 6.5: RMS error of lateral velocity estimate, when there is no noise and noise is present

Manoeuvre	RMS error lateral velocity no noise [m s^{-1}]	RMS error lateral velocity maximum noise [m s^{-1}]
Sine sweep	0.0441	0.0615
Step response	0.0154	0.0478
Double lane change	0.0360	0.0583
Skidpad	0.1281	0.1338
Fishhook	0.0952	0.1005
Hockenheim racetrack	0.1178	0.1241

Only for the skidpad manoeuvre and the Hockenheim racetrack the RMS error exceeds 0.1 m s^{-1} . As explained in previous sections this can be explained by the fact that there is a mismatch at high slip values in the calculated tyre force in the internal vehicle model and the actual tyre forces. In the skidpad manoeuvre and the Hockenheim racetrack there are constantly large accelerations and so large slip values, making the RMS error large.

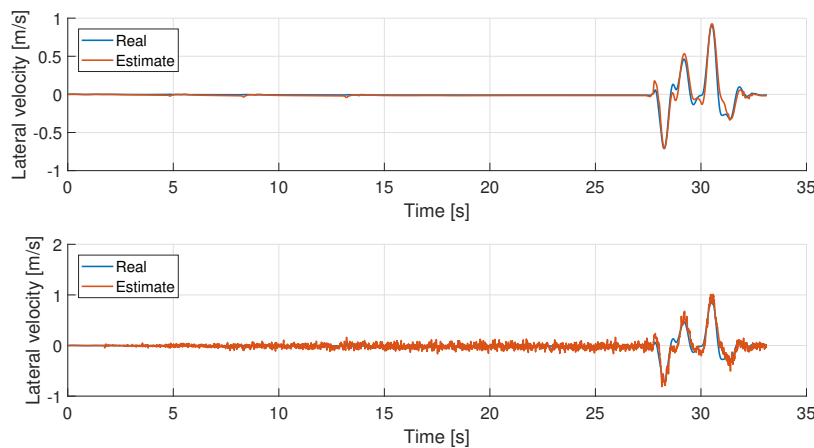


Figure 6.10: Estimation performance lateral velocity during the double lane manoeuvre

In Figure 6.10 the lateral velocity estimates can be seen of the double lane change manoeuvre, when no sensor noise is added to the inputs and when sensor noise is added to the inputs. It becomes clear that the estimated lateral velocities match quite well with the real lateral velocity. For this manoeuvre the steering rate is relatively low, which means that the slip in this manoeuvre is also relatively small and the calculated tyre forces match the actual values quite well.

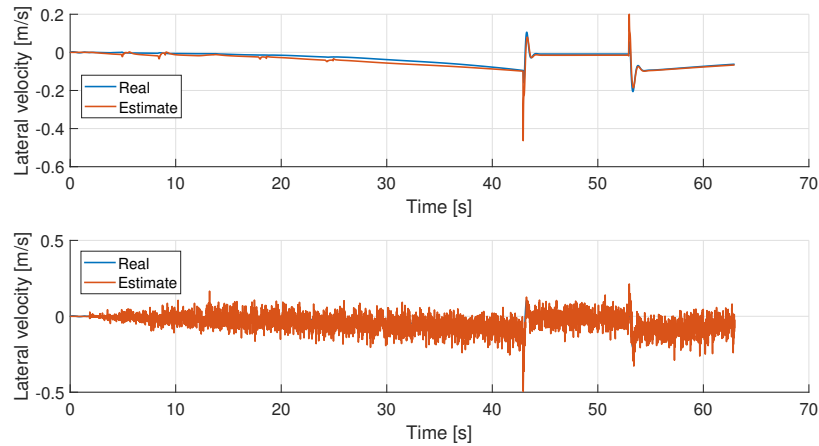


Figure 6.11: Estimation performance lateral velocity during the step response manoeuvre

This result is different when a rapid steering input is applied, which is the case in the step response manoeuvre. The estimation result can be seen in Figure 6.11 for the whole manoeuvre. At first sight the overall estimate matches up quite well with the real value, but if one zooms in on the actual manoeuvre, a mismatch between the estimate and the real value becomes visible.

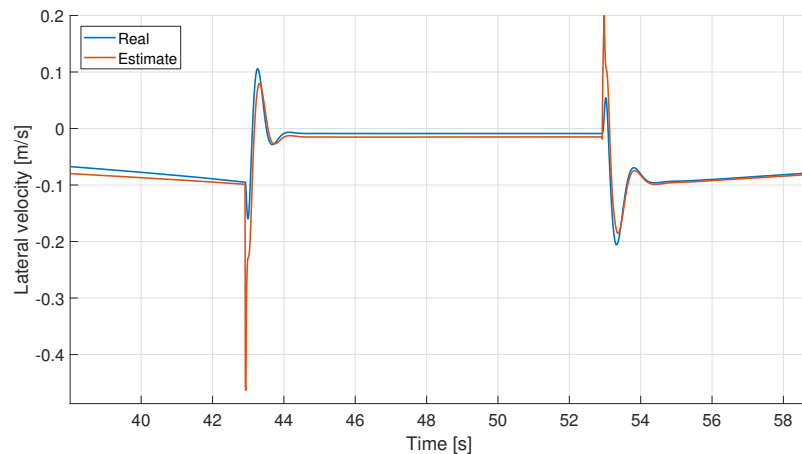


Figure 6.12: Close up lateral velocity estimate of the step response manoeuvre

In Figure 6.12 close up of the actual manoeuvre can be seen. It becomes clear that when the step response steering input is applied the estimate is off. There are large slip values present during the step response, which leads to a mismatch of the calculated tyre forces and the actual tyre forces. The calculated tyre forces are too high compared the the actual ones, leading to an over estimation of the lateral velocity.

Table 6.6: Maximum deviation of lateral velocity estimates with respect to true value for the different manoeuvres with no noise and noise present

Manoeuvre	Maximum deviation no noise [ms^{-1}]	Maximum deviation noise [ms^{-1}]
Sine sweep	0.1440	0.2716
Step response	0.3629	0.3941
Double lane change	0.2270	0.3344
Skidpad	0.7903	1.0540
Fishhook	1.0982	1.0989
Hockenheim racetrack	0.5575	0.9475

In Table 6.6 the maximum deviation of the lateral velocity estimate with respect to the true value for the different manoeuvres can be seen. It can be observed that the maximum deviations are the highest for manoeuvres that consist of high steering angle rates. Especially in the fishhook test, which consists of a very rapid steering input, the maximum deviation is high. What also can be observed from the table is that compared to the RMS errors in Table 6.5 the maximum deviations are quite high. This can be explained by the fact that the estimate is off for a short time period as the steering input is applied. The rest of the manoeuvre the lateral velocity estimate matches the true value well, which can also be seen in Figure 6.11.

The reader is referred to Appendix C to see the figures of the estimation results of the sine sweep, skidpad, fishhook and the Hockenheim racetrack.

Conclusion and Recommendations

7.1. Conclusion

7.1.1. Roll and Pitch Angle Estimation

In this thesis report a dynamic and kinematic observer were compared that estimate the roll and pitch angle. The dynamic observer was developed, because kinematic observers give inaccurate estimation results during extreme driving situations, because kinematic relations do not take into account tyre behaviour. The goal of this thesis was to develop an dynamic observer that gives accurate estimation results even in those extreme driving situations. The estimation performance was not only assessed using the actual roll and pitch angle, but also compared against a kinematic observer. The kinematic observer was developed by Ahmed & Tahir [7].

From the results it can be concluded that when no sensor noise is added to the inputs of the observers similar performance is achieved by both observers. Only at manoeuvres with high accelerations, where the slip has a dominant effect, some deviation between the dynamic and kinematic estimator is observed, because kinematic relations do not take into the slip. When sensor noise is added to the inputs of the observers, the estimation performance becomes different. Then the dynamic observer performs much better than the kinematic observer.

Including dynamics significantly improves the estimation performance of the dynamic observer. Because the observer has an internal model that calculates the roll and pitch angle quite accurately, its performance is not influenced a lot by the noisy sensor measurements. It also has been shown that calculating the lateral acceleration using an exponential tyre model leads to a more accurate estimation, than when the noisy acceleration sensor measurements are used, but as already explained in Chapter 6 incorporating longitudinal tyre forces makes the observer a lot more complex and with the prospect that the estimate of the pitch angle only slightly increases, the longitudinal tyre forces are not calculated and used in this thesis.

From the results it also becomes clear that the estimates of the roll and pitch angle of the kinematic observer drastically decrease when sensor noise is added to the inputs of the observer. The algorithm has trouble removing the external accelerations when the sensor measurements are noisy and due to that reason the kinematic observer cannot correct the drift of the gyroscopes accurately.

The contributions of this thesis to the scientific field are firstly that using an exponential tyre model inside a dynamic observer the roll and pitch angle can be accurately estimated. Even in conjunction with low quality sensors that have high noise in their measurements, accurate estimation results are achieved. The second contribution is that for the first time the estimation performance of a dynamic observer that estimates the roll and pitch angle is compared to a kinematic observer.

Recalling from the introduction that accurate estimates of the roll and pitch angle were desired, because the roll angle is used in roll stability control systems and the roll and pitch angle used for image correction of the stereo camera and for comfort assessment in autonomous vehicles. In this thesis it has been shown that using a dynamic observer the roll and pitch angle can be accurately estimated even using low quality sensors and thus the estimates of the dynamic observer can be used for those applications. It has also been shown that a kinematic observer fails to estimate the roll and pitch angle when low quality sensors are used and cannot be used for those applications.

7.1.2. Lateral Velocity Estimation

In this thesis an attempt was also made to estimate the lateral velocity in the dynamic observer. From the results it can be concluded that the estimated lateral velocity does not drift away from the true lateral velocity. It can also be concluded that the estimated lateral velocity follows the true value quite well when a gradual steering input is applied. Only if a rapid steering input is applied, the estimate of the lateral velocity deviates from the true lateral velocity.

This deviation during rapid steering inputs is caused by a mismatch at high slip values in the calculated tyre forces in the internal vehicle model. Although the exponential tyre model takes into account saturation, combined slip and vertical load dependency, it does not take into account the peak force and force drop off. Because the peak force and drop off are not modelled, the calculated tyre forces are too high at higher slip values.

In the introduction it was mentioned that the lateral velocity estimates are used to calculate the lateral side slip angle α . Having an accurate estimate of the side slip angle could lead to the development of new safety systems. For manoeuvres with a rapid steering input, the lateral velocity that is estimated in this thesis are sadly not good enough in order to be used to calculate the side slip angle. In the next section a recommendation is made to improve the estimation of the lateral velocity.

7.2. Recommendations

After performing this thesis study a few recommendations can be given to improve the state estimation of the dynamic observer:

An improvement can be made to the tyre force calculation by including the peak force and also force drop off at high slip values. The exponential tyre model can be extended by a second exponential term, which is proposed in [38]. Adding an extra exponential could lead to better calculated tyre forces at high slip values, which in turn leads to a better estimated lateral velocity when a rapid steering input is applied, such as for example in a step response manoeuvre.

In this thesis the tyre/road-friction coefficient μ is always equal to 1. This is a great assumption if the vehicle is driving on dry asphalt, but when the vehicle is driving on a wet road or even on ice, the assumption is not correct anymore. The tyre/road-friction coefficient then becomes close to zero. So for actual driving in the real world, it is better to make this constant dependent of the weather. This can be done in two ways. The first way is to make it a state in the Kalman filter, where it will be estimated. If the vehicle is equipped with a camera, the images could also be used to estimate the tyre/road-friction coefficient.

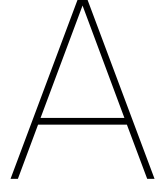
Lastly, in this thesis the performance of the dynamic observer was investigated using IPG CarMaker. Although this is a highly advanced vehicle simulation environment, which approximates the true vehicle dynamic behaviour well, there will always be some minor differences in the vehicle dynamic behaviour. To analyse the performance of the dynamic observer further, it would be beneficial to test the dynamic observer on a real vehicle doing actual manoeuvres and check if the observer shows similar performance as in IPG CarMaker.

Bibliography

- [1] Basam Musleh, David Martín, José María Armingol, and Arturo de la Escalera. Pose self-calibration of stereo vision systems for autonomous vehicle applications. *Sensors*, 16(9):1492, 2016.
- [2] Vladyslav Usenko, Jakob Engel, Jörg Stückler, and Daniel Cremers. Direct visual-inertial odometry with stereo cameras. In *Robotics and Automation (ICRA), 2016 IEEE International Conference on*, pages 1885–1892. IEEE, 2016.
- [3] Michael Santoro, Ghassan AlRegib, and Yucel Altunbasak. Misalignment correction for depth estimation using stereoscopic 3-d cameras. In *Multimedia Signal Processing (MMSp), 2012 IEEE 14th International Workshop on*, pages 19–24. IEEE, 2012.
- [4] J-S Jo, S-H You, Ji Yoel Joeng, Kyo Il Lee, and Kyongsu Yi. Vehicle stability control system for enhancing steerability, lateral stability, and roll stability. *International Journal of Automotive Technology*, 9(5):571, 2008.
- [5] Michael Sivak and Brandon Schoettle. Motion sickness in self-driving vehicles. 2015.
- [6] Judith A Joseph and Michael J Griffin. Motion sickness: Effect of the magnitude of roll and pitch oscillation. *Aviation, space, and environmental medicine*, 79(4):390–396, 2008.
- [7] Hamad Ahmed and Muhammad Tahir. Accurate attitude estimation of a moving land vehicle using low-cost mems imu sensors. *IEEE Transactions on Intelligent Transportation Systems*, 18(7):1723–1739, 2017.
- [8] Kanghyun Nam, Sehoon Oh, Hiroshi Fujimoto, and Yoichi Hori. Vehicle state estimation for advanced vehicle motion control using novel lateral tire force sensors. In *American Control Conference (ACC), 2011*, pages 4853–4858. IEEE, 2011.
- [9] Jason Kong, Mark Pfeiffer, Georg Schildbach, and Francesco Borrelli. Kinematic and dynamic vehicle models for autonomous driving control design. In *Intelligent Vehicles Symposium*, pages 1094–1099, 2015.
- [10] Havard Fjaer Grip, Lars Imsland, Tor A Johansen, Jens C Kalkkuhl, and Avshalom Suissa. Vehicle sideslip estimation. *IEEE control systems*, 29(5), 2009.
- [11] Marc Barnada, Christian Conrad, Henry Bradler, Matthias Ochs, and Rudolf Mester. Estimation of automotive pitch, yaw, and roll using enhanced phase correlation on multiple far-field windows. In *Intelligent Vehicles Symposium (IV), 2015 IEEE*, pages 481–486. IEEE, 2015.
- [12] Kanghyun Nam, Sehoon Oh, Hiroshi Fujimoto, and Yoichi Hori. Estimation of sideslip and roll angles of electric vehicles using lateral tire force sensors through rls and kalman filter approaches. *IEEE Transactions on Industrial Electronics*, 60(3):988–1000, 2013.
- [13] Neil Barbour and George Schmidt. Inertial sensor technology trends. *IEEE Sensors journal*, 1(4):332–339, 2001.
- [14] David M Bevly, Jihan Ryu, and J Christian Gerdes. Integrating ins sensors with gps measurements for continuous estimation of vehicle sideslip, roll, and tire cornering stiffness. *IEEE Transactions on Intelligent Transportation Systems*, 7(4):483–493, 2006.
- [15] David M Bevly. Global positioning system (gps): A low-cost velocity sensor for correcting inertial sensor errors on ground vehicles. *Transactions-American society of mechanical engineers journal of dynamic systems measurement and control*, 126(2):255–264, 2004.
- [16] Jihan Ryu and J Christian Gerdes. Integrating inertial sensors with global positioning system (gps) for vehicle dynamics control. *Transactions-American society of mechanical engineers journal of dynamic systems measurement and control*, 126(2):243–254, 2004.

- [17] James J Spiker and BW Parkinson. The global positioning system: Theory and application. *American Institute of Aeronautics and Astronautics: Washington, DC, USA*, 1996.
- [18] Lei Wang, Paul D Groves, and Marek K Ziebart. Multi-constellation gnss performance evaluation for urban canyons using large virtual reality city models. *The Journal of Navigation*, 65(3):459–476, 2012.
- [19] Minha Park and Yang Gao. Error analysis and stochastic modeling of low-cost mems accelerometer. *Journal of Intelligent & Robotic Systems*, 46(1):27–41, 2006.
- [20] Ehsan Hashemi, Reza Zarringhalam, Amir Khajepour, William Melek, Alireza Kasaiezadeh, and Shih-Ken Chen. Real-time estimation of the road bank and grade angles with unknown input observers. *Vehicle System Dynamics*, 55(5):648–667, 2017.
- [21] Beatriz L Boada, Daniel Garcia-Pozuelo, Maria Jesus L Boada, and Vicente Diaz. A constrained dual kalman filter based on pdf truncation for estimation of vehicle parameters and road bank angle: Analysis and experimental validation. *IEEE Transactions on Intelligent Transportation Systems*, 18(4):1006–1016, 2017.
- [22] H Eric Tseng, Li Xu, and Davor Hrovat. Estimation of land vehicle roll and pitch angles. *Vehicle System Dynamics*, 45(5):433–443, 2007.
- [23] Gamini Dissanayake, Salah Sukkarieh, Eduardo Nebot, and Hugh Durrant-Whyte. The aiding of a low-cost strapdown inertial measurement unit using vehicle model constraints for land vehicle applications. *IEEE transactions on robotics and automation*, 17(5):731–747, 2001.
- [24] Sarah K Spurgeon. Sliding mode observers: a survey. *International Journal of Systems Science*, 39(8):751–764, 2008.
- [25] Ping Li, Roger Goodall, and Visakan Kadirkamanathan. Estimation of parameters in a linear state space model using a rao-blackwellised particle filter. *IEE Proceedings-control theory and applications*, 151(6):727–738, 2004.
- [26] Haiyan Zhao and Hong Chen. Estimation of vehicle yaw rate and side slip angle using moving horizon strategy. In *Intelligent Control and Automation, 2006. WCICA 2006. The Sixth World Congress on*, volume 1, pages 1828–1832. IEEE, 2006.
- [27] Rudolph Emil Kalman. A new approach to linear filtering and prediction problems. *Journal of basic Engineering*, 82(1):35–45, 1960.
- [28] Jihan Ryu and J Christian Gerdes. Estimation of vehicle roll and road bank angle. In *American Control Conference, 2004. Proceedings of the 2004*, volume 3, pages 2110–2115. IEEE, 2004.
- [29] Lowell S Brown and David M Bevely. Roll and bank estimation using gps/ins and suspension deflections. *Electronics*, 4(1):118–149, 2015.
- [30] Vincent Winstead and Ilya V Kolmanovsky. Estimation of road grade and vehicle mass via model predictive control. In *Control Applications, 2005. CCA 2005. Proceedings of 2005 IEEE Conference on*, pages 1588–1593. IEEE, 2005.
- [31] Per Sahlholm and Karl Henrik Johansson. Road grade estimation for look-ahead vehicle control using multiple measurement runs. *Control Engineering Practice*, 18(11):1328–1341, 2010.
- [32] Ling-Yuan Hsu and Tsung-Lin Chen. Estimating road angles with the knowledge of the vehicle yaw angle. *Journal of dynamic systems, measurement, and control*, 132(3):031004, 2010.
- [33] Kun Jiang, Adina Pavelescu, Alessandro Victorino, and Ali Charara. Estimation of vehicle’s vertical and lateral tire forces considering road angle and road irregularity. In *Intelligent Transportation Systems (ITSC), 2014 IEEE 17th International Conference on*, pages 342–347. IEEE, 2014.
- [34] Moustapha Doumiati, A Victorino, Daniel Lechner, G Baffet, and A Charara. Observers for vehicle tyre/road forces estimation: experimental validation. *Vehicle System Dynamics*, 48(11):1345–1378, 2010.

-
- [35] Michel Verhaegen and Vincent Verdult. *Filtering and system identification: a least squares approach*. Cambridge university press, 2007.
- [36] Shahrokh Akhlaghi, Ning Zhou, and Zhenyu Huang. Adaptive adjustment of noise covariance in kalman filter for dynamic state estimation. In *Power & Energy Society General Meeting, 2017 IEEE*, pages 1–5. IEEE, 2017.
- [37] Matt C Best. Exploring assumptions and requirements for continuous modification of vehicle handling using non-linear optimal control and a new exponential tyre model. 2010.
- [38] Matthew C Best. A new empirical ‘exponential’ tyre model. *International Journal of Vehicle Design*, 65(2-3):241–255, 2014.
- [39] Hans Pacejka. *Tire and vehicle dynamics*. Elsevier, 2005.
- [40] J Kim. Identification of lateral tyre force dynamics using an extended kalman filter from experimental road test data. *Control Engineering Practice*, 17(3):357–367, 2009.
- [41] R van Hoek. Vehicle state estimation using the state dependent riccati equation technique. *Master thesis TU Eindhoven*, 2015.
- [42] Rajesh Rajamani. *Vehicle dynamics and control*. Springer Science & Business Media, 2011.
- [43] Gregory G Slabaugh. Computing euler angles from a rotation matrix. *Retrieved on August, 6, 2000*:39–63, 1999.
- [44] Shahid Ayub, Alireza Bahraminasab, and Bahram Honary. A sensor fusion method for smart phone orientation estimation. 2012.
- [45] Jung Keun Lee, Edward J Park, and Stephen N Robinovitch. Estimation of attitude and external acceleration using inertial sensor measurement during various dynamic conditions. *IEEE transactions on instrumentation and measurement*, 61(8):2262–2273, 2012.
- [46] Andrzej Reński. Identification of driver model parameters. *International Journal of occupational safety and ergonomics*, 7(1):79–92, 2001.



Derivations

In this appendix all the derivatives are presented needed for the calculation of the Jacobians A_k and H_k . Recalling that the Jacobians A_k and H_k are defined as

$$A_{ij} = \frac{\partial f_i(x, u)}{\partial x_j} \quad \text{with } i = \{1, 2, 3, 4, 5, 6\} \quad \text{and } j = \{1, 2, 3, 4, 5, 6\} \quad (\text{A.1})$$

$$H_{ij} = \frac{\partial f_i(x, u)}{\partial x_j} \quad \text{with } i = \{1, 2, 3, 4\} \quad \text{and } j = \{1, 2, 3, 4, 5, 6\} \quad (\text{A.2})$$

Where the Jacobian elements are numbered according to the definition of the state and output vector as in Section 3.1.1. Recalling that the state and output vector were defined as

$$\mathbf{x} = [v_y \quad \dot{\psi} \quad \phi \quad \dot{\phi} \quad \theta \quad \dot{\theta}]^T$$

$$\mathbf{z} = [a_y \quad \dot{\psi} \quad \dot{\phi} \quad \dot{\theta}]^T$$

A.1. Derivatives Tyre Forces

The partial derivatives of the lateral tyre forces are done using equations (3.51) and (3.52) and are defined below.

The partial derivative with respect to the lateral speed v_y is defined as

$$\left(\frac{\partial F_{y,FL}}{\partial v_y} \right)_{Positive \alpha} = -\mu F_{z,FL} K_F \exp^{-K_{y,F} \left(-\frac{v_y + l_f \dot{\psi}}{v_x} + \delta_F \right)} \frac{1}{v_x} \quad (\text{A.3})$$

$$\left(\frac{\partial F_{y,FL}}{\partial v_y} \right)_{Negative \alpha} = -\mu F_{z,FL} K_F \exp^{K_{y,F} \left(-\frac{v_y + l_f \dot{\psi}}{v_x} + \delta_F \right)} \frac{1}{v_x} \quad (\text{A.4})$$

Combining the positive and negative slip gives

$$\frac{\partial F_{y,F}}{\partial v_y} = -\mu F_{z,FL} K_{y,F} \exp^{-K_{y,F} |\alpha_{FL}|} \frac{1}{v_x} \quad (\text{A.5})$$

The partial derivatives with respect to the yaw rate is defined as

$$\left(\frac{\partial F_{y,FL}}{\partial \dot{\psi}} \right)_{Positive \alpha} = -\mu F_{z,FL} K_{y,F} \exp^{-K_{y,F} \left(-\frac{v_y + l_f \dot{\psi}}{v_x} + \delta_f \right)} \frac{l_f}{v_x} \quad (\text{A.6})$$

$$\left(\frac{\partial F_{y,FL}}{\partial \dot{\psi}} \right)_{Negative \alpha} = -\mu F_{z,FL} K_{y,F} \exp^{K_{y,F} \left(-\frac{v_y + l_f \dot{\psi}}{v_x} + \delta_f \right)} \frac{l_f}{v_x} \quad (\text{A.7})$$

Combining the positive and negative slip gives

$$\frac{\partial F_{y,FL}}{\partial \dot{\psi}} = \mu F_{z,FL} K_{y,F} \exp^{-K_{y,F} |\alpha_F L|} \frac{l_f}{v_x} \quad (\text{A.8})$$

To avoid divisions by zero a condition is set. The derivations of the lateral velocity are only calculated when the longitudinal velocity is greater than 0.5 m s^{-1} . When the longitudinal velocity is smaller than 0.5 m s^{-1} the derivations are set to zero.

A.2. Derivatives of Jacobian Elements

The elements of the A_k matrix containing the partial derivative with respect to the lateral velocity v_y are defined as

$$A_{11} = \frac{\partial \dot{v}_y}{\partial v_y} = 1 + t_s \left(\frac{1}{m_{tot}} \left(\frac{\partial F_{y,FL}}{\partial v_y} + \frac{\partial F_{y,FR}}{\partial v_y} + \frac{\partial F_{y,RL}}{\partial v_y} + \frac{\partial F_{y,RR}}{\partial v_y} \right) \right) \quad (\text{A.9})$$

$$A_{21} = \frac{\partial \dot{\psi}}{\partial v_y} = t_s \left(\frac{l_f}{I_{zz}} \left(\frac{\partial F_{y,FL}}{\partial v_y} + \frac{\partial F_{y,FR}}{\partial v_y} \right) - \frac{l_r}{I_{zz}} \left(\frac{\partial F_{y,RL}}{\partial v_y} + \frac{\partial F_{y,RR}}{\partial v_y} \right) \right) \quad (\text{A.10})$$

$$A_{31} = \frac{\partial \dot{\phi}}{\partial v_y} = 0 \quad (\text{A.11})$$

$$A_{41} = \frac{\partial \ddot{\phi}}{\partial v_y} = t_s \left(\frac{m_s h_r}{I_{xx}} \left(\frac{1}{m_{tot}} \left(\frac{\partial F_{y,FL}}{\partial v_y} + \frac{\partial F_{y,FR}}{\partial v_y} + \frac{\partial F_{y,RL}}{\partial v_y} + \frac{\partial F_{y,RR}}{\partial v_y} \right) \right) \right) \quad (\text{A.12})$$

$$A_{51} = \frac{\partial \dot{\theta}}{\partial v_y} = 0 \quad (\text{A.13})$$

$$A_{61} = \frac{\partial \ddot{\theta}}{\partial v_y} = 0 \quad (\text{A.14})$$

The elements of the H_k matrix containing the partial derivatives to the lateral velocity v_y are defined as

$$H_{11} = \frac{\partial a_y}{\partial v_y} = \frac{1}{m_{tot}} \left(\frac{\partial F_{y,FL}}{\partial v_y} + \frac{\partial F_{y,FR}}{\partial v_y} + \frac{\partial F_{y,RL}}{\partial v_y} + \frac{\partial F_{y,RR}}{\partial v_y} \right) \quad (\text{A.15})$$

$$H_{21} = \frac{\partial \dot{\psi}}{\partial v_y} = 0 \quad (\text{A.16})$$

$$H_{31} = \frac{\partial \dot{\phi}}{\partial v_y} = 0 \quad (\text{A.17})$$

$$H_{41} = \frac{\partial \dot{\theta}}{\partial v_y} = 0 \quad (\text{A.18})$$

$$(\text{A.19})$$

The elements of the A_k matrix containing the derivatives with respect to the yaw rate $\dot{\psi}$ are defined as

$$A_{12} = \frac{\partial \dot{v}_y}{\partial \dot{\psi}} = t_s \left(\frac{1}{m_{tot}} \left(\frac{\partial F_{y,FL}}{\partial \dot{\psi}} + \frac{\partial F_{y,FR}}{\partial \dot{\psi}} + \frac{\partial F_{y,RL}}{\partial \dot{\psi}} + \frac{\partial F_{y,RR}}{\partial \dot{\psi}} \right) - v_x \right) \quad (\text{A.20})$$

$$A_{22} = \frac{\partial \dot{\psi}}{\partial \dot{\psi}} = 1 + t_s \left(\frac{l_f}{I_{zz}} \left(\frac{\partial F_{y,FL}}{\partial \dot{\psi}} + \frac{\partial F_{y,FR}}{\partial \dot{\psi}} \right) - \frac{l_r}{I_{zz}} \left(\frac{\partial F_{y,RL}}{\partial \dot{\psi}} + \frac{\partial F_{y,RR}}{\partial \dot{\psi}} \right) \right) \quad (\text{A.21})$$

$$A_{32} = \frac{\partial \dot{\phi}}{\partial \dot{\psi}} = 0 \quad (\text{A.22})$$

$$A_{42} = \frac{\partial \ddot{\phi}}{\partial \dot{\psi}} = t_s \left(\frac{m_s h_r}{I_{xx}} \left(\frac{1}{m_{tot}} \left(\frac{\partial F_{y,FL}}{\partial \dot{\psi}} + \frac{\partial F_{y,FR}}{\partial \dot{\psi}} + \frac{\partial F_{y,RL}}{\partial \dot{\psi}} + \frac{\partial F_{y,RR}}{\partial \dot{\psi}} \right) \right) \right) \quad (\text{A.23})$$

$$A_{52} = \frac{\partial \dot{\theta}}{\partial \dot{\psi}} = 0 \quad (\text{A.24})$$

$$A_{62} = \frac{\partial \ddot{\theta}}{\partial \dot{\psi}} = 0 \quad (\text{A.25})$$

The elements of the H_k matrix containing the derivatives with respect to the yaw rate $\dot{\psi}$ are defined as

$$H_{12} = \frac{\partial a_y}{\partial \dot{\psi}} = \frac{1}{m_{tot}} \left(\frac{\partial F_{y,FL}}{\partial \dot{\psi}} + \frac{\partial F_{y,FR}}{\partial \dot{\psi}} + \frac{\partial F_{y,RL}}{\partial \dot{\psi}} + \frac{\partial F_{y,RR}}{\partial \dot{\psi}} \right) \quad (\text{A.26})$$

$$H_{22} = \frac{\partial \dot{\psi}}{\partial \dot{\psi}} = 1 \quad (\text{A.27})$$

$$H_{32} = \frac{\partial \dot{\phi}}{\partial \dot{\psi}} = 0 \quad (\text{A.28})$$

$$H_{42} = \frac{\partial \dot{\theta}}{\partial \dot{\psi}} = 0 \quad (\text{A.29})$$

The elements of the A_k matrix containing the derivatives with respect to the roll angle ϕ are defined as

$$A_{13} = \frac{\partial \dot{v}_y}{\partial \phi} = 0 \quad (\text{A.30})$$

$$A_{23} = \frac{\partial \dot{\psi}}{\partial \phi} = 0 \quad (\text{A.31})$$

$$A_{33} = \frac{\partial \dot{\phi}}{\partial \phi} = 1 \quad (\text{A.32})$$

$$A_{43} = \frac{\partial \dot{\phi}}{\partial \phi} = t_s \left(\frac{1}{I_{xx}} (m_s g h_r - (K_{roll,f} + K_{roll,r})) \right) \quad (\text{A.33})$$

$$A_{53} = \frac{\partial \dot{\theta}}{\partial \phi} = 0 \quad (\text{A.34})$$

$$A_{63} = \frac{\partial \ddot{\theta}}{\partial \phi} = 0 \quad (\text{A.35})$$

The elements of the H_k matrix containing the derivatives with respect to the roll angle ϕ are defined as

$$H_{13} = \frac{\partial a_y}{\partial \phi} = 0 \quad (\text{A.36})$$

$$H_{23} = \frac{\partial \dot{\psi}}{\partial \phi} = 0 \quad (\text{A.37})$$

$$H_{33} = \frac{\partial \dot{\phi}}{\partial \phi} = 0 \quad (\text{A.38})$$

$$H_{43} = \frac{\partial \dot{\theta}}{\partial \phi} = 0 \quad (\text{A.39})$$

The elements of the A_k matrix containing the derivatives with respect to the roll rate $\dot{\phi}$ are defined as

$$A_{14} = \frac{\partial \dot{v}_y}{\partial \dot{\phi}} = 0 \quad (\text{A.40})$$

$$A_{24} = \frac{\partial \dot{\psi}}{\partial \dot{\phi}} = 0 \quad (\text{A.41})$$

$$A_{34} = \frac{\partial \dot{\phi}}{\partial \dot{\phi}} = t_s \quad (\text{A.42})$$

$$A_{44} = \frac{\partial \ddot{\phi}}{\partial \dot{\phi}} = 1 + t_s \left(-\frac{1}{I_{xx}} (D_{roll,f} + D_{roll,r}) \right) \quad (\text{A.43})$$

$$A_{54} = \frac{\partial \dot{\theta}}{\partial \dot{\phi}} = 0 \quad (\text{A.44})$$

$$A_{64} = \frac{\partial \ddot{\theta}}{\partial \dot{\phi}} = 0 \quad (\text{A.45})$$

The elements of the H_k matrix containing the derivatives with respect to the roll rate $\dot{\phi}$ are defined as

$$H_{14} = \frac{\partial a_y}{\partial \dot{\phi}} = 0 \quad (\text{A.46})$$

$$H_{24} = \frac{\partial \dot{\psi}}{\partial \dot{\phi}} = 0 \quad (\text{A.47})$$

$$H_{34} = \frac{\partial \dot{\phi}}{\partial \dot{\phi}} = 1 \quad (\text{A.48})$$

$$H_{44} = \frac{\partial \dot{\theta}}{\partial \dot{\phi}} = 0 \quad (\text{A.49})$$

The elements of the A_k matrix containing the derivatives with respect to the pitch angle θ are defined as

$$A_{15} = \frac{\partial \dot{v}_y}{\partial \theta} = 0 \quad (\text{A.50})$$

$$A_{25} = \frac{\partial \dot{\psi}}{\partial \theta} = 0 \quad (\text{A.51})$$

$$A_{35} = \frac{\partial \dot{\phi}}{\partial \theta} = 0 \quad (\text{A.52})$$

$$A_{45} = \frac{\partial \dot{\phi}}{\partial \theta} = 0 \quad (\text{A.53})$$

$$A_{55} = \frac{\partial \dot{\theta}}{\partial \theta} = 1 \quad (\text{A.54})$$

$$A_{65} = \frac{\partial \ddot{\theta}}{\partial \theta} = t_s \left(\frac{1}{I_{yy}} (m_s g h_p - K_{pitch}) \right) \quad (\text{A.55})$$

The elements of the H_k matrix containing the derivatives with respect to the pitch angle θ are defined as

$$H_{15} = \frac{\partial a_y}{\partial \theta} = 0 \quad (\text{A.56})$$

$$H_{25} = \frac{\partial \dot{\psi}}{\partial \theta} = 0 \quad (\text{A.57})$$

$$H_{35} = \frac{\partial \dot{\phi}}{\partial \theta} = 0 \quad (\text{A.58})$$

$$H_{45} = \frac{\partial \dot{\theta}}{\partial \theta} = 0 \quad (\text{A.59})$$

The elements of the A_k matrix containing the derivatives with respect to the pitch rate $\dot{\theta}$ are defined as

$$A_{16} = \frac{\partial \dot{v}_y}{\partial \dot{\theta}} = 0 \quad (\text{A.60})$$

$$A_{26} = \frac{\partial \dot{\psi}}{\partial \dot{\theta}} = 0 \quad (\text{A.61})$$

$$A_{36} = \frac{\partial \dot{\phi}}{\partial \dot{\theta}} = 0 \quad (\text{A.62})$$

$$A_{46} = \frac{\partial \dot{\phi}}{\partial \dot{\theta}} = 0 \quad (\text{A.63})$$

$$A_{56} = \frac{\partial \dot{\theta}}{\partial \dot{\theta}} = t_s \quad (\text{A.64})$$

$$A_{66} = \frac{\partial \ddot{\theta}}{\partial \dot{\theta}} = 1 + t_s \left(-\frac{1}{I_{yy}} D_{pitch} \right) \quad (\text{A.65})$$

The elements of the H_k matrix containing the derivatives with respect to the pitch rate $\dot{\theta}$ are defined as

$$H_{16} = \frac{\partial a_y}{\partial \dot{\theta}} = 0 \quad (\text{A.66})$$

$$H_{26} = \frac{\partial \psi}{\partial \dot{\theta}} = 0 \quad (\text{A.67})$$

$$H_{36} = \frac{\partial \phi}{\partial \dot{\theta}} = 0 \quad (\text{A.68})$$

$$H_{46} = \frac{\partial \dot{\theta}}{\partial \dot{\theta}} = 1 \quad (\text{A.69})$$

B

Figures Roll and Pitch Angle

In this appendix the figures are shown of the roll and pitch angle estimation that were not showed in Chapter 6. The appendix follows the same structure as that chapter, which means that first the estimation results are shown when there is no noise added to the inputs of the observers and then the results are shown when the inputs are added to the observer.

B.1. No noise Added

Since the estimation results of the fishhook manoeuvre and the Hockenheim racetrack were already shown in Section 6.1.1, they will not be shown and discussed here.

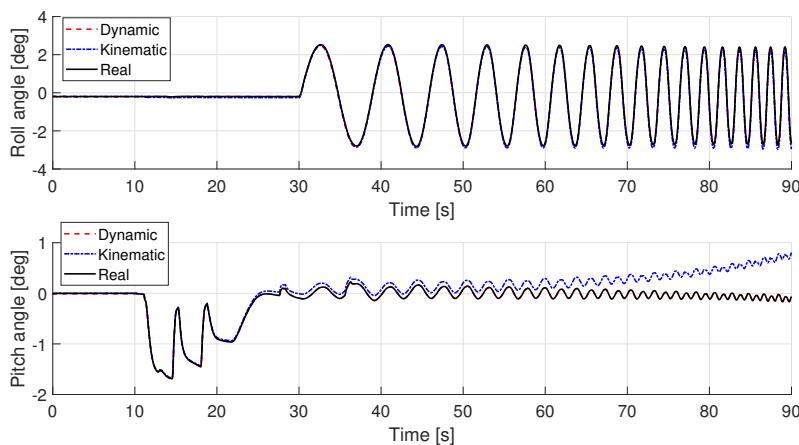


Figure B.1: Estimation performance during the sine sweep manoeuvre

Starting with the estimation results of the sine sweep manoeuvre, which can be seen in Figure B.1. It can be seen that the estimates of the roll and pitch angle of the dynamic observer follow the true values well and hardly any deviation can be observed. It becomes also clear the the estimate of the pitch angle of the kinematic observer slowly drifts away from the true value. A possible explanation for this is that the Kalman filter does not correct the drift, because the measurement covariance matrix in the first measurement update is low.

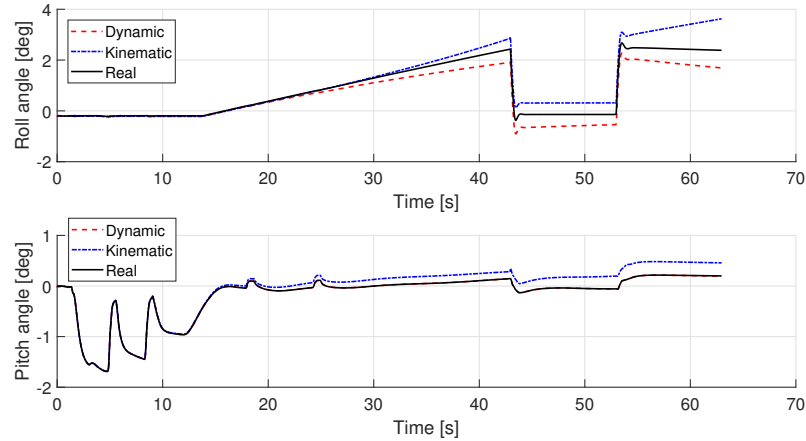


Figure B.2: Estimation performance during the step response manoeuvre

In Figure B.2 the estimation performance of the observers can be seen for the step response manoeuvre. It can be observed that a small deviation can be seen for both observers regarding the roll angle. For the dynamic observer this can be explained by the fact that for larger slip values the calculated tyre forces in the internal vehicle model are too high. The deviation of the kinematic observer can be explained by the fact that slip is not taken into account in the kinematic relations, which is a dominant effect in the step response manoeuvre. The deviation of the pitch angle of the kinematic observer can be explained by the coupling of the roll and pitch angle in the state vector.

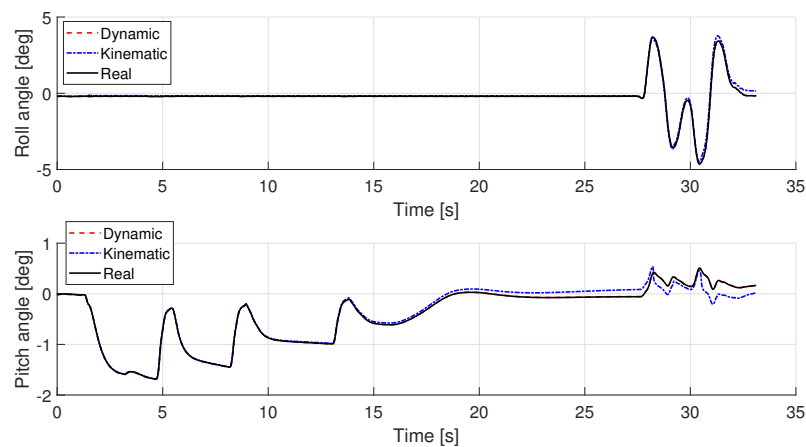


Figure B.3: Estimation performance during the double lane change manoeuvre

The results of the double lane change manoeuvre can be seen in Figure B.3. It can be observed that both observers perform well. There is some deviation of the kinematic observer regarding the pitch angle at the end of the manoeuvre, but this is so small that it can be neglected. The main reason for the good performance of both observers can be given by the relatively slow steering rate, which means that the slip values are not high. This results in an accurately calculated tyre force in the dynamic observer and the kinematic relations can still capture all the motions in the kinematic observer.

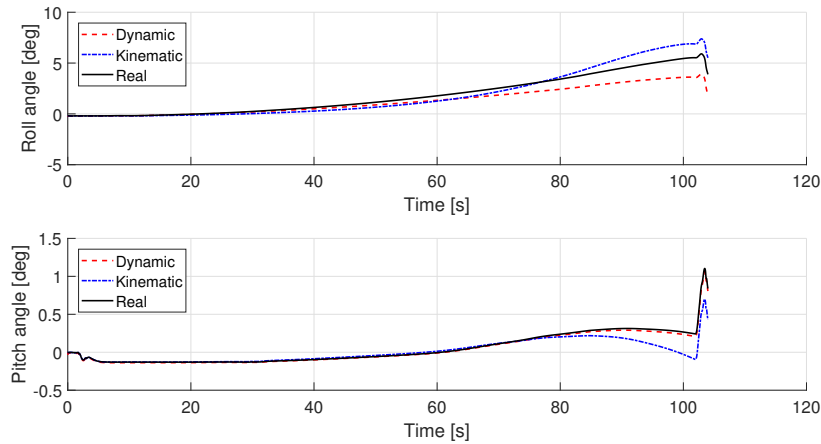


Figure B.4: Estimation performance during the skidpad manoeuvre

In Figure B.4 the estimation performance of the skidpad manoeuvre can be seen. As already explained in Chapter 6 the bad performance of the dynamic observer can be explained due to a mismatch in tyre forces, which in turn is then over compensated by the term that contain the roll stiffness and roll coefficients, which leads to a roll angle that is too low in the internal vehicle model compared to the actual roll angle. The kinematic observer only shows some deviation at the end of the manoeuvre, where the accelerations are the largest and slip plays a dominant role.

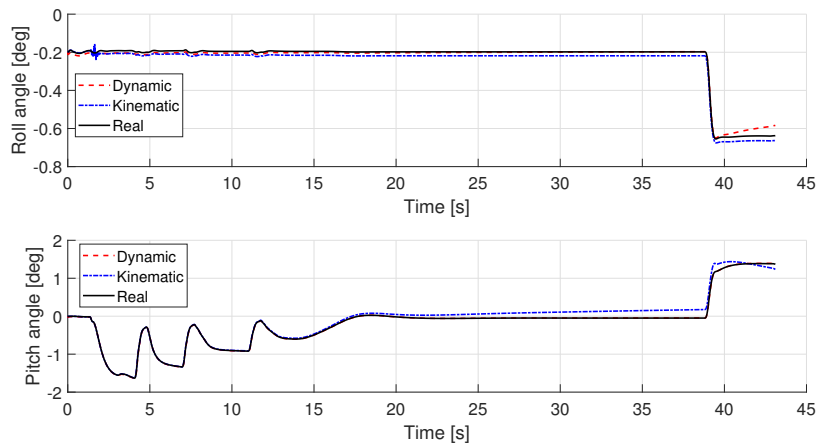


Figure B.5: Estimation performance during normal straight line braking

In Figure B.5 the estimation results can be seen for normal straight line braking. The slip values are not dominant in this manoeuvre and as expected the roll and pitch angle estimates of both observer match the true roll and pitch angle quite well. This is different for the emergency braking manoeuvre, which can be seen in Figure B.6. During this manoeuvre one of the wheels locks up and the kinematic observer does not take this into account, which explains the deviation of the roll angle.

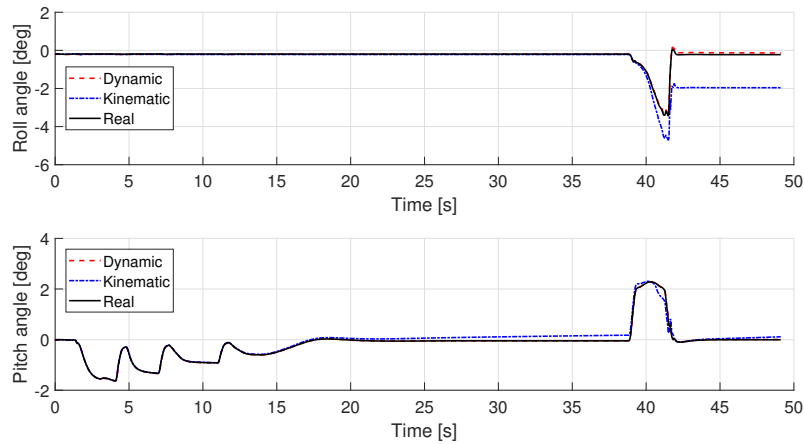


Figure B.6: Estimation performance during emergency straight line braking

B.2. Noise Added

In this section the figures of the estimation performances of the both observers can be seen when the sensor noise is added to the inputs of the observers. Just as in the previous section the figures that already have been shown in Chapter 6 are not shown. This means that the figures of the skidpad and emergency braking manoeuvre are not shown here.

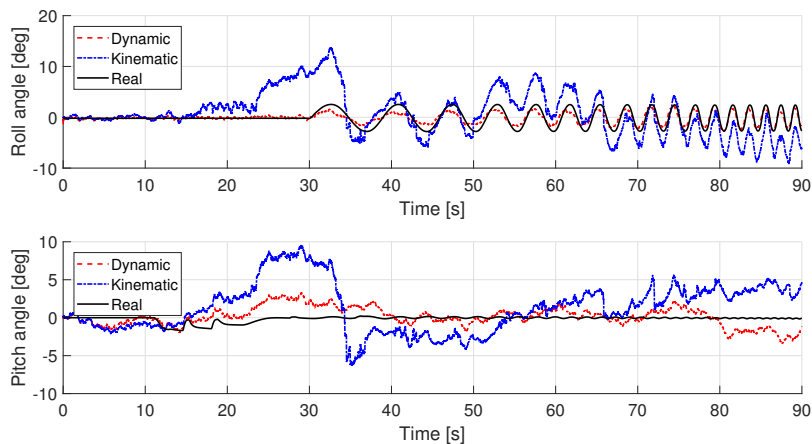


Figure B.7: Estimation performance during the sine sweep manoeuvre with noise added

In Figure B.7 the estimation performance of the sine wave manoeuvre can be seen. It can be seen that the roll estimate of the kinematic observer first drifts away, but then recovers when the steering input is started. The estimate is then in the first part quite accurate, but when the steering input rate increases the estimate drifts away, because the slip becomes a dominant roll. From the figure can also be observed that the dynamic observer performs much better in this manoeuvre, due to the internal vehicle model.

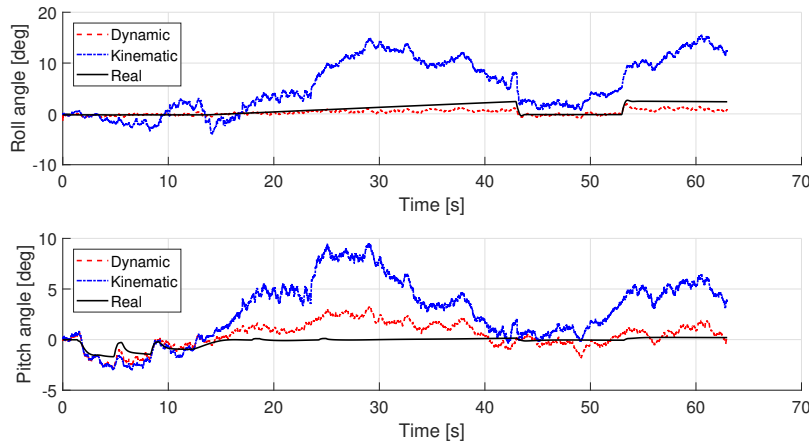


Figure B.8: Estimation performance during the step response manoeuvre with noise added

In Figure B.8 estimation performance of the step response manoeuvre can be seen. It becomes clear that the drift of the roll and pitch estimate of the kinematic observer is very large. The coupling of the states becomes also clearly visible again. The roll and pitch angle estimates of the dynamic observer stay much closer to the actual values. Even if the dynamics inside the internal vehicle model do not match completely with the real behaviour, they help the observer to estimate the roll and pitch angle much more accurately. A combination of extreme dynamics and very noisy sensor inputs causes the kinematic observer to drift away completely.

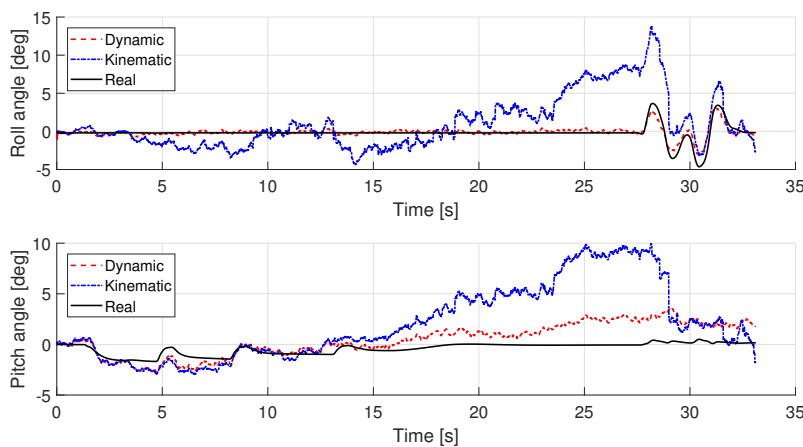


Figure B.9: Estimation performance during the double lane change manoeuvre with noise added

In Figure B.9 the estimation of the double lane change manoeuvre can be seen. It becomes visible that the roll estimate of the kinematic observer slowly drifts away from the true value when there are no accelerations in the lateral direction. As soon as the actual manoeuvre starts, the Kalman filter starts working, because it gets an lateral acceleration input and the drift of the roll estimate is corrected. Again in this figure the coupling of the roll and pitch angle estimate is clearly visible.

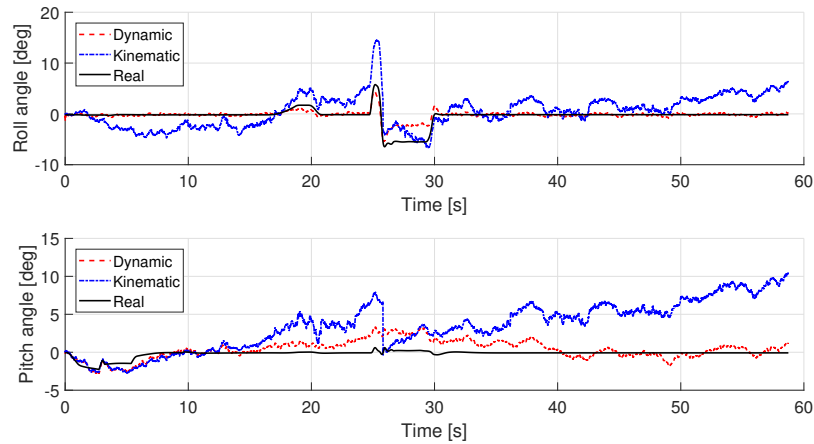


Figure B.10: Estimation performance during the fishhook manoeuvre with noise added

In Figure B.10 the estimation performance of the fishhook manoeuvre can be seen. Although the kinematic observer does not estimate the roll and pitch angle correctly, the drift is not so large as in the manoeuvres of the skidpad and double lane change manoeuvre. A possible explanation for this is that the actual steering action of the manoeuvre begins not so rapid, which leads to a better tracking of the states. The dynamic observer shows similar behaviour as in the previous manoeuvres.

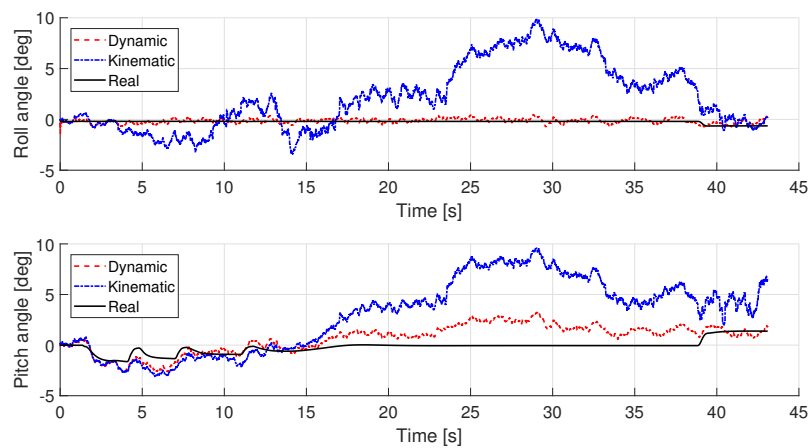


Figure B.11: Estimation performance during normal braking with noise added

In Figure B.11 the estimation performance of the observers can be seen when the normal braking manoeuvre is performed. Again the drift of the estimates of the roll and pitch angle of the kinematic observer is clearly visible. The dynamic observer performs similar as in the other manoeuvres.

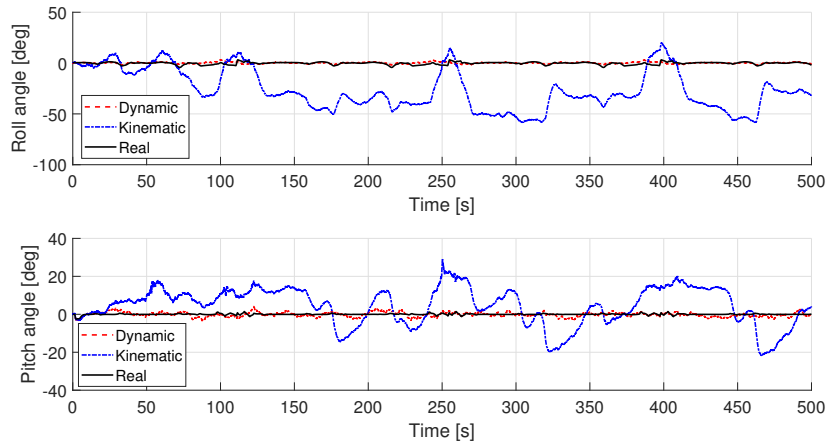


Figure B.12: Estimation performance of driving on the Hockenheim racetrack with noise added

Lastly in Figure B.9 the estimation performance of the observers can be seen when the vehicle is driven on the Hockenheim racetrack. The only thing that can be concluded from the figure is that the estimates of the roll and pitch angle of the kinematic observer completely lost track of the true roll and pitch angle. The kinematic observer already had difficulties giving correct estimates, when no sensor noise was present, but with sensor noise it completely loses track of the true roll and pitch angle. The accelerations are too high and hold on too long in order for the kinematic observer to give correct estimates.

C

Figures Lateral velocity estimation

In this appendix the estimation performances of the dynamic observer can be seen for the lateral velocity. Since the figures of the double lane change and step response manoeuvre were already shown in Chapter 6 they are not shown here.

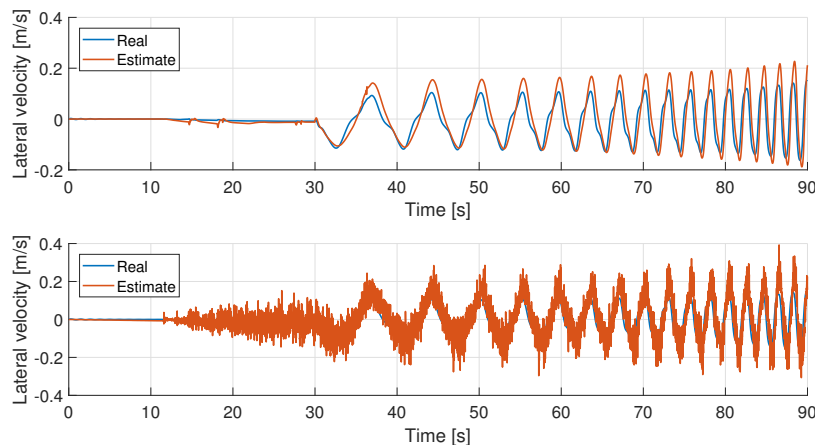


Figure C.1: Estimation performance of the lateral velocity during sine sweep manoeuvre

In Figure C.1 the estimation of the lateral velocity of the sine wave manoeuvre can be seen. It can be observed that for low steering rates the estimate is quite good and matches the true lateral velocity quite well. As the steering rate increases the estimate starts to deviate more. This can be explained as already said in the results, that for high steering inputs the slip is higher. Due to the mismatch in the tyre forces at higher slip values, the estimate of the lateral velocity starts to deviate.

In Figure C.2 the estimation performance of the lateral velocity of the skidpad manoeuvre can be seen. It can be observed that the estimate follows the true value well for the majority of the manoeuvre. Only at the end of the manoeuvre, where the lateral accelerations are the largest, there is some deviation. This can again be explained with the mismatch of the tyre forces at higher slip values.

In Figure C.3 the estimation performance of the lateral velocity of the fishhook manoeuvre can be seen. The manoeuvre consists of a very rapid steering rates to make the vehicle to roll over. This manoeuvre means high slip values and due to the vary rapid steering input the estimate is off.

In Figure C.4 the estimation performance of the lateral velocity of the Hockenheim racetrack. The drive consists of constant of hard cornering and hard braking, due to the high slip values the estimate is off most of the time.

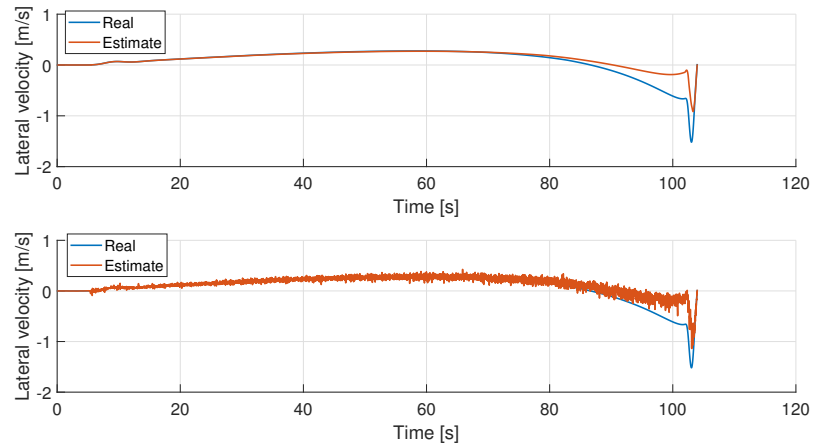


Figure C.2: Estimation performance of the lateral velocity during the skidpad manoeuvre

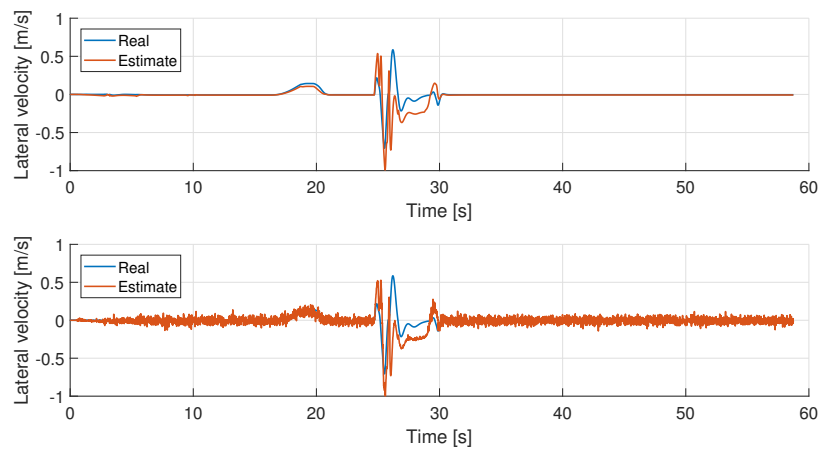


Figure C.3: Estimation performance of the lateral velocity during the fishhook manoeuvre

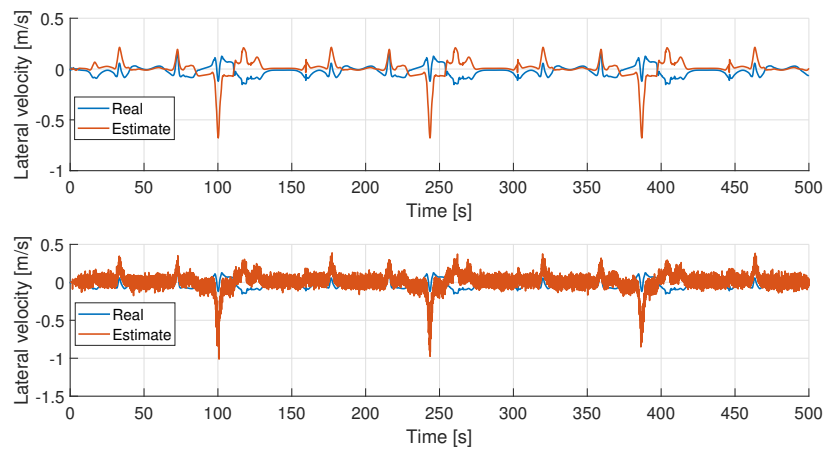


Figure C.4: Estimation performance of the lateral velocity during driving on Hockenheim racetrack

